POLITECNICO DI TORINO

Master's Degree in Biomedical Engineering

A.A. 2024/2025

Master's Thesis

Fabrication and characterization of magnetic scaffold for bone tissue engineering

Supervisor:
Prof. Enrica Verné

Candidate:
Sara Giacobbi

Co-Supervisors:
Prof. Marta Miola
Prof. Jonathan Massera
PhD Virginia Alessandra Gobbo

March 2025

Alla mia famiglia.

Mamma, papà, Martina: vi amo profondamente,

grazie per avermi reso la persona che sono.

ACKNOWLEDGEMENTS

This work is the result of a collaboration between Politecnico di Torino and Tampere University. I would like to express my gratitude to all the people who have guided me throughout this enriching journey.

A big thank you to Professors Enrica Verné and Marta Miola from Politecnico di Torino for their interest in this project and their support and help while supervising my work.

I am deeply grateful to Professor Jonathan Massera from Tampere University for his guidance, passionate collaboration and for welcoming me into his research group over these past months, offering me the opportunity to grow not only academically but also personally.

A special thanks to postdoctoral researcher Virginia Alessandra Gobbo for her teaching and supervising during the entire laboratory work. I am truly grateful for every day she spent answering my questions with patience and providing constant support, offering me an amazing example from which I could draw inspiration.

A big thank you to all the members of the Biomaterials group in Hervanta Campus (Tampere). In particular, I would like to thank Janne Koivisto for his fundamental support during the rheological tests, and Sonya, Sarah and Nicole for the time spent together in the university, you are such amazing and intelligent women!

My gratitude goes to my colleagues in Politecnico, with whom I have grown, sharing victories and defeats throughout my university career, and to all my friends, especially those I met in Tampere. 'Hohohoes', you are amazing and special people that will always have a place in my heart.

My biggest thank you is for my family: Mamma and Papà you are my pillar. Thank you for your endless support, for sharing my joy in happy moments, and for being a source of comfort in the hardest ones.

An immense thank you to my sister, Martina: my love for you is unlimited. Every day I feel incredibly grateful to have you not only as my sister but also as my best friend.

Finally, I would like to thank Felipe, whose beautiful soul enriches my life every day. Thank you for always encouraging me to believe in myself. I feel so fortunate to have met you.

ABSTRACT

The burden of cancer affects millions of people worldwide every year.
Bone cancer, in particular, is characterized by aggressive growth and great suffering for the patients. Conventional therapies, such as surgery, chemotherapy, or radiotherapy, may cause significant side effects and part of cancerous tissue might not be completely removed, causing recurrence. Moreover, surgical removal of bone cancer can leave critical bone defects, requiring the use of a bone graft. Recently, hyperthermia has emerged as a possible alternative. This therapy takes advantage of the higher sensitivity to heat of cancer cells to destroy them by locally increasing the temperature in the range 41-45 °C, causing molecular and cellular alterations which end up in cell death. In particular, magnetic hyperthermia is considered a promising option, since it can reach bone structures in depth, it is non-invasive and more tissue specific. An alternating magnetic field heats up magnetic nanoparticles, converting electromagnetic waves into thermal energy. Superparamagnetic Iron Oxide Nanoparticles (SPIONS) are considered good candidates, since they do not have a residual magnetization and possess low toxicity profile.
Bone tissue engineering is a growing field that aims at the development of bone substitutes, such as scaffolds, to repair damaged tissue. Bioactive glasses are good material candidates for their ability to create a strong bond with bone through the deposition of a hydroxyapatite layer on their surface. 1393B20 BAG overcomes the high crystallization tendency of traditional silicate glasses while promoting angiogenesis and osteogenesis in vitro and enhancing mineralization and collagen formation in vivo.
This thesis' work focused on the processing of multifunctional 3D printed scaffolds made of bioactive glass 1393B20 and SPIONS, with the aim of repairing critical bone defects of patients who underwent surgical removal of bone cancer and remove, at the same time, the residual cancer cells from the site.
SPIONS were synthesized with the co-precipitation method and analyzed both as dry powder and liquid solution with TEM, which confirmed the success of their synthesis. 1393B20 BAG powder was combined with SPIONS and a binding agent in different ratio to produce an ink for robocasting. The rheological studies proved the suitability for printing for all the different inks, showing shear thinning behavior. The obtained 3D printed scaffolds were sintered and the impact of the SPIONS on the mechanical properties and bioactivity was assessed through compression test, in vitro dissolution in SBF, SEM and EDS analysis. A calorimetric test was performed to verify the heating capacity of the scaffolds when exposed to a magnetic field. Live and Dead and CyQUANT assays analyzed the cytotoxicity of the material.
From the obtained results, scaffolds proved to maintain their magnetic properties and increase their temperature under magnetic field exposure. Moreover, they showed promising results about their dissolution in SBF and bioactivity, with the deposition of a CaP HA-like layer. Nevertheless, further improvements are needed to enhance their mechanical properties, since they were not able to reach the ones of trabecular bone. Cell viability was assessed around the samples, but mild cytotoxicity was found in direct contact with the scaffolds, as confirmed by the poor cell proliferation quantification. Additional investigation is required to find new methods to improve biocompatibility for future clinical applications.

TABLE OF CONTENTS

1. BONE TISSUE

1.1 Human skeleton

Bones and cartilages form the human skeleton, an essential framework that, in combination with muscles and bands of fibrous connective tissue, allows the movement of the body (musculoskeletal system) [1], [2], [3]. The human skeleton is made of 206 bones, which are classified depending on their shape into: long (e. g. femur), short (e. g. carpals), flat (e. g. skull), irregular (e. g. vertebrae) and sesamoid (e. g. patella) bones [1], [2]. Besides locomotion, the human skeleton accomplishes many other functions, such as: protection of internal soft tissues and vital organs, stabilization and support of the body, storage of mineral salts like calcium and phosphate, production of blood cells (erythrocytes, leukocytes, platelets), also called *hematopoiesis*, in the bone marrow [2], [4], [5].

1.2 Bone structure

Two main types of bone tissues can be found in each bone: compact bone and cancellous (spongy) bone. The first one (Figure 1) covers the surface of the bone and appears solid and dense. It is characterized by cylindrical structures called haversian systems (or osteons). Osteons are formed by layers of collagen and calcified bone matrix (lamellae) arranged around a central canal (Haversian channel), through which nerves, lymphatic vessels and arterioles pass providing nutrient supply. In long bones, the haversian systems are aligned in the same direction of the long axis and the medullar cavity containing yellow bone marrow is surrounded by this type of bone tissue [1], [2], [6], [7].

The second type of bone tissue (Figure 2), called cancellous bone, is located in the inner part of the bone and it is defined by the presence of trabeculae: lamellae shaped as thin plates or rods forming a latticework. Red bone marrow is placed inside this trabecular structure [1], [2], [6], [7]. Since the surface to volume ratio is higher and there is more exposure to bone marrow and blood flow, spongy bone has a higher turnover than cortical bone [8], so it can easily undergo remodeling according to changes in the body [7].

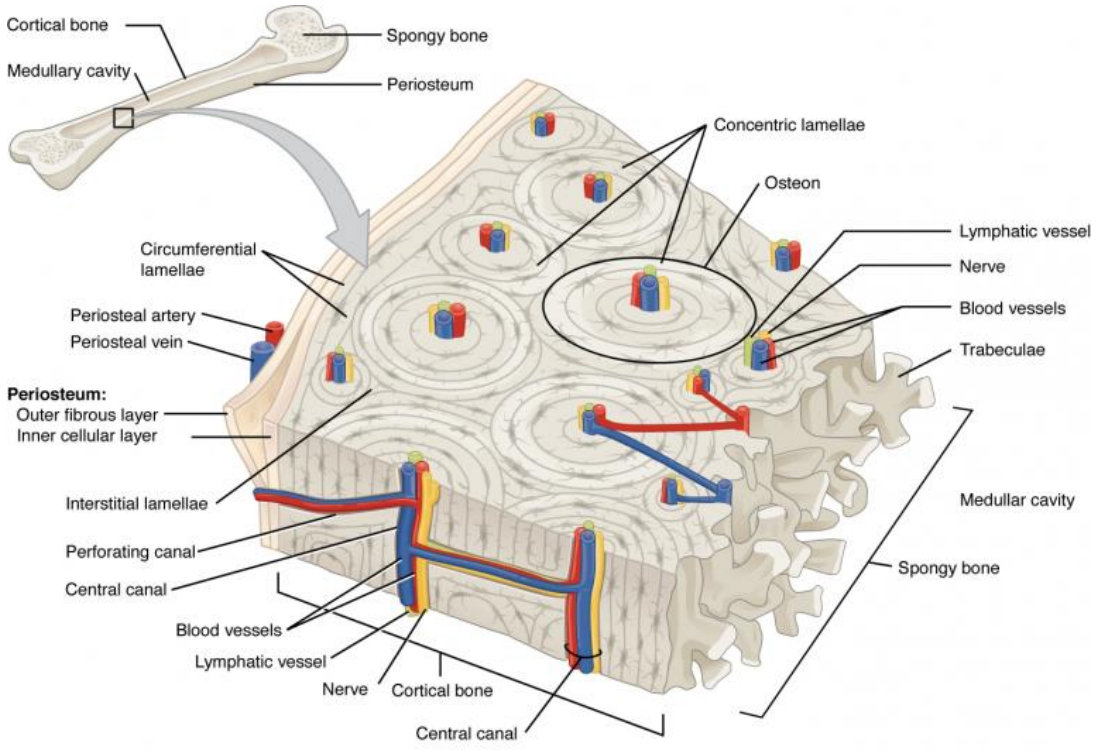

Figure 1. Compact bone. A cross section of compact bone shows its structure. Many osteons with various vessels and nerves passing through them are represented [7].

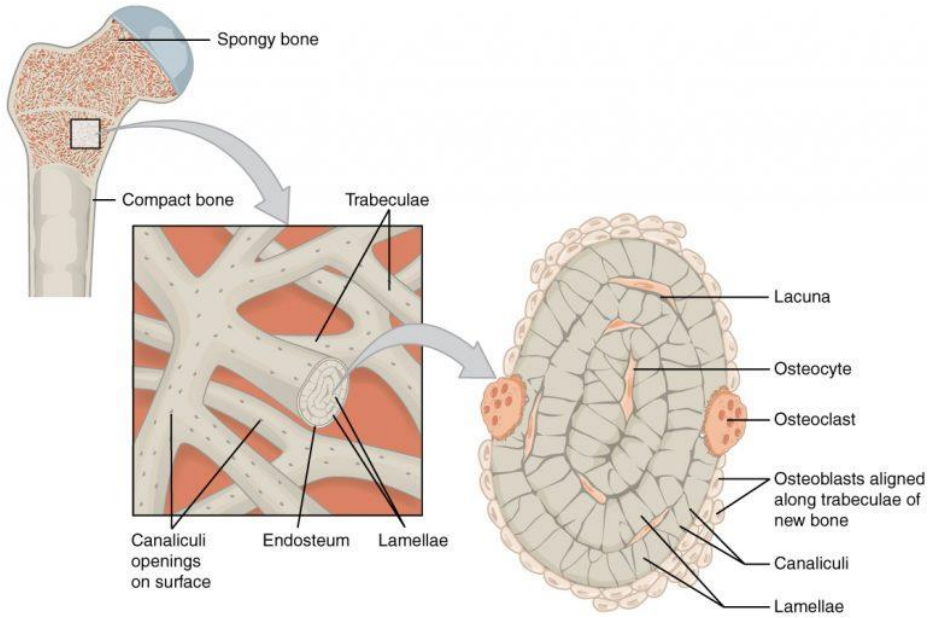

Figure 2. Cancellous bone. A complex structure of trabeculae forms spongy bone. Red bone marrow fills the space in between [7].

In long bones, such as the femur shown in Figure 3, compact bone tissue is highly present in the diaphysis (central region), while the epiphyses (extremities) present a cancellous internal structure [1], [9].

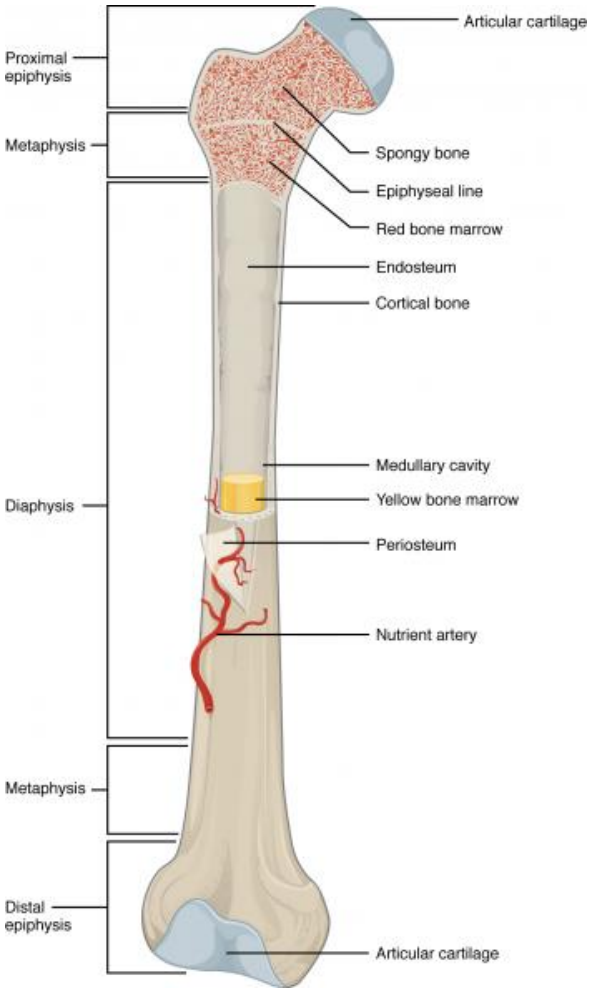

Figure 3. Long bone structure. Long bones are characterized by a central portion called diaphysis and two portions at the extremities called epiphyses [7].

The combination of compact and spongy tissues plays an important role in the distribution of loads within the bone: compact bone is able to resist higher modulus values of forces, but it has a little deformation before breaking [10]. Spongy bone, on the other hand, makes the bone lighter and has a high capacity for storing energy [7], [11]. Thanks to trabecular bone, loads are moved from the articular surface to the cortical bone [8]. In this way, the combination of the two tissues offers a total resistance higher than the one of the single tissues separately [10].

1.3 Periosteum and endosteum

A double layered coating tissue called periosteum envelops the external part of the bones (except for the epiphyses of long bones which are covered by articular cartilage). It is formed by an outer fibrous layer surrounding an area with bone cells that contribute to growth, repair and remodeling of bone tissue. Lymphatic vessels, nerves and blood vessels pass through the periosteum, supplying compact bone with nutrients and making the bone highly sensitive to pain. Indeed, a disruption of the periosteum produced by fractures or tumors can cause severe pain [1], [2], [7].

Around the medullar cavity and the trabeculae, there is another layer of bone cells called endosteum. Here, the cells have the same function of growth, repair and remodeling as the ones in the periosteum [2], [7].

1.4 Bone matrix

Bone is a connective tissue containing a hard, calcified matrix which makes it rigid [1], [2], [7]. Bone matrix is composed of an organic and an inorganic part. The organic part represents 35-40% of the bone's dry weight and it is mainly made of collagen type I (90%) [5], which not only provides tensile strength and flexibility to the bone, but also acts like a surface available for the deposition of mineral crystals during bone mineralization [12]. The organic part includes growth factors, proteoglycans, glycosaminoglycans, osteocalcin, osteopontin and bone sialoprotein [5], [12]. The inorganic part represents 60-65% of the bone's dry weight [12]. It includes calcium (Ca^{2+}) and phosphate (PO_4^{3-}) ions, which can combine to form hydroxyapatite crystals ($Ca_{10}(PO_4)_6(OH)_2$) [5] providing strength and hardness [7], and some other mineral ions such as magnesium (Mg^{2+}), sodium (Na^+) and potassium (K^+) [12].

Figure 4 shows the hierarchical organization of bone, illustrating the presence of both organic and inorganic parts.

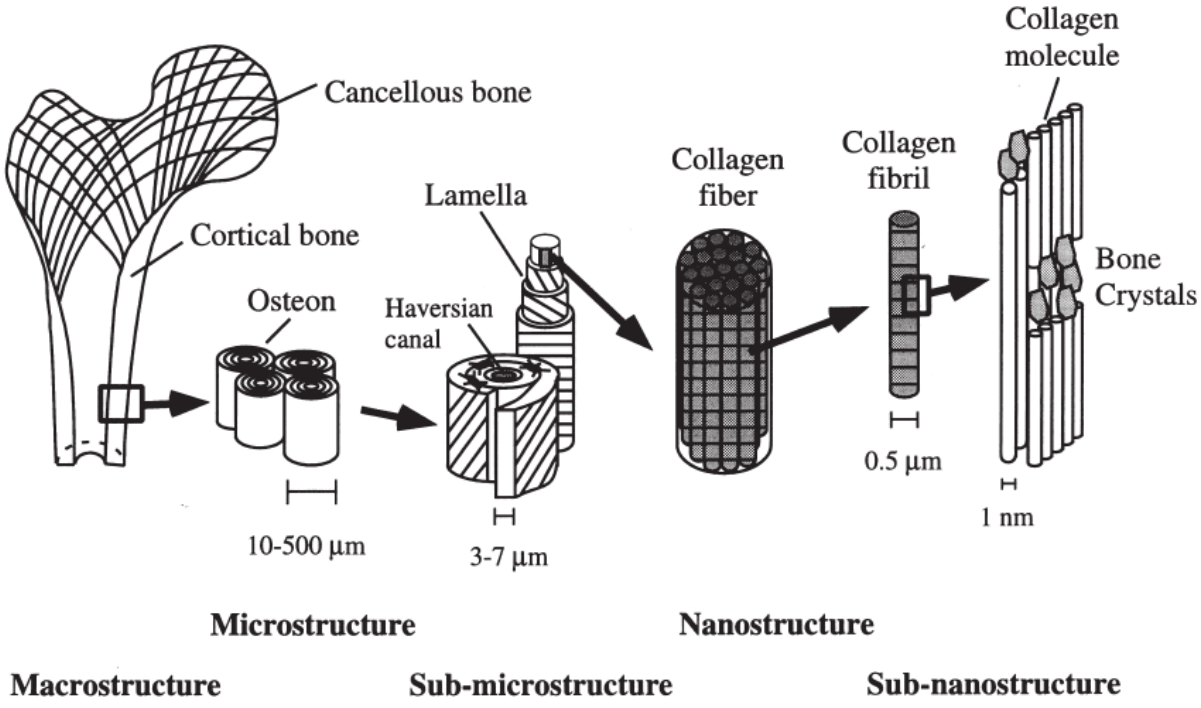

Figure 4. Hierarchical organization of the bone. Summary scheme that represents bone from the macro (on the left) to the sub-nano structure (on the right) [13].

1.5 Bone cells

The high dynamicity of bone tissue is due to the activity of its cells: osteoblasts, osteoclasts and osteocytes [5]. In the next paragraphs, each type of bone cell and its function are reported and visually represented in Figure 5.

1.5.1 Osteoblasts

Osteoblasts are cuboidal bone cells found in the endosteum, in the cellular layer of the periosteum and in areas where bone is growing. They derive from the differentiation of osteogenic cells [7] and act as new bone former [5], [7]. Osteoblasts synthesize bone matrix with a first organic matrix

deposition and a following mineralization. When they are mature, osteoblasts can undergo apoptosis or evolve into osteocytes or bone lining cells [5].

1.5.2 Bone lining cells

Bone lining cells are flat shaped osteoblasts located on bone surfaces in situations of quiescence, in which the bone is not being resorbed, nor new bone is forming. Further studies are needed to fully understand their functions, but some researchers found that these cells can prevent osteoclast activity when bone resorption is not required [5].

1.5.3 Osteocytes

Osteocytes are mature bone cells derived from osteoblast differentiation and representing 90-95% of the total number of bone cells [5]. They are embedded in the bone matrix inside cavities between the lamellae called lacunae [2]. Osteocytes present a dendritic shape, with dendrites expanding into the canaliculi: tiny tunnels connecting the various lacunae that allow the transport of nutrients to the osteocytes and the removal of waste [5], [7]. Through the osteocyte lacuno-canalicular system (OLCS) [14], osteocytes can also communicate between each other and perform their cytoplasmatic processes [5], [7]. Thanks to this complex structure, these cells can act as mechanosensors recognizing mutations in mechanical pressure and loads, and so guiding the adaptation of the bone to these changes and thus regulating the activity of osteoblasts and osteoclasts [5]. Moreover, they can maintain the mineral concentration level in the bone matrix through the production of some proteins, such as dentine matrix protein 1 (DMP1) [5], [7].

1.5.4 Osteoclasts

The high dynamicity of bone tissue is not only due to the constant bone production by osteoblasts, but also to the resorption activity performed by osteoclasts. Osteoclasts are multinucleated cells originating from monocytes and macrophages that can be found in the endosteum, periosteum and in situations where bone is old, injured or there is a bone excess [7]. Some diseases, such as osteoporosis or osteopetrosis, are caused by an abnormal behavior of osteoclasts. In osteoporosis the activity of osteoclasts is increased and bone density results low, with increased possibility of bone fractures. In osteopetrosis osteoclasts activity is highly reduced, leading to an aggregation of bone mass. Osteoclast activity can become abnormal also in case of bone metastasis, causing periarticular erosions [5].

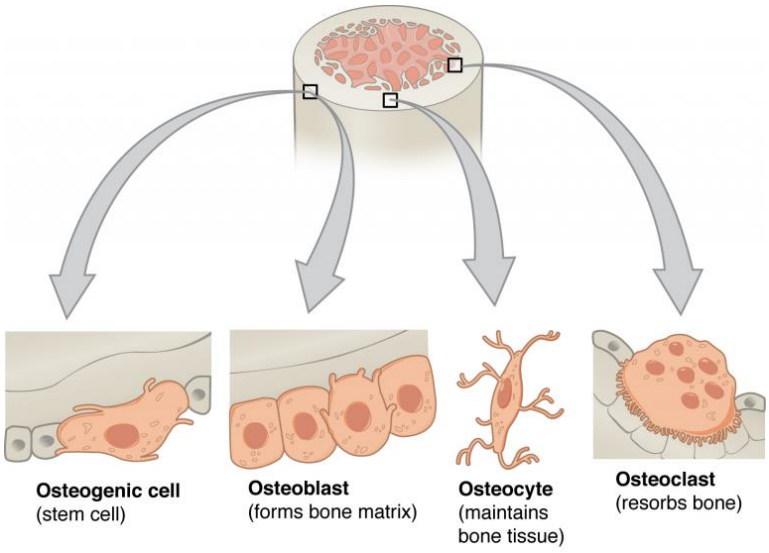

Figure 5. Bone cells. From the left: osteogenic cells, osteoblasts, osteocytes and osteoclasts [7].

1.6 Bone remodeling

The continuous removal of old bone and deposition of new one is a lifetime process called bone remodeling. Bone remodeling occurs to prevent the accumulation of microdamage and maintain the structural integrity of bone tissue. Moreover, it helps bone adaptation to variations in the mechanical loading: bone remodeling reacts by removing bone where not needed and by adding it where loads require it. Every year approximately 5-10% of total bone is renewed, with a higher metabolic rate in trabecular bone (10 times higher than the cortical one) [15].

The activities of osteoclasts and osteoblasts play an essential role in the balance between bone resorption and bone deposition, respectively. In particular, some key signaling molecules, such as the cell surface receptor RANK in pre-osteoclasts and the RANK ligand expressed by osteoblasts, regulate the communication between these two types of bone cells [15].

As represented in Figure 6, bone remodeling can be divided into 6 phases:

1. **Quiescent phase.** During this phase, the bone is at rest and nothing is happening.
2. **Activation phase**. Before resorption starts, bone lining cells retract and osteoclast precursors are recruited from blood circulation. The precursors develop into mature osteoclasts and attach to the mineralized bone surface.
3. **Resorption phase**. Osteoclasts release hydrogen ions (pH becomes lower) and enzymes, such as cathepsin K, to degrade bone matrix. The process lasts about 2-4 weeks.
4. **Reversal phase**. During this phase, the transition between bone resorption and bone formation occurs. Some coupling signals such as bone matrix-derived factors and fibroblast growth factors are responsible for this change.
5. **Formation phase**. Osteoclasts detach from bone surface and differentiated osteoblasts start to deposit osteoid matrix in the gaps created by the previous resorption. When their activity stops, osteoblasts become bone lining cells and cover the surface of the newly created bone.
6. **Mineralization phase**. This process starts 30 days after new bone deposition and ends at day 90 for the trabecular bone and at day 130 for the cortical one [15].

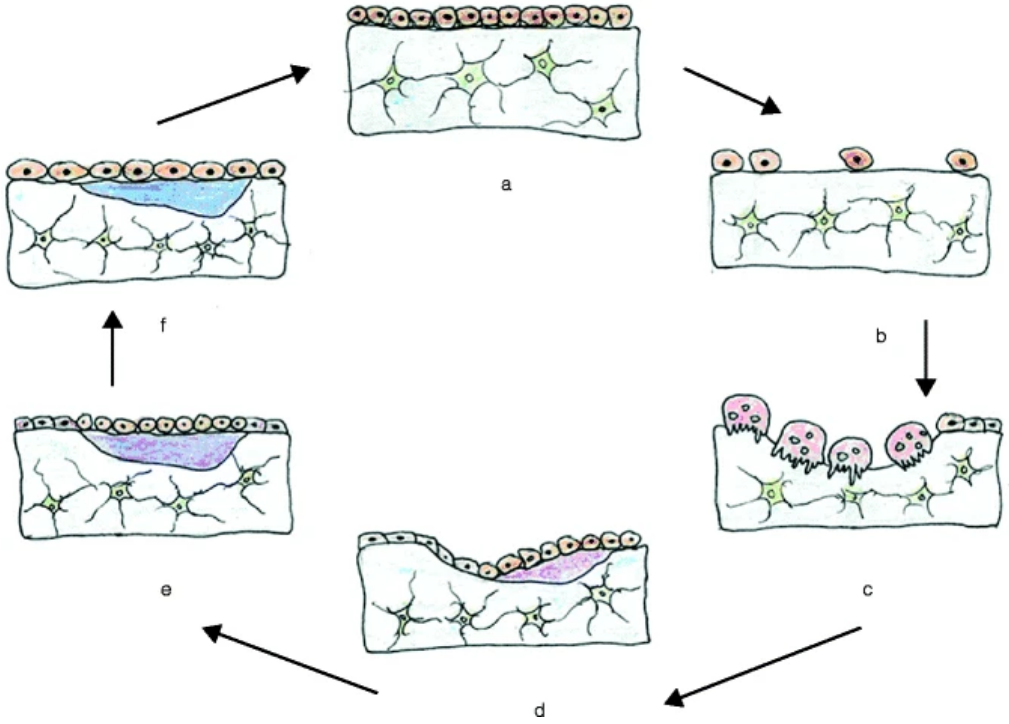

Figure 6. Remodeling phases. (a) Quiescent phase. (b) Activation phase. (c) Resorption phase. (d) Reversal phase. (e) Formation phase. (f) Mineralization phase [15].

1.7 Bone repair

When a fracture occurs, bone starts a process called bone fracture healing, during which it aims at restoring the damaged tissue to its original state [16]. Therefore, if the type of defect is small enough and doesn't require the application of a bone graft, bone has the ability to self-heal, forming new functional bone tissue [17]. Depending on the type of fracture and the distance between the fragments, two possible kinds of bone healing can take place: primary (direct) or secondary (indirect) bone healing [16], [18].

With primary bone healing, the fracture is characterized by high stability because of an internal fixation under compression, and the strain deriving from mechanical stimulation is low (below 2%) [16], [19]. First, at the end of the osteons closest to the fracture site, osteoclasts form cutting cones, creating longitudinal cavities that will be filled with bone matrix produced by osteoblasts. In this way,

Haversian systems can be restored and remodeled into a lamellar shape. Consequently, the ends of the fracture are joined and no callus formation takes place (Figure *7*) [19].

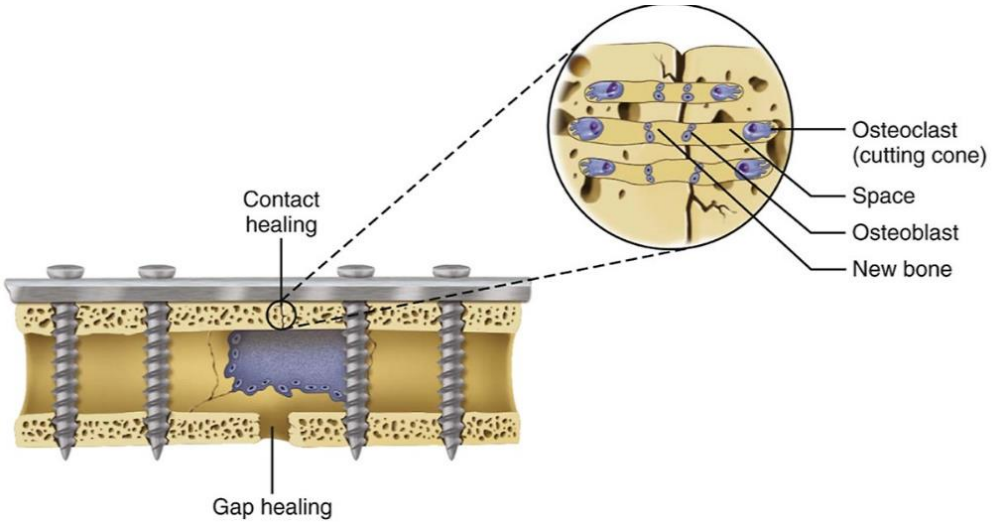

Figure 7. Primary bone healing. Osteoclasts create a cutting cone forming cavities along the fracture site. Osteoblasts fill the cavities with new bone matrix which is then remodeled into a lamellar shape [20].

Secondary bone healing is more common and occurs in case of non-rigid fixation methods, such as external fixation, with a mechanical strain between 2% and 10% [16]. It can be divided into 4 stages (Figure *8*):

1. **Inflammation**: immediately after the fracture, broken blood vessels from periosteum, osteons and medullar cavity form a hematoma, which will act as a template for the subsequent callus formation [18], [19]. Bone cells in the fracture site die because of the lack of nutrients [21] and macrophages, monocytes and lymphocytes are attracted by the presence of acute inflammatory markers. These white cells start removing the necrotic tissue and secrete cytokines beneficial for angiogenesis and healing, such as the vascular endothelial growth factor (VEGF). This first stage lasts approximately 5 days [19].
2. **Fibrocartilaginous callus formation**: during the second stage, mesenchymal stem cells are recruited and differentiate into fibroblasts, osteoblasts and chondroblasts. A collagen-rich fibro-cartilaginous network (soft callus) is created via chondrogenesis around the fracture, and, at the same time, a layer of trabecular bone is deposited next to the periosteum. Similarly to the first stage, this process lasts 5 days [16], [19].
3. **Bony callus formation**: until the fourth week after the fracture and overlapping the second stage, the third stage takes place. The soft callus is converted into a hard callus via endochondral ossification: cartilage ossifies, chondrocytes die because of a lack of nutrients and spongy bone replaces them, forming a calcified area that connects fracture ends [16], [19], [21] .
4. **Bone remodeling**: the final stage consists of bone remodeling according to the strain the healing bone is undergoing to. It is performed by osteoclasts and osteoblasts and leads to the formation of the medullar cavity in the inner part and lamellar bone in the outer part. This step can last months, or even years, until the bone is completely healed [18], [19], [21].

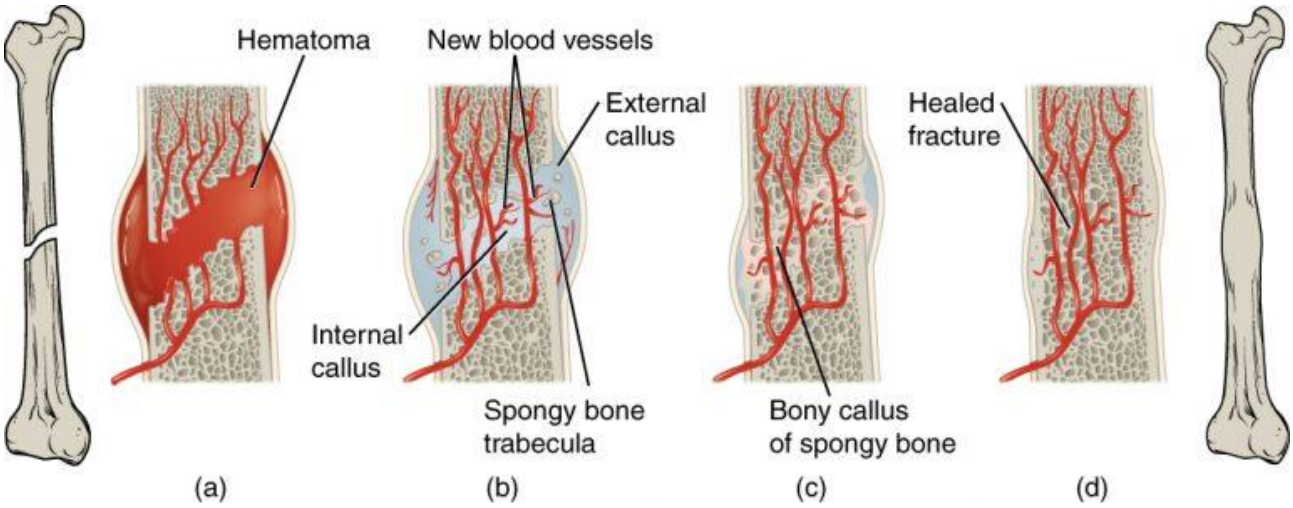

Figure 8. Stages of secondary bone healing. (a) Hematoma formation. (b) Soft callus formation with deposition of a layer of spongy bone. (c) Conversion of the soft callus into a hard one via endochondral ossification. (d) Remodeling of bony callus by osteoblasts and osteoclasts and formation of a mature, healed bone [18].

However, 5-10% of all fractures do not heal properly, or heal with a certain delay, because of excessive load and movement or because of infection, tumors, comminuted fractures and interrupted nutrient supply by blood vessels [16], [19].

REFERENCES

[1] J. A. Gosling MD, MB ChB, FRCS, FAS, P. F. Harris MD, MB ChB, MSc, FAS, J. R. Humpherson MB ChB, I. Whitmore MD, MB BS, LRCP MRCS, FAS, and P. L. T. Willan MB ChB, FRCS, "Basic Anatomical Concepts," in *Human Anatomy, Color Atlas and Textbook*, vol. Chapter 1, J. A. Gosling MD, MB ChB, FRCS, FAS, P. F. Harris MD, MB ChB, MSc, FAS, J. R. Humpherson MB ChB, I. Whitmore MD, MB BS, LRCP MRCS, FAS, and P. L. T. Willan MB ChB, FRCS, Eds., 2017, pp. 1–23. doi: 10.1016/B978-0-7234-3827-4.00001-1.

[2] Springhouse, "Musculoskeletal system," in *Lippincott professional guides : Anatomy & physiology*, 2nd ed., in Lippincott's Healthcare Professional Guide. , Wolters Kluwer Health, 2002, p. 255. Accessed: Sep. 27, 2024. [Online]. Available: https://ebookcentral.proquest.com/lib/tampere/detail.action?docID=2032679

[3] A. Warren, "human skeleton," *Encyclopedia Britannica*, Sep. 2024, Accessed: Sep. 27, 2024. [Online]. Available: https://www.britannica.com/science/human-skeleton

[4] Britannica The Editors of Encyclopaedia, "bone marrow," *Encyclopedia Britannica*, Jul. 2024, Accessed: Sep. 27, 2024. [Online]. Available: https://www.britannica.com/science/bone-marrow

[5] R. Florencio-Silva, G. R. D. S. Sasso, E. Sasso-Cerri, M. J. Simões, and P. S. Cerri, "Biology of Bone Tissue: Structure, Function, and Factors That Influence Bone Cells," *BioMed Research International*, vol. 2015, pp. 1–17, 2015, doi: 10.1155/2015/421746.

[6] Lumen Learning, "Module 23: The Musculoskeletal System, Structure of bone," Biology for Majors II. Accessed: Sep. 25, 2024. [Online]. Available: https://courses.lumenlearning.com/wm-biology2/chapter/structure-of-bones/#:~:text=Compact%20bone%20tissue%20is%20composed,%2C%20osteoprogenitor%20cells%2C%20and%20osteoblasts

[7] Lindsay M. Biga, Staci Bronson, Sierra Dawson, Amy Harwell, Robin Hopkins, Joel Kaufmann, Mike LeMaster, Philip Matern, Katie Morrison-Graham, Kristen Oja, Devon Quick, Jon Runyeon, OSU OERU, and OpenStax, "Bone Structure," in *Anatomy and Physiology*, in Chapter 6.3. , 2019.

[8] S. M. Ott, "Cortical or Trabecular Bone: What's the Difference?," *Am J Nephrol*, vol. 47, no. 6, pp. 373–375, 2018, doi: 10.1159/000489672.

[9] Heaney, Robert Proulx and Whedon, G. Donald, "bone," *Encyclopedia Britannica*, Sep. 2024, Accessed: Sep. 27, 2024. [Online]. Available: https://www.britannica.com/science/bone-anatomy/Bone-morphology#ref470921

[10] C. Bignardi, "Lezioni biomeccanica dell'osso, Politecnico di Torino." Oct. 03, 2021.

[11] F. Gaynor Evans. Ph.D., "The Mechanical properties of the Bone," in *Artificial Limbs: a review of current developments*, vol. 13, 1 vols., 1969, pp. 37–48. Accessed: Sep. 30, 2024. [Online]. Available: https://www.oandplibrary.org/al/1969_01_037.asp

[12] Biology Online Editors, "Bone matrix," Biology online. Accessed: Sep. 30, 2024. [Online]. Available: https://www.biologyonline.com/dictionary/bone-matrix

[13] Jae-Young Rho, Liisa Kuhn-Spearing, Peter Zioupos, “Mechanical properties and the hierarchical structure of bone,” *Medical Engineering & Physics*, pp. 92–102, 1998.

[14] C. B. Bozal, L. M. Sánchez, and A. M. Ubios, “The lacuno-canalicular system (LCS) and osteocyte network of alveolar bone by confocal laser scanning microscopy (CLSM),” *Acta Odontol Latinoam*, vol. 25, no. 1, pp. 123–131, 2012.

[15] U. Kini and B. N. Nandeesh, “Physiology of Bone Formation, Remodeling, and Metabolism,” in *Radionuclide and Hybrid Bone Imaging*, I. Fogelman, G. Gnanasegaran, and H. Van Der Wall, Eds., Berlin, Heidelberg: Springer Berlin Heidelberg, 2012, pp. 29–57. doi: 10.1007/978-3-642-02400-9_2.

[16] Sheen JR, Mabrouk A, Garla VV, “Fracture Healing Overview,” StatPearls [Internet], 2023. Accessed: Oct. 10, 2024. [Online]. Available: https://www.ncbi.nlm.nih.gov/books/NBK551678/

[17] Jonathan Massera and Amel Houaoui, “Bone tissue and cartilage,” presented at the Lecture Tampere University, Bioceramics course, Tampere University, Nov. 04, 2023.

[18] Lindsay M. Biga, Staci Bronson, Sierra Dawson, Amy Harwell, Robin Hopkins, Joel Kaufmann, Mike LeMaster, Philip Matern, Katie Morrison-Graham, Kristen Oja, Devon Quick, Jon Runyeon, OSU OERU, and OpenStax, “Bone repair,” in *Anatomy and Physiology*, in Chapter 6.5. , 2019.

[19] H. ElHawary, A. Baradaran, J. Abi-Rafeh, J. Vorstenbosch, L. Xu, and J. I. Efanov, “Bone Healing and Inflammation: Principles of Fracture and Repair,” *Semin Plast Surg*, vol. 35, no. 03, pp. 198–203, Aug. 2021, doi: 10.1055/s-0041-1732334.

[20] K. C. Lee, R. Reynolds, M. J. Recker, and M. R. Markiewicz, “Rigid Fixation of the Pediatric Facial Skeleton,” *Oral and Maxillofacial Surgery Clinics*, vol. 35, no. 4, pp. 529–541, Nov. 2023, doi: 10.1016/j.coms.2023.04.003.

[21] Lumen Learning, “Module 23: The Musculoskeletal System, Bone growth and development,” Biology for Majors II. Accessed: Oct. 10, 2024. [Online]. Available: https://courses.lumenlearning.com/wm-biology2/chapter/bone-growth-and-development/

2. TUMORS AND BONE CANCER

2.1 Preface

According to the World Health Organization (WHO) and the International Agency for Research on Cancer (IARC), 20 million new cancer cases and 9.7 million deaths were reported in the world in 2022. During their lifetime, about 1/5 of the people face the burden of cancer. This problem is expected to increase in the future, with a prediction of over 35 million new cancer cases in 2050. The increased exposure to risk factors, such as alcohol, obesity and air pollution, together with the ageing of the population, is strictly connected to the future growth and spread of cancer [1].

2.2 Tumors

When cells start proliferating without any control in an abnormal, excessive way, they can form a mass of tissue called tumor, or neoplasia [2], [3]. Tumors can originate from the clonal proliferation of a single progeny of a cell because of genetic damage or mutation. All tumors are characterized by two basic components: parenchyma and supportive stroma. Parenchyma consists of tumor cells, which are proliferating more rapidly than normal cells, ignoring the signals responsible for the interruption of the amplification. Supportive stroma includes all the blood vessels and fibrous connective tissue that have the function of supporting the growth of tumor cells [2]. Indeed, when a tumor starts growing, tumor cells produce angiogenic factors to promote the formation of new blood vessels (angiogenesis) which can provide nutrients to them [2]. Figure 9 shows the stages of tumor formation starting from a normal cell and leading to the formation of a tumor mass.

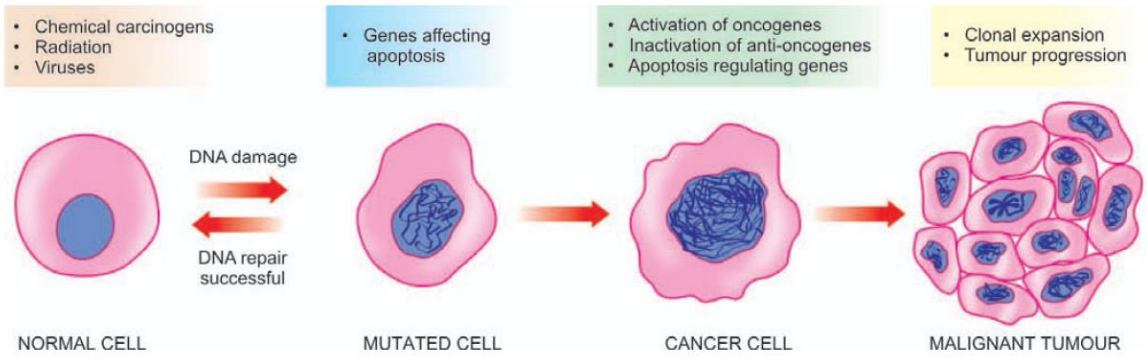

Figure 9. Tumor formation. After damage in the DNA, a normal cell can become a tumor cell and start proliferating without control [2].

Tumors can be divided into benign and malignant. A benign tumor grows slowly and is localized in a certain part of the body without invading the neighboring area. It generally has a spherical or ovoid shape and shares the same characteristics as the surrounding tissue [2], [4]. Usually, benign tumors react successfully to therapies, with a positive prognosis [4].

A malignant tumor, also called cancer, grows rapidly and its size increases constantly because of an imbalance between cell production and cell death. It is characterized by an irregular shape infiltrating and destroying the adjacent tissues. Cancer cells lack differentiation, so they don't perform any function and are highly prone to developing newer genetic mutations. Figure 10 shows a comparison between normal cells forming a tissue and cancer cells creating a tumor mass. Another

important characteristic that distinguishes malignant from benign tumors is their ability to spread into other areas of the body. These later forming tumors are called metastasis and contain the same type of cancer cells as the original cancer site (primary cancer). Malignant tumors can metastasize via lymphatic spread, hematogenous spread or through body cavities and natural passages (Figure 11) [2].

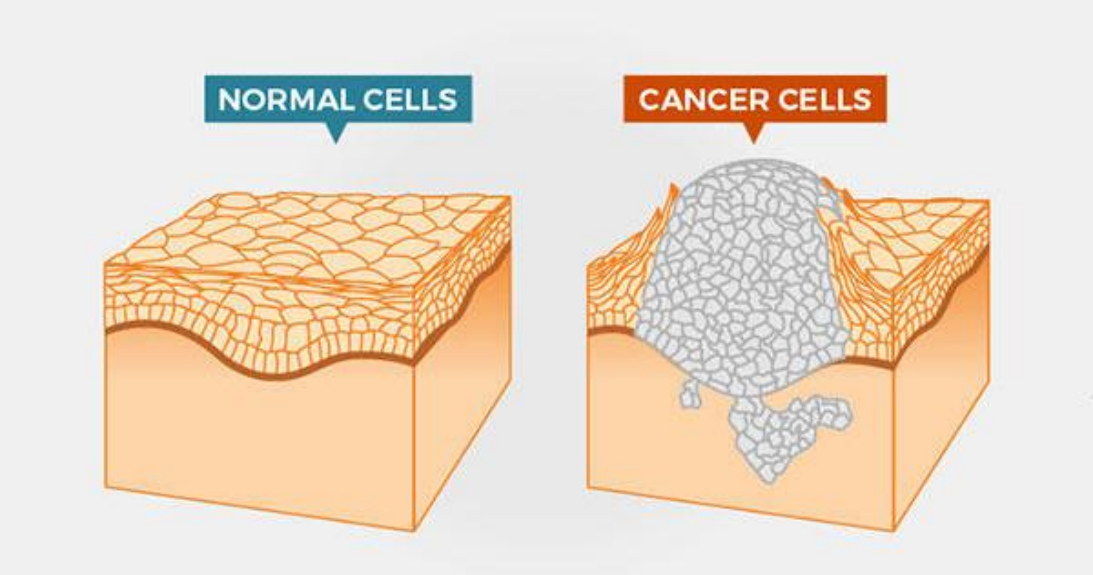

Figure 10. Comparison between normal and cancer cells. Cancer cells have an uncontrolled and rapid growth that leads to the formations of a mass infiltrating in the other tissues [5].

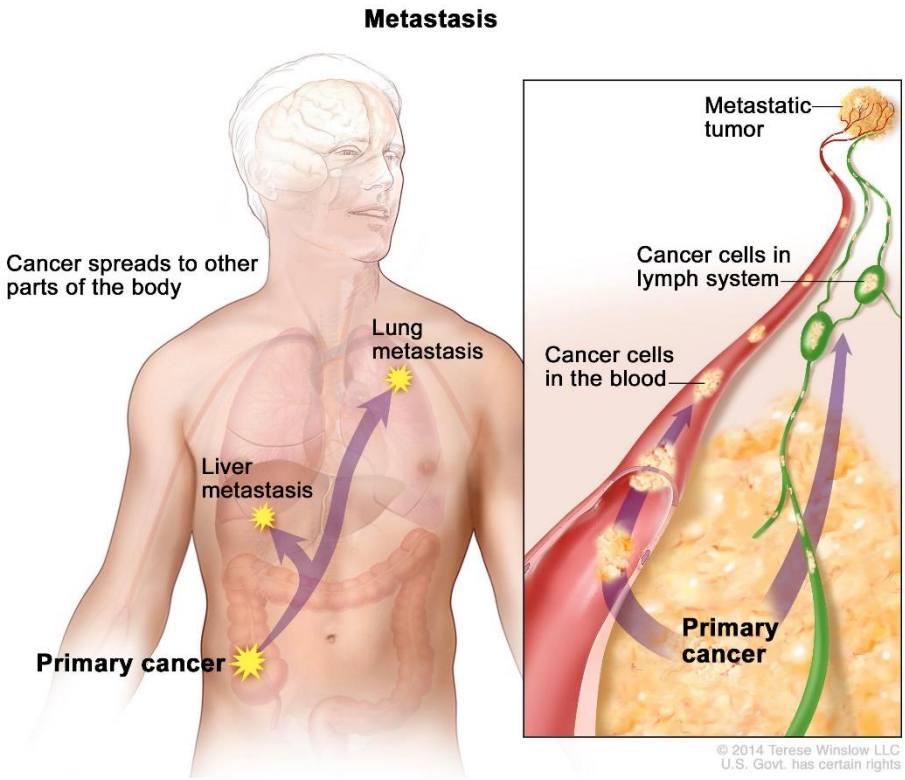

Figure 11. Examples of cancer metastasis. Primary cancer cells can spread through blood and lymphatic vessels, reaching other sites where they develop metastasis [5].

According to the specific type of cells where cancer starts to develop, it is possible to make a classification considering 7 types of cancer:

- **Carcinoma** is a cancer starting in the epithelial cells. It is the most common type of cancer. Depending on the class of epithelial cells, there are different varieties of carcinomas: adenocarcinoma, basal cell carcinoma, squamous cell carcinoma and transitional cell carcinoma.
- **Sarcoma** can develop in bone and soft tissues such as muscle, fat, fibrous tissue, blood and lymphatic vessels. Regarding bones, osteosarcoma is the most common type of cancer.
- **Leukemia** is a type of cancer that originates in bone marrow, where blood cells are produced. It doesn't create a solid tumor mass, but it is characterized by the presence of abnormal white cells which push and hamper the function of normal blood cells.
- **Lymphoma** develops from abnormal lymphocytes (T and B cells) in lymph nodes and lymph vessels, but also in other organs.
- **Multiple myeloma** originates from abnormal plasma cells, which gather in the bone marrow and create a tumor that can spread in the body.
- **Melanoma** is a cancer involving melanocytes, so it can develop in the skin but also in pigmented tissues, such as the eye.
- **Brain and spinal cord tumors** can be benign or malignant and they can have specific names depending on the type of cells where the tumor originates. For example, astrocytic tumor begins in the astrocyte cells (brain cells with a star shape) [5].

2.3 Bone tumors

When an abnormal growth of cells is localized in the bones, a bone tumor is present [6]. If it originally develops in bone tissue, it is called primary bone tumor. This type of tumor can be either benign or malignant. On the other hand, if it originates from other areas of the body (such as the prostate or breast) and it spreads to the bone after some time, it is called secondary or metastatic bone tumor. A metastatic bone tumor is always malignant [6], [7]. Even though bone tumors can have a spontaneous origin, hereditary defects are one of the most possible causes for a great number of them [8].

2.4 Primary bone tumors

2.4.1 Malignant primary bone tumors

Compared to other types of tumors, bone tumors occur rarely [2]. In particular, primary bone cancer comprises only 0.2% of malignancies registered in SEER (Surveillance, Epidemiology, End Result) database in the United States [8]. Despite their low incidence in the population, malignant primary bone tumors are characterized by aggressive growth and great suffering for the patient [9]. In the 1970s the World Health Organization (WHO) created a classification [10] (updated in 2020 [11]) of the different types of primary bone cancer, also called bone sarcoma [12], among which the most important ones are discussed below and shown in Figure 12.

2.4.1.1 Osteosarcoma

Osteosarcoma, or osteogenic sarcoma, is a very common type of primary bone cancer. Its distribution among the population has a bimodal shape, with a first peak of incidence in young people and a second peak in people older than 60 years old [9], [12]. Its origin is not completely well known, but a correlation has been found with mesenchymal stem cells (MSCs), intended to become osteoblasts precursors, carrying mutations in cell cycle regulation pathways [9]. These sarcoma cells have a spindle shape and can synthesize directly osteoid, bone, or both. Some pre-existing bone diseases, such as Paget's disease, are also found responsible for the development of osteosarcoma [2]. Usually, the tumor originates in the metaphysis of long bones and it's associated with pain, swelling of bone extremities and fast metastasis formation, especially in the lungs [9], via the hematogenous route [2]. Only in 5% of the cases osteosarcoma can begin on the surface of the bone, having in this case a slower growth [2].

2.4.1.2 Ewing's sarcoma

This type of sarcoma is very common among young patients and can begin in the diaphysis of long bones or in the bones of the chest wall, with a high possibility of metastasis formation in the lungs, liver, brain and other bones [9]. It is classified as tumor with a miscellaneous origin (either from bone or soft tissue) [11] and it is characterized by small, round tumor cells, with a specific chromosomal translocation [2], [9]. The symptoms include pain, swelling and tenderness of the part, together with fever, leukocytosis and elevated Erythrocyte Sedimentation Rate (ESR) [2]. Ewing sarcoma's prognosis used to be unfavorable, even though with the latest therapies 5 year survival rate increased to 40-80% [2], [9].

2.4.1.3 Chondrosarcoma

The origin of chondrosarcoma is in the chondroblasts, which are the cells responsible for the production of cartilage [2], [13]. It is the most common cancer in adults after osteosarcoma and it

usually develops in the central skeleton bones, such as the pelvis and shoulders [2]. It can be divided into two types: central or peripheral chondrosarcoma, depending on whether it arises in the medullar cavity of diaphysis and metaphysis or in the periosteum of metaphysis, respectively [2]. Most chondrosarcomas are low grade (I and II), which corresponds to a slow growth rate and better prognosis. However, in some cases, chondrosarcomas can belong to the highest grade (III), which is related to a high probability of metastasis, especially in the lungs, liver, kidney and brain [2], [12].

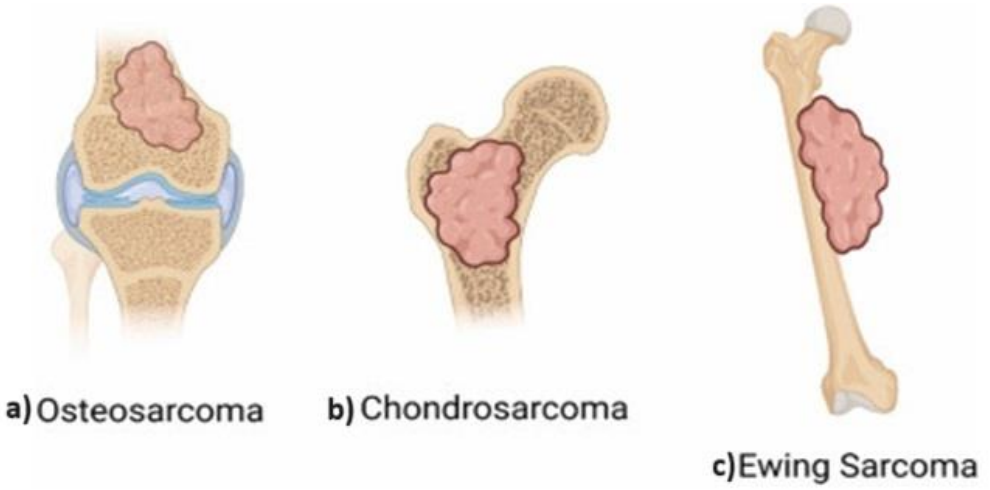

Figure 12. Three different primary bone cancers. a) Osteosarcoma usually originates in the metaphysis of long bones. b) Chondrosarcoma can develop in the medullar cavity of diaphysis or metaphysis. c) Ewing sarcoma can start in the diaphysis of long bones [14].

2.4.2 Benign primary bone tumors

Primary bone tumors can also be benign, without the formation of metastases, and they are not necessarily harmful. However, they can require surgery because of painful conditions or possible transformation into malignancies [2], [12]. A type of classification can be done by considering their histologic derivation [2].

2.4.2.1 Bone forming tumors

Benign primary tumors belonging to this category are osteoma, osteoid osteoma and osteoblastoma. As for osteosarcoma, which is also a bone forming tumor, tumor cells directly synthesize osteoid or bone. Osteoma is a tumor that doesn't occur often and grows slowly in the flat bones of the skull and face. Osteoid osteoma is quite common in young people, it is a small, painful tumor situated in the cortex of long bones. Osteoblastoma is painless and it is located in the medullar cavity of long bones, vertebrae, ribs or ilium [2].

2.4.2.2 Cartilage forming tumors

Osteochondroma, enchondroma and chondroblastoma are benign tumors deriving from cartilage forming cells. Osteochondroma is very common and consists of an abnormal growth of a cartilaginous cap and inner bone, also called exostosis, which can be solitary or multiple. It can develop from the metaphysis of long bones, and it appears without specific symptoms. In many cases, especially with multiple exostoses, this benign tumor can turn into chondrosarcoma. Enchondroma owes its name to the fact that it develops in the center of the inner part of bone, especially in the long bones of hands and feet. Like osteochondroma, enchondroma can be

asymptomatic and can transform into chondrosarcoma, but in some cases, it is also related to pain and pathologic fractures. Chondroblastoma occurs less frequently, and it originates in the area next to the epiphyseal cartilage plate. It can be associated with pain or can be asymptomatic and there is a possibility of reappearance after surgical removal [2].

2.5 Secondary bone tumors

Secondary bone tumors are more common than primary ones. They consist of metastasis belonging to other cancers like breast, lung, prostate, thyroid and kidney cancer. The skeletal system is one of the most common sites for the development of metastasis after the lungs and liver, most frequently via hematogenous spread. The most common bones affected by metastasis are the spine, pelvis, femur, ribs, humerus and skull [2], [8]. Secondary bone tumors more commonly come from carcinomas than sarcomas [2].

When a primary cancer spreads to the bones as a metastasis, the patient often experiences severe pain and a decrease in the quality of his life, because of high risk of fracture due to a progressive weakening of the affected bones [2], [8]. Moreover, the survival probability after metastasis in the bones is low, with 2 or 3 years of survival in case of breast and prostate cancers and only 4 months in case of lung cancer [8]. Figure 13 shows an example of bone metastasis formation via hematogenous spread.

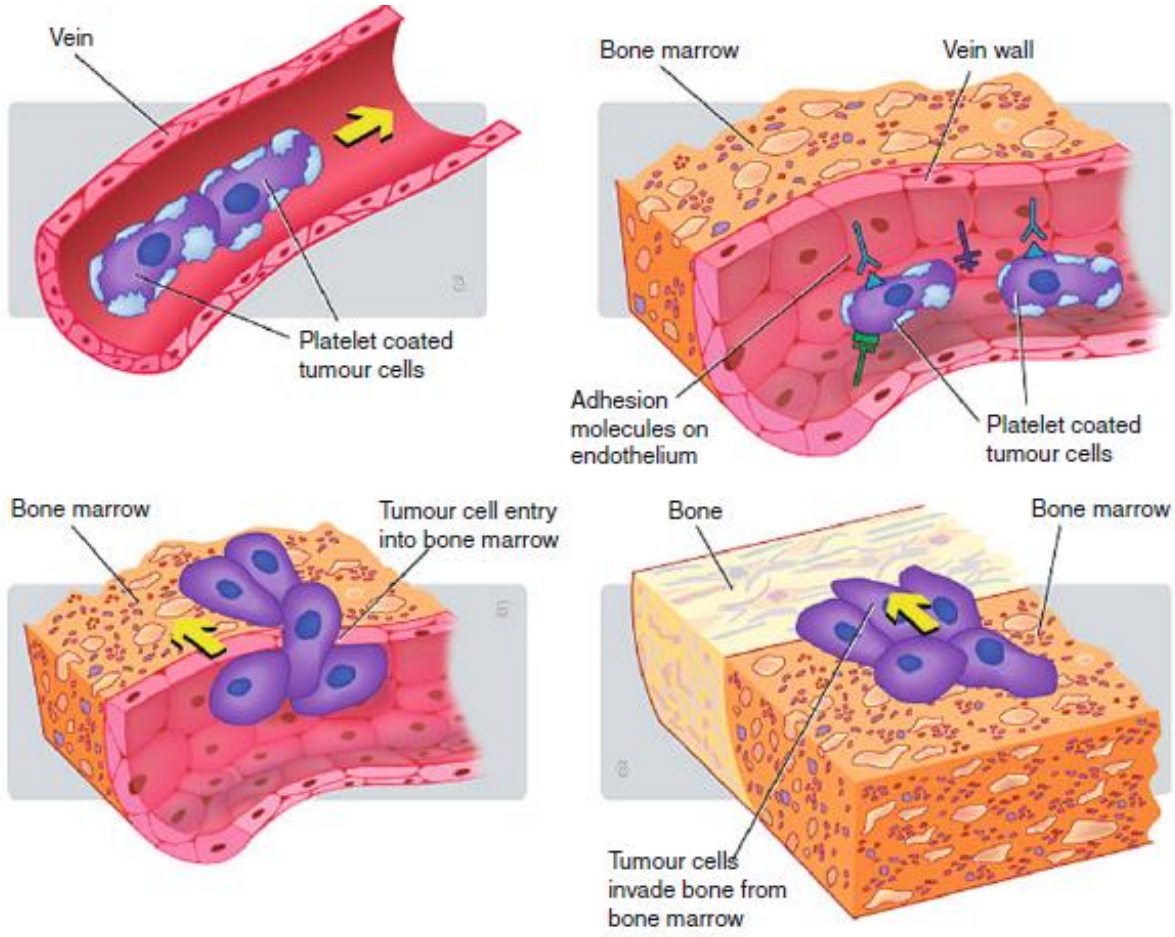

Figure 13. Example of bone metastasis formation. From the top left: cancer cells evade the primary cancer site in the body and enter the circulation. Subsequently, they infiltrate into bone marrow and invade bone [15].

REFERENCES

[1] World Health Organization, International Agency for Research on Cancer, “Global cancer burden growing, amidst mounting need for services,” World Health Organization, Feb. 2024. Accessed: Oct. 08, 2024. [Online]. Available: https://www.who.int/news/item/01-02-2024-global-cancer-burden-growing--amidst-mounting-need-for-services

[2] H. Mohan, *Textbook of pathology*, 6th ed. New Delhi: Jaypee Brothers Medical Publishers, 2013.

[3] National Cancer Institute, “tumor,” *NCI Dictionary of Cancer Terms*. Accessed: Oct. 09, 2024. [Online]. Available: https://www.cancer.gov/publications/dictionaries/cancer-terms/def/tumor

[4] Fondazione CMT, “Tumori benigni e maligni: le differenze,” Aggiornamenti, eventi e news di Fondazione CMT. Accessed: Oct. 09, 2024. [Online]. Available: https://www.fondazionecmt.it/blog-articolo.asp?idb=188

[5] National Cancer Institute, “What Is Cancer?,” Understanding cancer. Accessed: Oct. 09, 2024. [Online]. Available: https://www.cancer.gov/about-cancer/understanding/what-is-cancer

[6] “Overview of Bone Tumors,” MSD Manual. Accessed: Oct. 15, 2024. [Online]. Available: https://www.msdmanuals.com/home/bone-joint-and-muscle-disorders/bone-and-joint-tumors/overview-of-bone-tumors

[7] “Bone cancer,” NHS inform. Accessed: Oct. 15, 2024. [Online]. Available: https://www.nhsinform.scot/illnesses-and-conditions/cancer/cancer-types-in-adults/bone-cancer

[8] R. Forsyth and P. C. W. Hogendoorn, “Epidemiology of primary bone tumors and economical aspects of bone metastases,” in *Bone Cancer*, Elsevier, 2022, pp. 17–23. doi: 10.1016/B978-0-12-821666-8.00038-4.

[9] M. Van Driel and J. P. T. M. Van Leeuwen, “Cancer and bone: A complex complex,” *Archives of Biochemistry and Biophysics*, vol. 561, pp. 159–166, Nov. 2014, doi: 10.1016/j.abb.2014.07.013.

[10] H. A. Sissons, “The WHO Classification of Bone Tumors,” in *Malignant Bone Tumors*, E. Grundmann, Ed., Berlin, Heidelberg: Springer Berlin Heidelberg, 1976, pp. 104–108. doi: 10.1007/978-3-642-80997-2_8.

[11] S. Hwang, M. Hameed, and M. Kransdorf, “The 2020 World Health Organization classification of bone tumors: what radiologists should know,” *Skeletal Radiol*, vol. 52, no. 3, pp. 329–348, Mar. 2023, doi: 10.1007/s00256-022-04093-7.

[12] American Cancer Society, “What Is Bone Cancer?,” About bone cancer. Accessed: Oct. 15, 2024. [Online]. Available: https://www.cancer.org/cancer/types/bone-cancer/about/what-is-bone-cancer.html

[13] Merriam-Webster, “chondroblast.” in Medical. Accessed: Oct. 16, 2024. [Online]. Available: https://www.merriam-webster.com/medical/chondroblast

[14] N. M. Al Sawaftah, W. G. Pitt, and G. A. Husseini, “Incorporating nanoparticles in 3D printed scaffolds for bone cancer therapy,” *Bioprinting*, vol. 36, p. e00322, Dec. 2023, doi: 10.1016/j.bprint.2023.e00322.

[15] U. Kini and B. N. Nandeesh, “Physiology of Bone Formation, Remodeling, and Metabolism,” in *Radionuclide and Hybrid Bone Imaging*, I. Fogelman, G. Gnanasegaran, and H. Van Der Wall, Eds., Berlin, Heidelberg: Springer Berlin Heidelberg, 2012, pp. 29–57. doi: 10.1007/978-3-642-02400-9_2.

3. BONE CANCER TREATMENTS

3.1 Diagnosis of bone cancer

When a suspect of bone cancer is found in a patient, the complete diagnosis can be first made by understanding the location and size of the malignancy. This information is obtained through several imaging techniques, such as X-ray, magnetic resonance imaging (MRI), computed tomography (CT), positron emission tomography (PET) and bone scan [1], [2].

In order to determine the exact nature of the abnormal bone tissue, biopsy is required. Biopsies consist of sampling a part of the affected tissue and analyzing it in a laboratory. They can be performed in two different ways: by inserting a needle through the skin in order to take a part of the tissue, or by a surgical removal of the sample [1], [2].

According to the results obtained regarding size, location, metastasis formation, cancer can be classified into 4 stages, in which number 1 represents a slow growing and small sized cancer, while stage 4 refers to a cancer that already spread to the lymph nodes and generated metastasis [2].

3.2 Bone cancer therapies

Depending on the stage, location and type of cancer, different therapies can be employed [2]. Usually, bone cancers are first treated with surgery, but, according to the situation, other treatments or a combination of them can be applied, such as chemotherapy and radiotherapy [3]. In recent years, other new therapies using drugs that focus on specific aspects of cancer cells have been used, such as targeted therapies, immunotherapy or drugs that affect bone cells.

3.2.1 Surgery

Surgery is the most common treatment for the majority of bone cancers. Usually, biopsy and surgical treatment are performed at the same time, in order to reduce the number of surgical operations the patient undergoes [3], [4]. The surgeon aims at removing all the cancer with a so-called wide excision, so a part of the surrounding healthy tissue will be removed as well to ensure no cancer cells are left and avoid a possibility of cancer recurrence [3]. If bone cancer affects arms or legs, there could be two possible surgery treatments: limb-sparing surgery or amputation. With the first one, some bone is removed leaving a critical-size bone defect, which can be reconstructed with a bone graft or a prosthesis, as shown in Figure 14, so the patient doesn't lose completely the functionality of his original limb. In case the cancer is spread into blood vessels, nerves or limb-sparing is not possible, amputation is required. It implies the complete removal of the limb, which will be replaced by a prosthetic one and has a strong psychological impact on the patient [3], [4], [5].

Surgery can be combined with chemotherapy and radiotherapy before, to reduce the size of the tumor, and after, to destroy the possible remaining cancer cells [6]. After surgery, a patient can face some side effects like pain, excessive bleeding or infections, especially in case of amputation. With limb-sparing surgery, the main complications regard the bone graft and its ability to repair the critical-size bone defects. Physical therapy and rehabilitation are two important steps in the recovering process, otherwise the patient might experience severe problems related to walking and conducting a normal life [4].

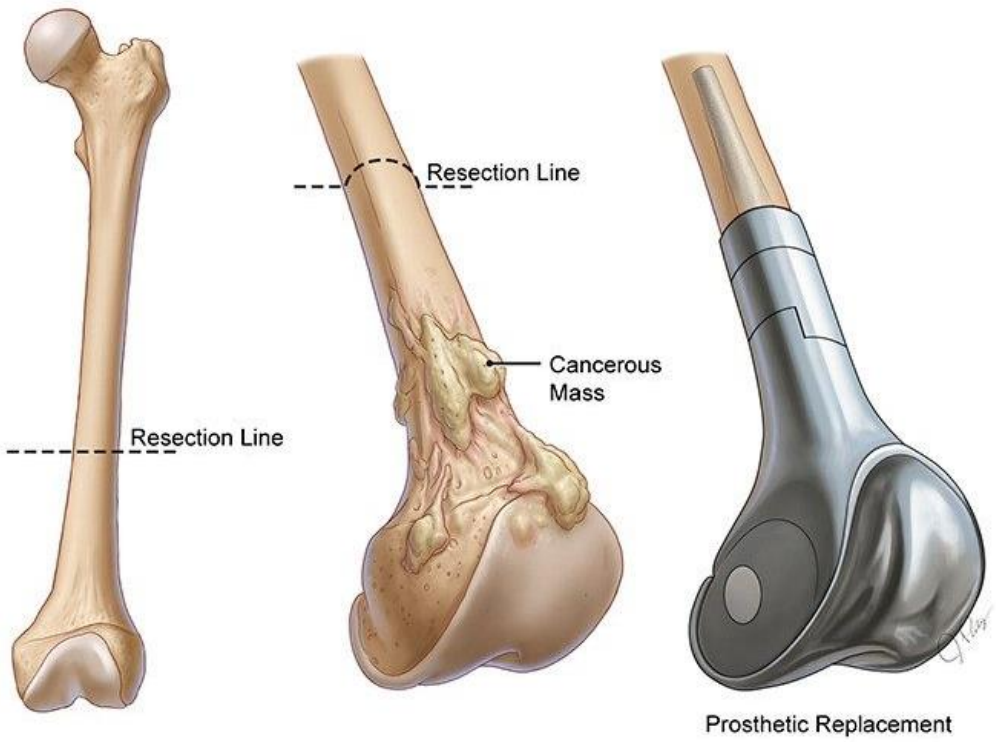

Figure 14. Removal of cancerous mass via surgical resection and replacement with a prosthesis [3].

3.2.2 Chemotherapy

Chemotherapy is a treatment method that makes use of some drugs to cure cancer, such as Doxorubicin or Cisplatin, in most of the cases injected intravenously [2], [7]. The drugs can destroy cancer cells in any part of the body, so in this case this therapy is often used in case of metastasis from bone cancer [7]. The patient usually undergoes cycles of chemotherapy, with breaks between one cycle and the following one [5]. Since chemotherapy not only kills cancer cells, but also might cause damage to normal cells, there is a high possibility of encountering side effects. The most common ones include nausea, vomiting, hair loss, loss of appetite. Moreover, if there is damage in the bone marrow, there would be an impairment in blood cells number, which can lead to fatigue, increased risk of infections and easy bleeding after minor cuts [7].

3.2.3 Radiation therapy

Radiation therapy, or radiotherapy, uses high doses of ionizing radiation to cause localized damage to the DNA of cancer cells, in order to make them stop replicating and die. However, this therapy is not very common because of the low sensitivity of most bone cancers to radiation [8]. Besides its use in combination with surgery and chemotherapy, radiotherapy can also be employed alone if surgery is not possible, or to control cancer symptoms, such as pain and swelling. Side effects are present because the radiation unavoidably damages a part of the normal cells around the cancer, causing skin irritation, hair loss and joint pain in the treated area, in addition to tiredness and sickness [5], [8].

3.2.4 Targeted therapy

Targeted drugs can act on specific mechanisms in cancer cells by blocking the signals that control cancer growth. Kinase inhibitors, such as Dasatinib (Sprycel), are targeted drugs for some types of

bone cancers, where they can stop or slow the growth of the tumor by blocking certain kinase proteins in cancer cells. This type of medicine is taken by the patient as a pill once or twice a day. These drugs are, therefore, different from chemotherapy ones and with different side effects, such as skin rashes, fluid build-up around the eyes, feet or belly [9].

3.2.5 Immunotherapy

Immunotherapy stimulates the immune system in recognizing and destroying cancer cells. Usually, tumor cells can act on immune cell proteins responsible for starting or stopping an immune response, evading in this way the immune attack. Pembrolizumab (Keytruda) is an example of drug that targets PD-1 checkpoint protein on T cells and blocks it. With this action, cancer cells undergo an increased attack from the immune system, resulting in shrinking and reduced growth of the tumor. However, as with every drug, some side effects are present, such as itching, skin rash, muscle or joint pain, shortness of breath, constipation or diarrhea and some serious ones, like infusion reactions (allergic reaction) and autoimmune reactions. The latter can be life-threatening because the immune system attacks other parts of the body, such as the lungs, intestines and liver [9].

3.2.6 Drugs that affect bone cells

These types of drugs interfere with the activity of bone cells. For example, Denosumab (Xgeva) blocks osteoclasts' action because it binds with RANKL protein, hampering the process that transforms pre-osteoclast into mature, resorbing bone osteoclasts. It is injected under the skin and the majority of side effects are quite moderate, even though in rare cases there could be an osteonecrosis of the jaw, especially if some dental treatments are performed together with this therapy [9].

3.3 Hyperthermia

Another possible treatment which could be used for bone cancer, but is still under investigation, is hyperthermia. This therapy uses heat to destroy cancer cells and so reduce the size of a tumor. Nowadays, it is used in the case of advanced cancer together with other therapies, such as radiotherapy and chemotherapy, but its use is not well spread like other conventional treatments because clinical trials are still ongoing [10]. Thermal ablation or thermotherapy are terms included in the definition of hyperthermia, but with a difference: the first one refers to the usage of high temperatures (above 45 °C), while the latter uses a range between 41 °C and 45 °C [11].

3.3.1 Effects of hyperthermia

When a normal tissue is exposed to high temperature blood vessels dilate, blood flow increases and heat is dissipated, so the temperature inside the body does not rise. On the other hand, tumors have a poorly organized blood system due to disorganized angiogenesis from tumor cells, so their ability to dissipate heat is highly reduced. The increase of temperature leads to molecular and cellular alterations that end up with cell death via necrosis or apoptosis [11]. Figure 15 shows the two different outcomes between heating of normal tissue and tumors.

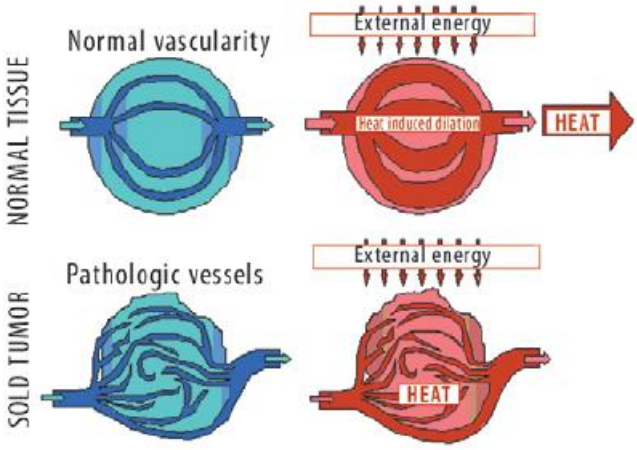

Figure 15. Different outcomes in blood vessel dissipation of heat [12].

Some studies on cultured cells (Chinese hamster ovarian cells, CHO) [13] showed that when cells are exposed to heat for a certain incubation time, there are two steps in the process of cell killing, as reported in Figure 16. At the beginning, cells stop growing and this phase is still reversible and non-lethal. Subsequently, cells start to die following an exponential curve. This study shows how cytoplasmatic and membrane proteins denaturation is strictly correlated to the cytotoxic effect of hyperthermia [13].

Indeed, the thermal energy dose that induces exponential cell death (activation energy) is close to the one that causes denaturation of these proteins (140 kcal/mol) [13]. The denatured/unfolded proteins can form high molecular mass protein aggregates, which are strictly correlated to the loss of structural integrity of subcellular components, and so to the loss of cellular function and cell death [14]. Unfolding and aggregation can involve proteins responsible for DNA synthesis and repair, or proteins of the cytoskeleton, leading to cell cycle arrest and disequilibrium of membrane permeability [15].

In clinical research, CEM 43 °C T90 is considered a very convenient dosimetric parameter. It represents *"the cumulative equivalent minutes at a standard targeted treatment temperature of 43 °C obtained within 90% of the tumor volume"* [12]. A dose of 10 CEM 43 °C T90 during hyperthermia is considered to be effective for the patient, because heating 90% of the tumor at 43 °C for cumulative 10 minutes doubles the probability of obtaining a complete response after hyperthermia and radiotherapy than after radiotherapy alone [12].

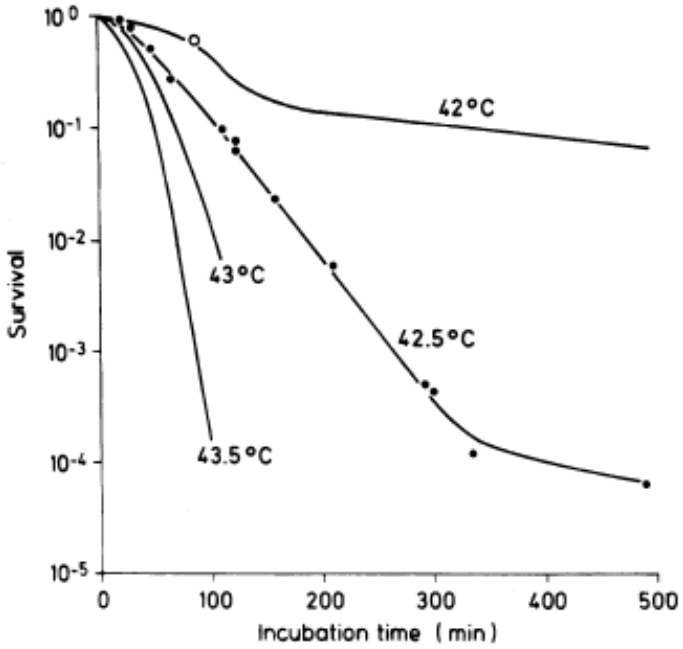

Figure 16. Surviving fraction of CHO cells heated at different temperatures [13].

Depending on the cell cycle phase, heat sensitivity can change. Cells are more susceptible to heat during the mitotic phase, when hyperthermia leads to damage in the mitotic apparatus and mitosis results inefficient. During S-phase, cells are also heat-sensitive and can undergo chromosomal damage. In both cases, cells show a slow cell death. G1-phase cells are less sensitive during hyperthermia without reporting any microscopic damage, but they undergo a rapid death after the treatment. These various reactions to heat exposure in cell behavior explain that the molecular mechanisms leading to cell death can be diverse [13].

3.3.1.1 Thermotolerance

When cells are exposed to fractionated hyperthermia treatments, a phenomenon called thermotolerance (TT) develops. Thermotolerance is a transient resistance to thermal cytotoxicity during heat treatments after heat pre-exposure. It is strictly connected to an up-regulation of a class of proteins called heat-shock proteins (HSP) and to other adaptation processes which make cells less susceptible to future heat treatments, developing a resistance against thermal denaturation and aggregation of their proteins [13], [14], [16]. The mechanism of resistance can, in some cases, result in attenuated protein initial damage or, in other cases, in better repair and recovery of the harmed protein [16].

If thermotolerance develops at a temperature below 42 °C during hyperthermia, it is defined as chronic TT. In this case, cells stop dying after a certain period of exposure and, later than, they can be resistant even at higher temperatures for a while. Acute TT, on the other hand, appears if cell are first exposed for a short time to a temperature above 43 °C, and then for another period of time at 37 °C. Nearly all living organisms show the presence of thermotolerance, mammalian cells included [16].

As shown in Figure 17, where the pre-exposure temperature is 40 °C, thermotolerance varies depending on the length of the pre-heating period. Indeed, more cells survive if the pre-heating

period is longer [13]. It is, therefore, a phenomenon to consider when hyperthermia treatment is applied.

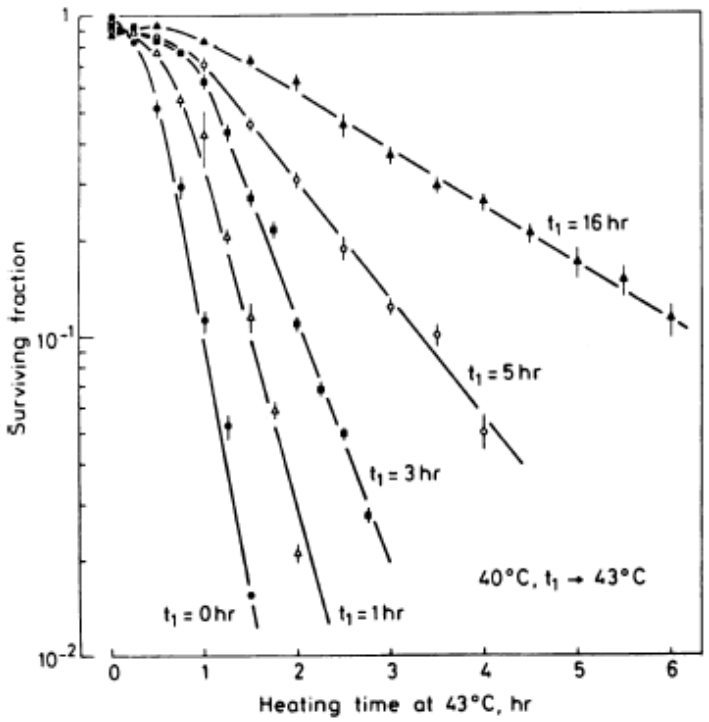

Figure 17. Thermotolerance in CHO cells exposed to 43 °C and pre-heated at 40 °C for different periods of time [13].

3.3.1.2 Alterations in tumor blood flow and microenvironment

Hyperthermia treatment temperature can produce two main different outcomes regarding the alterations in tumor blood flow and microenvironment, as shown in some *in vivo* studies [13]. If the tumor is treated with temperatures above 42 °C, tumor blood flow decreases together with some morphological changes, such as endothelial swelling, microthrombosis and change of the viscosity of blood cell membrane. As a consequence, there is a lack of oxygen and nutrient supply, inducing intratumoral acidosis [13]. On the other hand, if hyperthermia temperature is below 42 °C, tumor blood flow, and so oxygen content, might increase. This phenomenon can improve the result of a subsequent radiotherapy, which is more effective in tumor with higher oxygen supply, or a subsequent chemotherapy, because of the increased blood flow [13].

3.3.2 Hyperthermia and radiotherapy

As discussed briefly before, some *in vitro* studies [13] and clinical trials [11] showed that hyperthermia and radiotherapy can be combined together to obtain better results in cancer treatment. The increase in cell killing during radiation therapy with a previous heat treatment is defined as *thermal radiosensitization*. This phenomenon can be quantified with the Thermal Enhancement Ratio (TER) by dividing the survival fraction of cells treated only with radiotherapy by the survival fraction of cells treated with both radiotherapy and hyperthermia [13]. If oxygen supply increases (temperature of heat treatment below 42 °C), radiotherapy proves to be more effective, because radiation-induced oxygen radicals are easier to form. These radicals can kill cancer cells

because of the production of double-strand breaks in DNA [11]. Some factors like temperature, interval between heat and radiation and treatment sequence influence the final outcome [13].

3.3.3 Hyperthermia and chemotherapy

Similarly, *in vitro* studies, animal studies [13] and clinical trials [11] proved that some chemotherapy drugs can enhance their cytotoxicity towards cancer cells when they are at elevated temperatures. In this case the phenomenon is called *thermal chemosensitization*, and it is measured with the TER as the ratio between survival fractions of cells at elevated temperature and at normal temperature, given a certain drug level. Chemotherapeutic drugs can show different behaviors when they interact with heat. In particular, they can increase their cytotoxicity in a linear way with increasing temperature, or they can increase significantly their cytotoxicity only after a certain temperature level is reached (threshold behavior), or do not have any interaction with heat (independent behavior) [13].

3.3.4 Types of hyperthermia treatment

Depending on the extension of the tumor in the body, hyperthermia treatment can be local, regional, or whole-body.

3.3.4.1 Local hyperthermia

When the tumor is small (up to 5-6 cm in the longest diameter [12]) and confined, local heating is applied. The heating source can be a generator of radio waves (ranging from 100kHz to 150 MHz), microwaves (from 433 MHz to 2450 MHz) or ultrasound waves (also called Focused Ultrasound Technique) [12], [17].

Depending on the area of the body, three possible local treatments are employed:

- **External hyperthermia** is used when the tumor is on or just beneath the skin. A heating device, like a superficial applicator or an antenna, is applied near the affected part [12], [18]. Tiny thermometers can be inserted through tubes or needles in the anaesthetized tumor to monitor the temperature [12].
- **Intraluminal or endocavitary hyperthermia** is employed when the tumor is inside or near body cavities, like cancer of prostate, rectum, cervix, esophagus. In this case, the heat comes from a probe which is inserted inside the cavity [18].
- **Interstitial hyperthermia** is used if a tumor is deep in the body, such as a brain tumor. A probe or a needle connected to the heating system is deeply inserted in the tumor while the patient is under anesthesia, whereas other probes are used for measuring the temperature [12], [18]. Ultrasound imaging technique, Magnetic Resonance Imaging (MRI) or Computed Tomography (CT) can be used for monitoring the procedure. Radiofrequency ablation (RFA) is a common type of interstitial hyperthermia which uses high energy radio waves to kill cancer cells at a temperature over 50 °C, causing vascular stasis, cellular coagulation and tissue necrosis [12], [17], [18].

Local hyperthermia side effects can include pain, infection, bleeding, burns and blistering, with possible damage to the skin, nerves and muscles in the treated area [17]. However, concurrent administration of water boluses during the treatment can prevent the formation of burns and blisters, keeping skin temperature at 37 °C [12].

3.3.4.2 Regional hyperthermia

Regional hyperthermia treats larger areas of the body, for example organs or limbs, affected by a tumor. There are three types of regional treatments [10].

- **Deep tissue therapy** uses external devices placed in a ring pattern around the affected area of the patient. The devices consist of arrays of antennas, ranging from 70 to 150 MHz, which emit microwaves or radiofrequency energy raising the temperature of the body portion up to 41-42 °C [12], [17].
- **Regional perfusion** is used for cancers in the arms or in the legs (melanoma), or in some organs like liver and lungs. Heat is delivered by isolating the blood supply to that specific part of the body, and letting it pass through a heating system before the reintroduction into the circulation. Chemotherapy is often pumped at the same time [12], [17].
- **Hyperthermia intraperitoneal chemotherapy (HIPEC)** treats cancers in the abdominal cavity where the intestines, stomach and liver are located (peritoneal cavity). A warmed washing fluid (41.0-42.5 °C) with chemotherapy drugs is delivered during or after surgery [12], [18].

Regional hyperthermia is related to less systemic effects compared to whole-body treatment [18]. Some common and transitory side effects include diarrhea, nausea and vomiting [17]. Swelling, bleeding and blood clots can be present with perfusion but they improve after treatment [18].

3.3.4.3 Whole-body hyperthermia (WBH)

For patients with metastatic disease, hyperthermia therapy aims at destroying cancerous cells distributed throughout the organism by increasing the temperature of the whole body. This can be achieved by using thermal chambers, hot water blankets or infrared radiators. The patient is under general anesthesia, or deep sedation, and the temperature can reach 42 °C for 60 minutes (extreme WBH) or 39.5-41.0 °C for 3-4 hours (moderate WBH). Even though among the different heat treatments WBH allows to reach the most homogeneous thermal distribution, a high probability of complications is present. Side effects are similar to the regional ones, but in some rare cases there could be serious problems related to the heart, blood vessels and major organs [12], [17].

3.3.5 Hyperthermia and bone cancer

Concerning bone cancer treatment, hyperthermia is considered as a possible adjuvant therapy and it has been demonstrated that it can contribute to the reduction of metastasis formation in osteosarcoma [19]. Different types of hyperthermia have been studied, focusing on the use of microwaves, radiofrequency and laser ablation [20], [21], [22], [23]. However, one of the most important limitations concerning these methods is the difficulty in reaching a high temperature in deep regions of the body, as well as heating selectively a specific area and leaving the surrounding tissue unaltered [24], [25]. Because of these reasons, magnetic nanoparticle-mediated hyperthermia has been proposed as an alternative, since it can reach bone structures in depth, it is considered non-invasive and more tissue-specific [25], [26], [27].

3.3.6 Magnetic hyperthermia

Magnetic hyperthermia consists of using an alternating magnetic field (AMF) to heat up magnetic nanoparticles (MNPs) which can convert electromagnetic waves into thermal energy [28].

When talking about magnetic materials, ferromagnetic and ferrimagnetic ones make a distinction from the other types because, under a certain temperature (Curie temperature), they can maintain a permanent magnetization, even after the removal of a magnetic field. They are both characterized by the presence of magnetic domains, in which the atomic magnetic moments of the same domain are parallel to each other in the case of ferromagnetic materials, or antiparallel but with different magnitudes in the case of ferrimagnetic ones. In both situations, they exhibit a strong response when an external magnetic field is applied, aligning the magnetic moments of the domains parallel to the direction of the field [29].

As shown in Figure 18, the way the magnetization M changes as a function of the magnetic field strength H is characterized by the presence of a hysteresis loop. In particular, when H returns to zero there is a residual magnetization Mr, while the coercivity Hc corresponds to the value of H for which magnetization is zero [29].

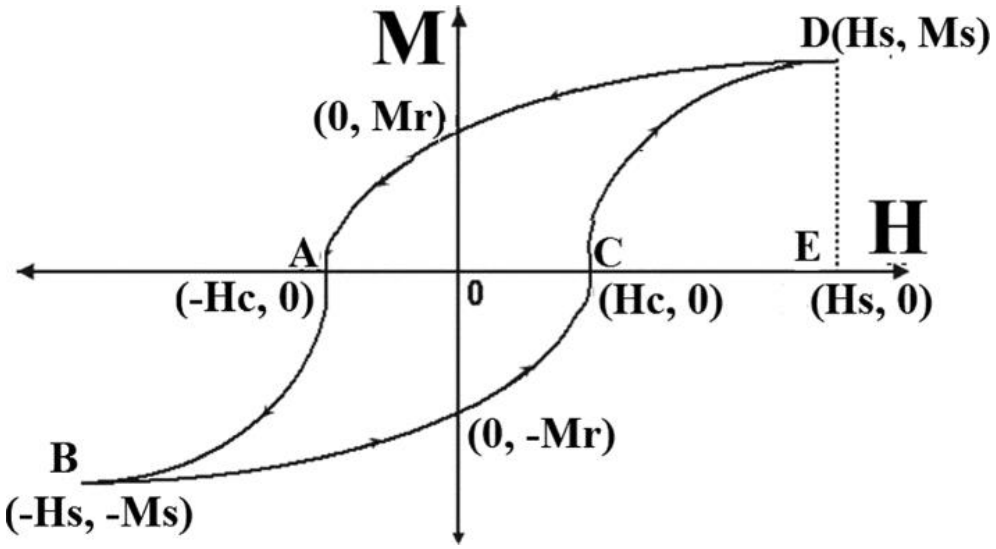

Figure 18. Magnetization as a function of the magnetic field strength [30].

Size is a crucial factor in terms of the way magnetic behavior can change. While in bulk ferromagnetic and ferrimagnetic materials there are multidomains, nanometer scale particles (nanoparticles NPs) only have a single domain. With a single domain, NPs can be divided into two types, depending on their magnetic behavior: ferromagnetic NPs and superparamagnetic NPs. When the particle size decreases from multidomain to single domain situation, coercivity first increases and reaches a maximum value, then it starts decreasing with NPs still behaving in a ferromagnetic way. If the size is further reduced, Hc reaches zero and superparamagnetic behavior starts, as shown in Figure 19 [29].

Superparamagnetic NPs can reach a high saturation magnetization when H is applied and lose their magnetism when H is removed. This is considered as an aspect of interest in biomedical applications because they behave as magnets only in the presence of a magnetic field, therefore they can prevent possible particle agglomeration due to a residual magnetization. Moreover, the mechanism of heat release makes them suitable for magnetic hyperthermia applications [29].

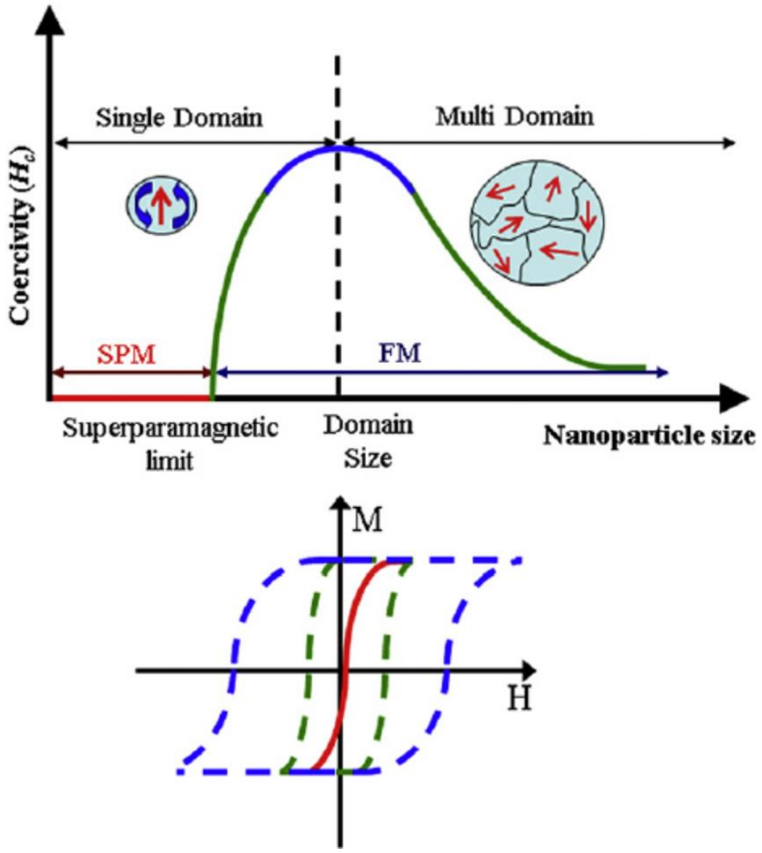

Figure 19. Above: coercivity Hc as a function of nanoparticle size. Below: magnetization M as a function of magnetic field strength H referring to the 3 different situations: in blue Hc is maximum, in green Hc is non-zero and in red Hc is zero [31].

3.3.6.1 Heat generation in magnetic hyperthermia

The generation of heat in magnetic hyperthermia treatments is based on the magnetization reversal process that occurs when MNPs are subjected to an alternating magnetic field. The mechanisms of heat generation can be divided into two groups: hysteresis losses and susceptibility losses [29].

Hysteresis losses occur in multi and single domain ferromagnetic NPs, in which a loss of energy is dissipated as heat because of a delay in the variation of magnetization when AMF is applied. This delay corresponds to the hysteresis loop, whose area represents the amount of heat produced [29].

Susceptibility losses characterize superparamagnetic NPs, which do not show the presence of hysteresis loop. Two mechanisms participate in this type of loss: Néel and Brownian relaxation. Néel relaxation occurs when the magnetic moment of the particle rotates in response to an external field, keeping the physical orientation of the particle fixed. This process dissipates heat because it happens with a certain delay, since the magnetic anisotropy energy barrier ΔE of the particle needs to be overcome. The magnetic anisotropy energy barrier depends on magnetic anisotropy and volume of MNPs, and it is defined as in Equation 1 [29].

$$\Delta E = KV$$

Equation 1. Magnetic anisotropy energy barrier [29].

Where K is the anisotropy constant and V is the MNPs volume [29].

Brownian relaxation occurs when the whole particle rotates in the medium where it is located to align with H, with magnetization orientation fixed in the crystalline lattice. In this case, the type of medium in which the MNPs are immersed is important for determining how much Brownian relaxation contributes to heat production. Indeed, if the medium is more viscous, the contribution will be lower because the particle movement is hindered [29].

Specific absorption rate (SAR) defines the thermal energy dissipation, and it is calculated as the ratio between thermal power dissipation and mass of MNPs, as shown in Equation 2. It is expressed as W/g [29].

$$SAR = \frac{P_{diss}}{M_{MNP}}$$

Equation 2. Specific absorption rate [29].

Higher SAR corresponds to higher dissipation and so higher heat generation. The magnetic field parameters can be adjusted to obtain a higher dissipation. However, there is a limit (Brezovich value) due to human tolerance defined as $H \cdot f < 5 \cdot 10^9 A/ms$. This limit should be respected to ensure safety and avoid damage to healthy tissues [29].

3.3.6.2 Superparamagnetic Iron Oxide Nanoparticles (SPIONS)

Different types of metals have been employed for MNPs, such as iron, cobalt, nickel, manganese, zinc, gadolinium, magnesium, including their alloys and oxides. In particular, iron oxide nanoparticles possess some important characteristics that make them a good candidate for hyperthermia treatment [29].

Superparamagnetic Iron Oxide Nanoparticles (SPIONS) are characterized by an iron oxide core, which can be made of magnetite (Fe_3O_4), maghemite (Y- Fe_2O_3) or hematite (α- Fe_2O_3). Usually, magnetite is the most used iron oxide type. Bulk magnetite is a ferrimagnetic material that contains iron ions Fe^{2+} and Fe^{3+} in the ratio of 1:2 [32]. When the diameter of magnetite NPs is 20 nm or less, iron oxide nanoparticles become superparamagnetic, revealing their magnetic properties only when an external magnetic field is applied [29], [32].

As shown in Figure 20, around the iron oxide core there is usually a coating made of organic acids (like citric acid) or biocompatible and hydrophilic polymers, or polysaccharides. The presence of the coating is important to reach colloidal stability in aqueous media, otherwise SPIONS tend to aggregate and, due to their hydrophobic nature, plasma proteins can coat them when they are injected into blood circulation (phenomenon of opsonization), favoring a rapid clearance from the blood. Thanks to the hydrophilic coatings, SPIONS can avoid opsonization and are less prone to aggregate because of electrostatic interactions and steric hindrance [29], [32].

SPIONS toxicity is strongly dependent on the type of coating, which can prevent the release of iron ions and be responsible for the type of interactions with the biological environment. Even though iron oxide is considered safe by both Food and Drug Administration (FDA) and European Medicines Agency (EMA), one of the main issues concerning SPIONS effects on the human body is the production of Reactive Oxygen Species (ROS), because of the reaction between ferrous ions (Fe^{2+}), hydrogen peroxide and oxygen (Fenton reaction). ROS cause oxidative stress, with damage to DNA, proteins, lipids and polysaccharides in the cell [29], [32].

Different studies [33], [34] have been conducted about the concentration of SPIONS to be considered safe in the human body, proving that a concentration below 100-200 µg/ml was not cytotoxic. It was also underlined how the coating has a strong impact on the cytotoxic effects and on the blood-half lives of SPIONS, which can vary from 1 to 24-36 hours [32]. The liver and the spleen are the usual sites for SPIONS accumulation, where SPIONS are phagocytosed by macrophages if their diameter is over 100 nm, or undergo pinocytosis if it is under 30 nm, while smaller NPs (<10 nm) are removed by the kidneys [15], [32], [35]. Further studies are needed to fully understand the toxicity of SPIONS, but so far the type of adverse effects are not considered severe nor frequent, with a low toxicity profile [32], [36].

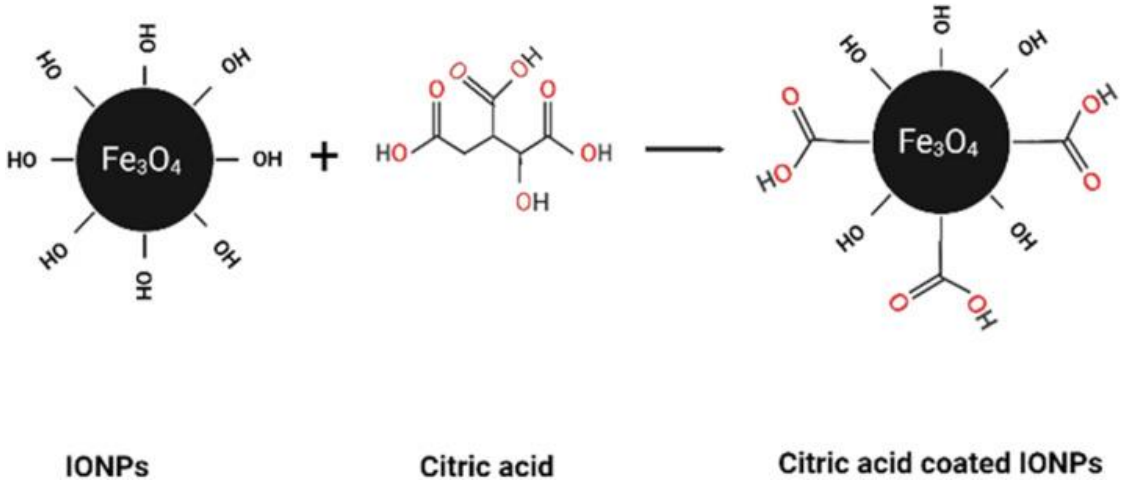

Figure 20. Coating of an iron oxide nanoparticle with citric acid [37].

In magnetic hyperthermia, SPIONS are usually directly injected into the tumor area or in the veins as a suspension of stabilized SPIONS called magnetic fluid. If SPIONS have a specific coating which makes them targeted to the tumor cells, they can easily accumulate in that area and within cancer cells, releasing the energy in a very restricted environment when heated up and reducing the damage to the surrounding healthy tissues [15], [32], [36].

Despite hyperthermia, SPIONS can be employed for many other applications:

- **Drug delivery**. SPIONS could be used as drug carriers and delivered to a specific site of the body by using an external magnetic field. The type of coating would be responsible for the protection of the nanoparticles from the immune system and the encapsulation of the drug [32].
- **MRI contrast agents**. SPIONS can be used as contrast agents in Magnetic Resonance Imaging (MRI) for the visualization of specific tissues, such as cancer, or for the *in vivo* tracking of iron oxide doped stem cells. Antibodies can be combined with NPs to target the specific zone of the body [32], [36].
- **Conjugation with antibodies.** Antibodies can be coupled with SPIONS for oncological treatments because of their ability to target specific patterns in proteins tertiary structure [32].
- **Tissue engineering.** SPIONS can be incorporated in biodegradable scaffolds, making them magnetic, for tissue engineering applications [36].

- **Biosensors.** Surface of SPIONS can be modified with receptors for targeting specific cells regarding a certain biological environment or a certain biological substance [36].

REFERENCES

[1] NHS, “Diagnosis, Bone cancer.” Accessed: Oct. 17, 2024. [Online]. Available: https://www.nhs.uk/conditions/bone-cancer/diagnosis/

[2] Mayo clinic, “Bone cancer.” Accessed: Oct. 17, 2024. [Online]. Available: https://www.mayoclinic.org/diseases-conditions/bone-cancer/diagnosis-treatment/drc-20350221#:~:text=Bone%20cancer%20treatments%20include%20surgery,overall%20health%20and%20your%20preferences.

[3] The University of Texas MD Anderson Cancer Center, “Bone Cancer Treatment,” Bone cancer. Accessed: Oct. 17, 2024. [Online]. Available: https://www.mdanderson.org/cancer-types/bone-cancer/bone-cancer-treatment.html

[4] American Cancer Society, “Surgery for Bone Cancer,” Bone cancer. Accessed: Oct. 17, 2024. [Online]. Available: https://www.cancer.org/cancer/types/bone-cancer/treating/surgery.html

[5] NHS, “Treatment, Bone cancer.” Accessed: Oct. 17, 2024. [Online]. Available: https://www.nhs.uk/conditions/bone-cancer/treatment/

[6] SARCOMA oncology center, “Bone Cancer Symptoms and Effective Treatment Options Available at Sarcoma Oncology Center.” Accessed: Oct. 17, 2024. [Online]. Available: https://sarcomaoncology.com/blog/bone-cancer-symptoms-and-effective-treatment-options-available-at-sarcoma-oncology-center/

[7] American Cancer Society, “Chemotherapy for Bone Cancer,” Bone cancer. Accessed: Oct. 21, 2024. [Online]. Available: https://www.cancer.org/cancer/types/bone-cancer/treating/chemotherapy.html

[8] American Cancer Society, “Radiation Therapy for Bone Cancer,” Bone cancer. Accessed: Oct. 21, 2024. [Online]. Available: https://www.cancer.org/cancer/types/bone-cancer/treating/radiation.html

[9] American Cancer Society, “Targeted Therapy and Other Drugs for Bone Cancer,” Bone cancer. Accessed: Oct. 23, 2024. [Online]. Available: https://www.cancer.org/cancer/types/bone-cancer/treating/surgery.html

[10] Cleveland Clinic, “Hyperthermia Therapy Overview.” Accessed: Oct. 24, 224AD. [Online]. Available: https://my.clevelandclinic.org/health/treatments/17114-hyperthermia-therapy

[11] O. Bretcanu, “Mini Review: Hyperthermia Treatment for Bone Cancers,” *NACS*, vol. 6, no. 4, Dec. 2021, doi: 10.31031/NACS.2021.06.000643.

[12] A. Chicheł, J. Skowronek, M. Kubaszewska, and M. Kanikowski, “Hyperthermia – description of a method and a review of clinical applications,” *Reports of Practical Oncology & Radiotherapy*, vol. 12, no. 5, pp. 267–275, Sep. 2007, doi: 10.1016/S1507-1367(10)60065-X.

[13] Bert Hildebrandt *et al.*, “The cellular and molecular basis of hyperthermia,” *Critical Reviews in Oncology/Hematology 43 (2002)*, pp. 33–56, Jul. 2001.

[14] H. H. Kampinga, “Thermotolerance in mammalian cells protein denaturation and aggregation, and stress proteins,” *Journal of Cell Science*, vol. 104, no. 1, pp. 11–17, Jan. 1993, doi: 10.1242/jcs.104.1.11.

[15] M. Szwed and A. Marczak, “Application of Nanoparticles for Magnetic Hyperthermia for Cancer Treatment—The Current State of Knowledge,” *Cancers*, vol. 16, no. 6, p. 1156, Mar. 2024, doi: 10.3390/cancers16061156.

[16] M. Dewhirst, B. L. Viglianti, M. Lora-Michiels, P. J. Hoopes, and M. A. Hanson, “Thermal dose requirement for tissue effect: experimental and clinical findings,” presented at the Biomedical Optics 2003, T. P. Ryan, Ed., San Jose, CA, Jun. 2003, p. 37. doi: 10.1117/12.476637.

[17] American Cancer Society, “Hyperthermia to Treat Cancer.” Accessed: Oct. 24, 2024. [Online]. Available: https://www.cancer.org/cancer/managing-cancer/treatment-types/hyperthermia.html

[18] National Cancer Institute, “Hyperthermia to Treat Cancer,” About cancer. Accessed: Oct. 24, 2024. [Online]. Available: https://www.cancer.gov/about-cancer/treatment/types/hyperthermia

[19] K. Nakajima, T. Yanagawa, H. Watanabe, and K. Takagishi, “Hyperthermia reduces migration of osteosarcoma by suppression of autocrine motility factor,” *Oncology Reports*, vol. 28, no. 6, pp. 1953–1958, Dec. 2012, doi: 10.3892/or.2012.2066.

[20] Q. Fan *et al.*, “Surgical treatment of bone tumors in conjunction with microwave-induced hyperthermia and adjuvant immunotherapy. A preliminary report,” *Chin Med J (Engl)*, vol. 109, no. 6, pp. 425–431, Jun. 1996.

[21] R. L. Cazzato *et al.*, “Percutaneous microwave ablation of bone tumors: a systematic review,” *Eur Radiol*, vol. 31, no. 5, pp. 3530–3541, May 2021, doi: 10.1007/s00330-020-07382-8.

[22] J. Palussière, A. Pellerin-Guignard, E. Descat, F. Cornélis, and F. Dixmérias, “Radiofrequency ablation of bone tumours,” *Diagnostic and Interventional Imaging*, vol. 93, no. 9, pp. 680–684, Sep. 2012, doi: 10.1016/j.diii.2012.06.008.

[23] A. Gangi, H. Alizadeh, L. Wong, X. Buy, J.-L. Dietemann, and C. Roy, “Osteoid Osteoma: Percutaneous Laser Ablation and Follow-up in 114 Patients,” *Radiology*, vol. 242, no. 1, pp. 293–301, Jan. 2007, doi: 10.1148/radiol.2421041404.

[24] K. Takegami *et al.*, “New ferromagnetic bone cement for local hyperthermia,” *J. Biomed. Mater. Res.*, vol. 43, no. 2, pp. 210–214, 1998, doi: 10.1002/(SICI)1097-4636(199822)43:2<210::AID-JBM16>3.0.CO;2-L.

[25] A. Yazdanpanah *et al.*, “Threatening sarcoma with combinational therapies: Magnetic hyperthermia using nanoparticles,” *Nano Select*, vol. 4, no. 6, pp. 353–367, Jun. 2023, doi: 10.1002/nano.202300008.

[26] K. Yu, H. Zhou, Y. Xu, Y. Cao, Y. Zheng, and B. Liang, “Engineering a triple-functional magnetic gel driving mutually-synergistic mild hyperthermia-starvation therapy for osteosarcoma treatment and augmented bone regeneration,” *J Nanobiotechnol*, vol. 21, no. 1, p. 201, Jun. 2023, doi: 10.1186/s12951-023-01955-7.

[27] A. Matsumine *et al.*, “A novel hyperthermia treatment for bone metastases using magnetic materials,” *Int J Clin Oncol*, vol. 16, no. 2, pp. 101–108, Apr. 2011, doi: 10.1007/s10147-011-0217-3.

[28] X. Liu *et al.*, “Comprehensive understanding of magnetic hyperthermia for improving antitumor therapeutic efficacy,” *Theranostics*, vol. 10, no. 8, pp. 3793–3815, 2020, doi: 10.7150/thno.40805.

[29] A. Rajan and N. K. Sahu, “Review on magnetic nanoparticle-mediated hyperthermia for cancer therapy,” *J Nanopart Res*, vol. 22, no. 11, p. 319, Nov. 2020, doi: 10.1007/s11051-020-05045-9.

[30] A. H. El-Sayed and M. A. Hamad, “Simulated Hysteretic Loops for YBa2Cu3O7,” *J Supercond Nov Magn*, vol. 31, no. 10, pp. 3163–3166, Oct. 2018, doi: 10.1007/s10948-018-4591-1.

[31] M. Mehrmohammadi, K. Y. Yoon, M. Qu, K. P. Johnston, and S. Y. Emelianov, “Enhanced pulsed magneto-motive ultrasound imaging using superparamagnetic nanoclusters,” *Nanotechnology*, vol. 22, no. 4, p. 045502, Jan. 2011, doi: 10.1088/0957-4484/22/4/045502.

[32] J. Dulińska-Litewka, A. Łazarczyk, P. Hałubiec, O. Szafrański, K. Karnas, and A. Karewicz, “Superparamagnetic Iron Oxide Nanoparticles—Current and Prospective Medical Applications,” *Materials*, vol. 12, no. 4, p. 617, Feb. 2019, doi: 10.3390/ma12040617.

[33] D.-W. Han *et al.*, “Subtle cytotoxicity and genotoxicity differences in superparamagnetic iron oxide nanoparticles coated with various functional groups,” *IJN*, p. 3219, Dec. 2011, doi: 10.2147/IJN.S26355.

[34] R. M. Patil *et al.*, “Comprehensive cytotoxicity studies of superparamagnetic iron oxide nanoparticles,” *Biochemistry and Biophysics Reports*, vol. 13, pp. 63–72, Mar. 2018, doi: 10.1016/j.bbrep.2017.12.002.

[35] H. Fatima, T. Charinpanitkul, and K.-S. Kim, “Fundamentals to Apply Magnetic Nanoparticles for Hyperthermia Therapy,” *Nanomaterials*, vol. 11, no. 5, p. 1203, May 2021, doi: 10.3390/nano11051203.

[36] X. Li *et al.*, “Current investigations into magnetic nanoparticles for biomedical applications,” *J Biomedical Materials Res*, vol. 104, no. 5, pp. 1285–1296, May 2016, doi: 10.1002/jbm.a.35654.

[37] F. Alzoubi *et al.*, “Exploring the impact of pH on the properties of citric acid-coated iron oxide nanoparticles as high-performance T2 contrast agent for MRI applications,” *Results in Engineering*, vol. 18, p. 101206, Jun. 2023, doi: 10.1016/j.rineng.2023.101206.

4. BIOACTIVE GLASSES

The study of bone tissue repair and regeneration has been making considerable progress over the last century. Even though autografts are still considered as the goal standard for the repairing of bone tissue, their limitations in terms of availability, and the disease transmission risk and immune rejection related to allografts and xenografts, have moved on the research to the development of new synthetic materials able to restore the function of the bone [1].

Since the 1950s, the idea of implanting a synthetic material in the body as a substitute for the original tissue has attracted attention, leading to the development of the so called "first generation biomaterials". During this phase, the most important characteristic for a biomaterial was its capacity to be as inert as possible, without causing any reaction in the body [2]. These types of bio-inert materials were mostly corrosion resistant metals and their alloys [2], [3]. However, it is well known that no material can be completely inert when interacts with a living host, therefore many issues emerged, such as tissue breakdown and loosening over time, stress shielding with long term implant failure, wear debris production and osteolysis [2].

Almost twenty years later, the start of the "second generation biomaterials" focused the attention on bioceramic materials as main substitutes for bone tissue, introducing the concept of bioactivity. The implant was not anymore an inert element in the body, but a reactive material able to positively interact with the host and form a strong bond with the bone [2].

The term bioceramics includes ceramics, glass-ceramics and glasses [4]. The latter are of particular importance, as the first discovered bioactive material was a bioactive glass [5]. The ability to enhance revascularization, osteoblast adhesion, enzyme activity and differentiation of osteoprogenitor cells makes bioactive glasses suitable candidates for bone tissue engineering [6]. Over the years, different bioactive glasses have been developed, and their properties are still under investigation nowadays, to improve not only their ability of bone regeneration, but also soft tissue repair and genes activation to stimulate the self-reparation of bone [2], [7].

The next paragraphs will explore the concept of bioactive glasses, starting from their structure and analyzing the bioactivity mechanisms that make bioactive glass such an interesting material.

4.1 Introduction to glasses

Glass is a type of ceramic material which doesn't present an ordered crystalline structure, since its atoms are distributed in a configuration with no long-range order. The structure is therefore called amorphous, and the atomic arrangement is present only at local atomic level [6].

This characteristic confers different properties from crystalline ceramics, even though both glasses and crystals have the same building blocks (cation polyedra) [6], [8]. While crystalline materials present a defined temperature at which they melt or crystallize, glasses possess a time-dependent transformation behavior, in which the transition from solid to liquid, or vice versa, occurs over a range of temperatures without a sharp change in viscosity [6], [9]. In particular, during the cooling of a glass at the liquid state, the material doesn't crystallize, but reaches a phase of metastable equilibrium, becoming a supercooled liquid (Figure 21). With the lowering of the temperature, viscosity increases progressively, preventing the atoms from ordering themselves in a crystalline way. When the temperature goes below the glass transition temperature (Tg), the glass passes from a

supercooled state to a rigid, brittle state called glassy state [10]. Therefore, a solid glass is a material with short elastic deformation range, and the Young's Modulus depends on the thermal history of the glass [10].

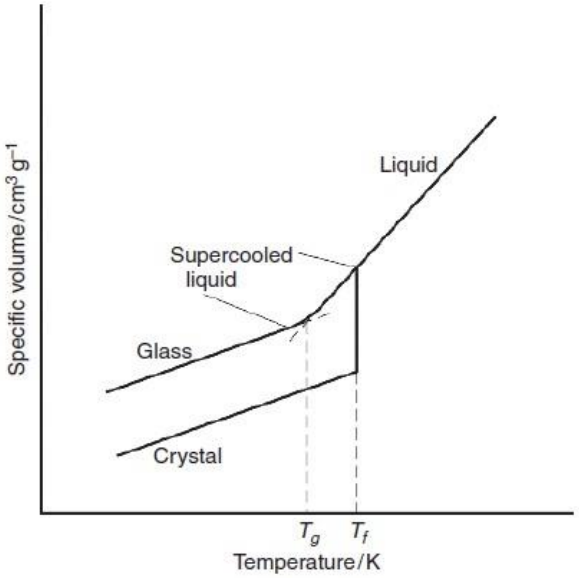

Figure 21. Specific volume of a glassy and a crystal phase as a function of the temperature [10].

Glasses are not stoichiometric compounds made of different mixtures of substances, which can be added in variable quantities allowing the production of a wide range of compositions. In this way, it is possible to tailor different properties to specific applications [9].

As illustrated in Figure 22, the materials forming a glass can be divided into different categories:

- **Glass network formers** form the backbone of the glass. They present a low coordination number (between 3 and 4) and a bond strength in the range of 60-80 kcal/mol. They form defined structures in 2D or 3D without a periodic arrangement and with a broad distribution of bond angles. Within a glass, there can be one or more network formers. Usually, the name of a certain type of glass derives from the network former it contains. Examples of glass formers are SiO_2, B_2O_3, P_2O_5 [6].
- **Glass modifiers** are oxides which modify the glass structure by occupying random positions in the network. The cations distribute within the network and bring additional oxygens, called non-bridging oxygens, which interrupt the continuity of the structure. Glass modifiers present a high coordination number between 6 and 8 and a bond strength in the range of 30-40 kcal/mol. Typical network modifiers, such as Na_2O, K_2O, or CaO, contribute to the reduction of the melting temperature of the glass and are fundamental for the achievement of some properties, such as bioactivity [6], [11].
- **Glass intermediates** are oxides which can behave either as network formers or network modifiers, such as Al_2O_3 and TiO_2. They have an intermediate coordination number between 4 and 8 and a bond strength ranging from 50 to 60 kcal/mol [6].
- **Fining agents**, such as arsenic and antimony, are present for specific reasons in very small quantity which do not affect the properties of the glass. These agents can first release large bubbles which they can then eliminate by absorbing O_2 [6].

- **Colorants** give glasses different colors. They are usually oxides from the 4th or 3rd transition metal series [6].

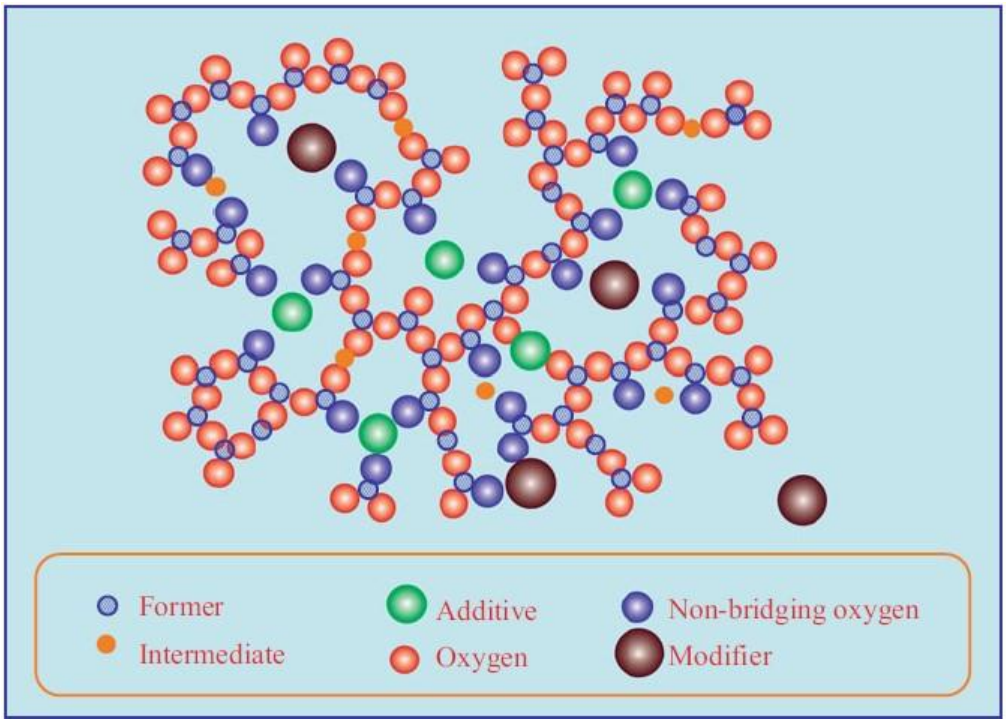

Figure 22. Glass structure [6].

4.2 Fabrication techniques

In order to obtain a glass material, the cooling process should be fast enough to avoid the formation of the crystalline nuclei, because of insufficient time for their organization [6], [10]. Glasses are usually prepared with two main techniques: melt-quenching and sol-gel technique. Glasses obtained with melt-quenching usually possess enhanced mechanical properties, such as hardness and flexural strength, but the procedure requires very high melting temperatures, reaching values up to 1500 °C. With sol-gel technique, it is possible to produce glasses at lower temperatures characterized by an inherent mesoporous structure, with pore diameters ranging from 20 to 50 nm [6].

4.2.1 Melt-quenching technique

This method starts with the mixing of appropriate mole/weight fractions of the glass reagents, such as oxides and carbonates, which should be of high purity (99.9 %) to avoid the presence of contamination of not desired elements [12], [13]. The mixture is pulverized with ball mill in order to have a homogeneous and uniform powder, then placed in a platinum crucible and melted at high temperature values depending on the glass composition [6]. The molten glass should be kept at least 1 hour at the melting temperature to achieve a homogeneous, bubble-free condition [1]. Then, the material is given the desired shape by casting it in graphite molds and annealing is performed at 500 °C, so that the internal stresses generated during the quenching are eliminated [6], [12].

Some types of glass might require higher cooling rates to avoid crystallization. In this case, the molten glass can be quenched in cold water, and the final products, called frits, consist of granules and pieces of different sized which can be easily powdered [12].

Viscosity, thermal expansion and crystallization characteristics are important factors to be considered during melt-quenching of a glass. Viscosity should be low in order to avoid the presence of bubbles and obtain a more homogenous mixture. Moreover, low viscosity facilitates the elimination of the molten glass from the platinum crucible during casting [1].

4.2.2 Sol-gel technique

This technique involves the formation of two phases: sol (or solution) and gel. Sol is a dispersion of colloidal particles in a liquid, while a gel consists of a rigid network containing interconnected pores in sub-micrometer scale and polymeric chains in micrometer scale [6].

The first step of the process involves the mixing of the alkoxide or organometallic precursors, followed by the hydrolysis of the alkoxide precursors with de-ionized water. The hydrolysis of silicon alkoxide produces silanol groups ($Si(OH_4)$), which can interact among each other through polycondensation process forming a silica network (SiO_2). The reactions of hydrolysis and polycondensation are simultaneous processes which lead to the formation of the sol phase [12].

At this point, a gel starts forming by condensation and cross-linking of the silica particles and other colloids. During this process, the viscosity sharply increases until the gel reaches a point (gelation point t_g) in which it behaves like an elastic solid because of the interconnectivity of the particles. The gelation time depends on the concentration of the solvent, nature of the oxide group and amount of water used for the hydrolysis. If heavy alkoxy group are present, or the required amount for hydrolysis is high, the gelation time increases [1], [6].

After gelation, the gel starts a process called aging, or syneresis. Aging lasts several hours at 25-80 °C and causes a decrease in porosity and increase in the strength of the gel, because of the polycondensation and reprecipitation of the gel network. Physical properties such as pore volume, surface area and density are affected by aging, causing a phase transformation and a change in the glass structure [1], [6]. Finally, the gel must be dried by removing the pore liquid from the network. The process of drying can be easily done for colloidal gels (pore size >100 nm), while for alkoxide gels with a pore size between 1 and 10 nm large capillary stresses may develop. Drying above the pore-liquid-solid point (hypercritical drying) can eliminate drying stresses since it avoids the solid-liquid interface [1].

Sintering of the gels is important to control the stability of the material. Moreover, sintering increases strength, hardness and density. The sintering temperature for alkoxide-based gels varies between 900 °C and 1150 °C, according to the glass composition.

Sol-gel glasses possess some beneficial characteristics in the context of bioactive glasses, compared to the melt-quenched ones. For instance, sol-gel glasses have a higher surface area, which results in a higher dissolution rate and cellular response. Moreover, the hierarchical structure made of macropores and nanopores resembles the one of natural tissues, leading to a better interaction with cells. On the other hand, sol-gel glass are not considered strong enough for hard tissue engineering applications, such as bone tissue engineering, therefore melt-quenched glasses are preferred [1].

4.3 Bioactivity

The concept of bioactivity was introduced for the first time by Larry H. Hench in 1969, who proposed the following definition: "*A bioactive material is one that elicits a specific biological response at the*

interface of the material which results in the formation of a bond between the tissues and the material" [5]. When speaking about bioactive materials, two main steps occur after their implantation in the body: the first step implicates time-dependent specific reactions at the material's surface when in contact with body fluids, while the second step involves the formation of a biologically active hydroxyapatite (HA) layer, which is responsible for the bonding with hard and soft tissues [5], [6].

Indeed, the HA layer formed on the surface of bioactive materials is equivalent in chemistry and structure to the actual mineral phase in the bone [5]. This comparability is responsible for the interfacial bonding, since the HA layer interacts with collagen fibrils of damaged bone and creates an adherent interface which is able to withstand considerable mechanical forces [4], [5]. Further studies are needed, but the bonding between bone and HA layer is supposed to involve protein adsorption, attachment of bone progenitor cells, cell differentiation and production of bone extracellular matrix followed by its mineralization [4].

The level of bioactivity of a material is strictly correlated to the speed of formation of a bond at the interface between the implant and the tissue [3]. It is measured by the bioactivity index I_B, which is calculated as shown in Equation 3:

$$I_B = 100/t_{0.5bb}$$

Equation 3. Bioactivity index [3].

Where $t_{0.5bb}$ is the time it takes for more than a half of the interface to bond [3].

If a material has a bioactivity index greater than 8, it can bond to both hard and soft tissue, while if I_B is between 0 and 8 the material can only bond to hard tissue [3].

This distinction can be organized into two categories of bioactive materials: Class A and Class B. The rate of tissue response to the implant, and so the kinetics of surface reactions and ion dissolution determine the type of class [14].

Class A materials, that have $I_B > 8$, such as bioactive glass 45S5, exhibit rapid bone bonding and long-term implant durability, since the bonding to both soft and hard tissue prevents any micromotion of the implant [14]. These materials possess the properties of both osteoconduction and osteoinduction. Osteoconduction refers to the ability of a material to provide a biocompatible surface for bone migration, while osteoinduction concerns the induction of bone growth from undifferentiated stem cells which are stimulated to differentiate into pre-osteoblasts, and so to produce new bone even in areas where bone doesn't normally exist [4], [14], [15]. Indeed, the reactions at the surface of the material involve the dissolution of Si and Ca in critical concentration which leads to intracellular and extracellular responses. These responses are translated into the formation of osteoid bridges between particles, with subsequent mineralization and production of mature bone [2].

Class B materials, e.g. synthetic HA, have $0 < I_B > 8$ and are characterized by the presence of only osteoconduction. These materials show slow bonding to the bone, with no formation of a bond with soft tissues and slow or incomplete bone cells proliferation [14].

While for Class A materials the formation of crystallized HA requires 2-6 hours, Class B materials take up to 30 days for nucleation and crystallization of HA [14].

4.4 Discovery of bioactive glasses

The history of bioactive materials starts with the first bioactive glass, discovered in 1969 by Larry H. Hench. He developed a type of soda-lime-phosphate-silicate glass that possessed excellent biocompatibility and the ability to form a bond with the bone so strong that it was impossible to remove the implant from the site in rats without breaking the bone [2], [4]. This new type of glass composition, named 45S5 and Bioglass®, contained in weight percent 45% SiO_2 as network former, 24.5% Na_2O and 24.5% CaO as network modifiers and the addition of 6% P_2O_5. Moreover, 45S5 Bioglass® proved to be able to promote stem cell differentiation into osteoblasts, supporting the production of a bone mineralized matrix. In 1985, 45S5 was used in its first clinical application in the ossicular chain of the middle ear of a patient [7].

This discovery signed a turning point in the concept of biomaterial implantation, moving the research from materials as biologically inert as possible (first generation materials) to reactive implants able to promote natural tissue regeneration (second generation materials) [2].

The composition of bioactive glass 45S5 defines its position in the zone of both bone and soft tissue bonding, as shown in the phase diagram proposed by Hench in Figure 23 [6].

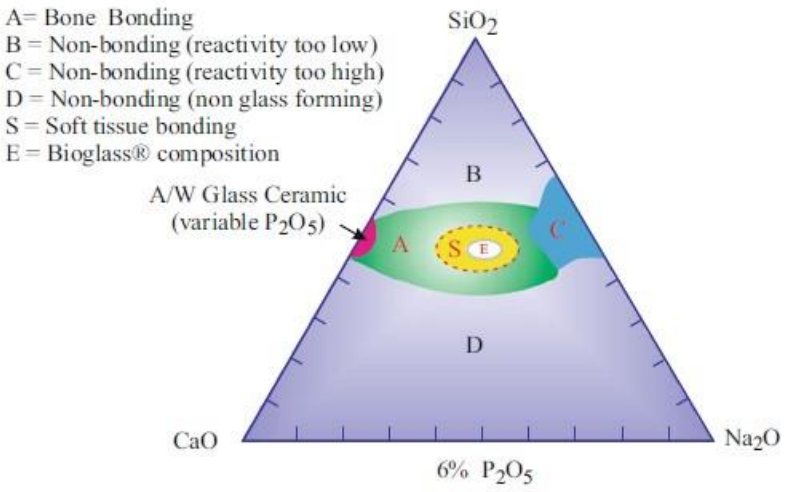

Figure 23. Phase diagram indicating glass forming region and the type of bonding to tissue of bioactive glasses proposed by Hench [6].

By tailoring the composition of the glass and its processing methods, it is possible to obtain major changes in the properties and in the results after implantation, tuning in this way the mechanical properties and dissolution rates. Indeed, one of the most important requirements regarding any biomaterial is the ability to be resorbed over a period of time after implantation and replaced by the natural host tissue. In particular, the resorption rate of the biomaterial should match the growth rate of the surrounding tissue, in order to obtain an appropriate tissue regeneration [6].

The amorphous structure in bioactive glasses is another important characteristic regarding their bioactivity. Crystals can form inside of an amorphous glass when the material is exposed to heat treatment at a fixed temperature and duration, which can lead to crystal nucleation and growth. This phenomenon, known as devitrification, leads to the formation of a glass-ceramic material. Glass-ceramics possess a structure composed of crystalline phases surrounded by an amorphous glassy

matrix. Even though in general glass ceramics possess enhanced mechanical properties compared to their parent glasses, different studies highlighted how bioactivity is reduced because of the presence of crystalline phases. Crystallization of a bioactive glass should be, therefore, avoided [6].

Briefly, some of the main important requirements for bioactive glasses to be implanted include:

- Formation of a hydroxyapatite layer on the glass surface when the material is in contact with SBF [6].
- Adequate mechanical properties to prevent the failure of the glass structure under loading. In particular, when bioactive glasses are prepared as scaffolds, they should possess mechanical properties comparable to the ones of the host tissue [6].
- Biocompatibility, meaning non-toxicity and promotion of cell adhesion and proliferation [6].
- Absence of any inflammatory response, immunogenicity and cytotoxicity [6].
- Dissolution into non-toxic products, which can be resorbed or excreted by the body [6].
- Sterile surface and bulk material of the implant [6].

4.5 Bioactivity reaction stages

The answer to the bone bonding properties of bioactive glasses relies on their chemical reactivity when in contact with body fluids [11]. The first stage of bioactivity involves the formation of HA layer of the surface on the implant, and it can happen both in body fluids in vivo and in vitro aqueous solutions, such as Simulated Body Fluid (SBF) [4], [11].

During this process, five different steps have been identified by Hench et al. [5]:

1. During the first step, a rapid exchange of Na^+ and/or Ca^{2+} cations with H^+ or H_3O^+ from the solution happens. This replacement gives rise to the formation of silanol bonds (Si-OH), as described in Equation *4*. Since they are not part of the glass network, glass modifiers leach very easily from the surface of the glass to the aqueous solution. As a result of the ion exchange, the basicity of the solution increases (pH > 7) [4], [5], [11]. If present in the initial composition of the glass, $(PO_4)^{3-}$ ions are released to the solution [7].

$$\mathrm{Si-O^-Na^+ + H^+ + OH^- \rightarrow Si- OH^+ + Na^+(aq) + OH^-}$$

Equation 4. Cation exchange of Na^+ with H^+ [4].

   This reaction lasts a few minutes and leaves the surface layer alkaline cation depleted, with a net superficial negative charge [7].
2. Since the local pH is high, hydroxyl ions (OH^-) are in high concentration and can attack the silica glass network by breaking Si – O – Si bonds. As shown in Equation 5, more silanols are forming at the glass-solution interface, while the soluble silica goes to the solution in the form of $Si(OH)_4$ groups [4], [5]. The soluble silica has been proven to have a strong impact on the proliferation of cells forming new bone next to the glass surface [7]. The rate of silica dissolution is strongly dependent on the glass composition. If the percentage of SiO_2 overcomes 60%, the number of bridging oxygens is higher, so the rate of silica dissolution decreases [11].

$$\mathrm{Si-O-Si + H_2O + OH^- \rightarrow Si- OH + OH-Si}$$

Equation 5. Attack of the silica glass network and formation of silanols [4].

3. At this point, neighboring silanols start a polycondensation and repolymerization process which ends in the formation of a silica-rich layer on the surface of the glass [4], [5]. This layer has a thickness between 1 and 2 μm and it is microscopely highly porous, with an average pore diameter between 30 and 50 Å [7], [16]. The process of repolymerization can be confirmed with nuclear magnetic resonance (NMR) by the increase of the number of bridging oxygens during leaching [4].
4. During the fourth step, Ca^{2+} and PO_4^{3-} groups released from the glass migrate through the silica-rich layer, together with those coming from the solution, to form an amorphous calcium-phosphate film on the top of the silica-rich layer. This $CaO\text{-}P_2O_5$ film starts growing into a thicker layer with the incorporation of calcium and phosphate ions from the solution. The Si-OH groups still present on the silica-rich layer have been identified as sites of nucleation for the calcium phosphate [4], [5], [11]. X-ray diffraction (XRD) can confirm the presence of an amorphous calcium-phosphate layer prior to the formation of HA [4].
5. The final step involves the incorporation of hydroxyls (OH^-) and carbonate (CO_3^{2-}) ions from the solution to the amorphous calcium-phosphate layer and its crystallization into HA. This final layer is similar to the nano-crystalline mineral phase of the physiological bone tissue in both composition and structure, and it is crucial for the direct bonding between implant and living tissue [4], [5], [7]. The HA layer can increase its thickness with time up to 100 μm [7].

If the implant is studied in vivo, after HA formation additional steps take place for the complete bonding and integration of the implant with bone. These biological phases were first explained by Hench and Andersson [17], but the exact mechanisms are still under investigation [4], [11]. Anyway, it is known that proteins adsorb to the HA layer, cells attach, differentiate and produce bone matrix [4].

The five additional steps are explained as follows:

6. Growth factors and proteins are adsorbed by the reaction layers already during the first four stages of bioactivity, determining, in this way, the characteristics of the HA layer [2], [7].
7. The time required for the macrophages to prepare the implant site for tissue repair is reduced by the action of the reactive layers [2].
8. Stem cells attach and colonize the surface of the implant. The colonization takes 12 hours from the implantation of the material [7].
9. During this stage, stem cells proliferate and differentiate into mature osteoblasts [2].
10. Mature osteoblasts produce growth factors which stimulate cellular attachment, mitosis and production of extracellular matrix proteins [7].
11. After its deposition, the extracellular matrix is mineralized is 6-12 days. As a result, mature osteocytes are embedded in a mature collagen-HA matrix [2], [7].

The division and proliferation of osteoprogenitor cells is strongly related to the ion release into the solution. If too many ions are released, the implant might show some toxic effects. Some studies observed that the gene expression of mature human osteoblasts is highly dose-dependent, reaching a maximum at 20 μg/ml of soluble silica and 60-90 μg/ml of calcium ions. The concentration of these two ionic products at the cell-solution interface is, therefore, fundamental for controlling the cell cycle and activating the genes responsible for the osteogenesis process [2], [7].

4.6 Categories of bioactive glasses

Bioactive glasses can be grouped into different families, whose name is related to the main component of the glassy network. Within each family, different compositions have been developed with different results in properties e behavior [10]. In the following paragraphs, the main bioactive glass families are briefly described.

4.6.1 Silicate glasses

Silicate glasses are characterized by a 3D network of SiO_4 tetrahedra connected to each other by oxygen centers, called bridging oxygens (BO). The difference from a crystalline quartz stays in the variability of the Si-O bond length and angle, which can vary between 120° and 180°, causing a high degree of disorder in the structure. When network modifiers, such as Na_2O or CaO, are added to the composition of a silicate glass, the cations usually occupy interstices, and the oxygens associated with them replace some of the bridging oxygens in the structure. These new oxygens cause an opening in the network because they do not participate in the bonding between the building blocks, therefore they are called non-bridging oxygens (NBO) [6], [11].

In silicate bioactive glasses Si_2O, Na_2O, CaO and P_2O_5 are essential components for the presence of bioactivity and the number of non-bridging oxygens in each tetrahedron is more than 2.6 [6], [11].

The three key compositional features that distinguish silicate bioactive glasses from traditional Na_2O-CaO- Si_2O glasses are the following:

- Si_2O content must be less than 60 mol% [5].
- The content of Na_2O and CaO must be high [5].
- The CaO/P_2O_5 ratio must be high [5].

The presence of these elements results in a reduced reticulation of the network which makes the surface highly reactive in physiological fluids [5]. Indeed, with higher content of SiO_2 (more than 60 mol%) the dissolution rate of the glass ions from the surface decreases, and so the bioactivity. High CaO/P_2O_5 content facilitates the release of ions from the surface when the material is immersed in body fluid and supports cells proliferation at the interface [11]. Moreover, studies on in vitro cell culture proved that silicate bioactive glasses support proliferation of function of osteoblastic cells [6].

45S5 Bioglass® is the oldest and one of the most studied silicate glasses. In the last two decades, many different substitutions in the composition have been investigated. Table 1 shows the main silicate glasses and their compositions.

Table 1. Silicate glasses compositions [7], [18].

Composition (wt%)	**45S5**	**S53P4**	**1393**
SiO_2	45.0	53.0	53.0
Na_2O	24.5	23.0	6.0
CaO	24.5	20.0	20.0
P_2O_5	6.0	4.0	4.0
MgO	0.0	0.0	5.0
CaF_2	0.0	0.0	0.0

4.6.2 Borate glasses

The network former in pure borate glasses is B_2O_3, which creates a structure of linked triangles forming planar rings (boroxyl group), with variable B-O-B angles [6]. The addition of network modifiers causes a change of boron coordination number, converting the structure from triangular to tetrahedral, without the formation of NBO and increasing the T_g. However, when the amount of network modifiers exceeds a critical concentration, NBO are forming, leading to an inversion of the properties: the glass becomes weaker and T_g decreases. This phenomenon is known as boron anomaly, and it is explained by the possible variation of boron coordination number between 3 and 4 [6], [19].

Borate glasses can be bioactive, showing some differences from the silicate ones: due to their atomic structure, borate glasses exhibit higher reactivity and lower chemical stability, therefore they convert more completely and rapidly into HA when immersed in aqueous phosphate solutions. The mechanism of conversion is quite similar to silicate glasses but, instead of the formation of a SiO_2-rich layer, a temporary borate-rich layer appears. Moreover, the sintering of borate glasses results more controlled than silicate glasses [6], [11].

Borate bioactive glasses have demonstrated to support cell proliferation and differentiation in vitro and tissue infiltration in vivo. Nevertheless, one of the main concerns regarding this type of glasses is their cytotoxicity in static conditions during in vitro cell culture, most likely related to the release of $(BO_3)^{3-}$ ions associated with toxicity and elevated pH because of the fast dissolution rate. On the other hand, under dynamic culture conditions no considerable toxicity was detected [6], [11], [20].

4.6.3 Borosilicate glasses

Recent studies are focusing on the partial replacement of SiO_2 in silicate glasses with B_2O_3, in order to control the degradation rate and tailor the properties of the materials. This type of glass, in which the network formers of SiO_2 are partially replaced by B_2O_3, is called borosilicate glass [11].

Borosilicate glasses can merge the beneficial aspects of silicate and borate glasses in different ways:

- Since some silicate glasses, such as 1393 BAG, dissolve slowly, the partial replacement of SiO_2 with B_2O_3 increases the degradation rate of the glass, expanding the possible clinical applications and leading to boron release in similar amount which was found to be beneficial in cell culture testing [20].
- One of the main problems of silicate glasses is their tendency to crystallize when sintered as scaffolds. As mentioned previously, crystallization of bioactive glasses decreases bioactivity and doesn't allow a proper sintering of the material. The presence of B_2O_3 can drastically reduce this tendency to crystallization, allowing the manufacturing of bioactive glass scaffolds for bone tissue engineering [20].
- The presence of boron enhances osteogenic and angiogenic properties, as proven in previous studies [20].

One of the main concerns about borosilicate glasses is still related to their potential cytotoxicity, as discussed for borate glasses [6], [20]. Consequently, boron concentration must be controlled and regulated.

Different types of borosilicate glasses have been developed starting from silicate glasses. One big family includes the borosilicate glasses deriving from glass 1393, where the name changes according to the boron content. 1393 B1, for example, shows an increased boron amount compared to the original 1393, while 1393 B3 refers to a full borate glass, without any SiO_2 in its composition. The glass 1393 B20 indicates that 20% of SiO_2 is replaced by B_2O_3. Table *2* shows the nominal composition of the silicate glass 1393 and its borate and borosilicate modifications.

Table 2. Compositions of glass 1393 and its modifications [20], [21], [22].

Composition (mol%)	**1393**	**1393 B1**	**1393 B20**	**1393 B3**
SiO_2	54.6	34.4	43.7	0.0
B_2O_3	0.0	20.0	10.9	56.6
Na_2O	6.0	5.8	6.0	5.5
CaO	22.1	19.5	22.1	18.5
P_2O_5	1.7	3.9	1.7	3.7
MgO	7.7	4.9	7.7	4.6
K2O	7.9	11.6	7.9	11.1

4.6.4 Phosphate glasses

Phosphate glasses are composed of P_2O_5 as a network former, which is organized in PO_4 tetrahedral structural units. The highly asymmetric network arrangement and the facilitated hydration of the P-O-P bonds are responsible for the low durability of these glasses in aqueous solutions [6]. Indeed, their ability to degrade in a congruent manner provides a more complete dissolution compared to the silica-based glasses [23].

Phosphate glasses have attracted great attention as bioactive materials because of different aspects. Specifically, the solubility of phosphate glasses can be controlled by their composition through the addition of metal oxides, such as TiO_2, CuO, NiO or MnO, making them ideal materials for temporary implants [6], [24]. The possibility of shaping phosphate glasses into glass fibers makes them suitable as guides for muscle or nerve repair in the soft tissue engineering field, while for hard tissue engineering the material can be used as bulk or powder in conjunction with polymers [6]. Moreover, the constituent ions of the network are present in the organic mineral phase of the bone, creating a chemical affinity between the glass and the tissue [11].

Despite all these advantages, the method of dissolution of phosphate glasses makes the initial cell adhesion quite poor. Some studies observed that this problem can be overcome with simple surface treatments, such as base-washing or silanization, through which it is possible to promote cell adhesion and spread to comparable levels of material commonly used in cell culture [23].

4.6.5 Doped glasses

Glass composition can be modified with the addition of dopants to improve some of its properties. A dopant refers to the intentional addition of an element in low concentration (from a few ppm to a few percent), compared to the main elements present in the glass composition, with the aim of enhancing or introducing some characteristics in the material [25].

Different types of dopant elements have been found beneficial for bioactive glass function and structure. Alumina (Al_2O_3) can be helpful for dental applications and bone implants, since it has high

bioinertness and can increase the mechanical properties with its high abrasion resistance and high hardness [6].

The addition of silver, copper or zinc have beneficial effects on the antibacterial properties, while maintaining the bioactive function [6].

Zinc and magnesium show a positive effect on the stimulation of osteoblast proliferation, differentiation and bone mineralization. Moreover, partial substitution of MgO for CaO in S53P4 has demonstrated to increase the temperature window for hot working of the glass melt, reducing the crystallization tendencies during sintering [26]. As reported in Table *2*, the glass composition of 1393 and its modifications are doped with MgO [6].

Strontium effects are known for accelerated bone-healing, stimulation of osteogenesis through a positive action on osteoblasts and reduced bone resorption through a negative action on osteoclasts [6], [25]. Specifically for borosilicate glasses, strontium and magnesium introduced in place of calcium have demonstrated to contribute to the stabilization of the borate network, leading to a more controlled boron release. This stabilizing effect is considered beneficial for cell proliferation, since an immediate and elevated release of boron inhibits the amplification of cells [27].

4.7 Clinical applications of BAGs

The versatility of processing bioactive glasses into different shapes, combined with the possibility of tailoring their properties in numerous ways, makes this type of biomaterial suitable for different clinical applications. Considering their ability of promoting osteogenesis [28], bioactive glasses are mainly employed in the bone repair field, as monolithic implants or particulates. Nevertheless, they can also have beneficial functions in the role of coatings of metallic prosthesis and in the treatment of oral hypersensitivity. Recent studies have investigated the possibility of using bioactive glasses as drug carriers and in soft tissue repair, broadening the possible clinical applications of this material.

4.7.1 Bone repair and orthopedic implants

Healing of bone defects is currently one of the most important applications for bioactive glasses. Bone defects can emerge for different reasons including trauma, congenital defects, disease or tumor removal [4].

In 1984, Bioglass® 45S5 underwent its first clinical application. It consisted of a cone shaped material implanted in deaf patients affected by an infection responsible for the degradation of two of three bones in the middle ear (middle ear prosthesis, MEP®). The implant successfully restored the transmission of sound from the eardrum to the cochlea, giving the ability of hearing back to the patients. From then on, bioactive glasses started to be used as substitutes of bone in other regions of the body, such as tooth extraction sites (endosseous ridge maintenance implant, ERMI®) and orbital floors. However, the commercial success of these products is not very significant, since the commercial viability of custom design is not possible. Bioactive glasses in the form of particulates are, therefore, preferred rather than monolithic shapes [4].

The use of glass particles or granules is considered quite convenient by orthopedic surgeons and dentists, since the material can be pressed in the implant site quite easily. In 1993, 45S5 was employed as the first particulate bioactive glass, called PerioGlas®, to repair defects in the jaw related to periodontal disease. PerioGlas®, still sold nowadays, proved its efficacy with in vivo and

clinical studies. It has a particle size between 90 and 710 µm and it is used for the regeneration of the bone around the root of a healthy tooth, or to improve the quality of bone in the jaw before anchoring titanium implants [4].

Particulates can be also employed for orthopedic bone grafting of non-load-bearing sites, as demonstrated by NovaBone®, used for the first time in 1999. The particulate is usually mixed with blood taken from the defect site and manipulated to create a putty-like consistency which is then pressed into the gap. Apart from 45S5, other glass compositions have been introduced for bone graft substitutes, such as particulates of S53P4, known as BonAlive® and approved by EMA in 2006 for assisting the implantation of titanium roots in the porous maxilla [4].

4.7.2 Treatment of oral hypersensitivity

When the dentine of teeth becomes exposed in the gum line, tooth hypersensitivity arises. Hypersensitivity causes pain whenever there is fluid flow change through the tubules of the dentine, since they are linked to the pulp chamber, and so to nerve endings. NovaMin® is a very fine particulate of Bioglass® 45S5 in the size of 18 µm, used in the form of a toothpaste for treating hypersensitivity. In vitro studies proved that the glass particles adhere to the dentine and deposit a HA layer which locks the tubules, relieving the patient from pain. In this way, the particles can stimulate long-term repair and mineralization of the bone. Moreover, bioactive glass particles can be used as a repair treatment of the enamel in the phases before tooth-bleaching, and in the air polishing for teeth whitening treatments [3], [4].

4.7.3 Coating of metallic implants

The importance of bioactive coatings on metallic implants, such as hip prosthesis, is fundamental, since metals are bioinert and cause the formation of a fibrous capsule, with consequent loosening and implant failure. Bioactive glasses are considered promising materials, since they can establish a bonding between implant and host tissue and their interconnected porosity supports tissue ingrowth, enhancing the stability of the prosthesis [3], [4]. Some studies on Ti-based implants covered by bioactive glass showed promising results, with the formation of a thick interfacial layer on the implant surface [29] and better osteointegration in vivo [30]. However, some limitations are encouraging researchers to find more suitable new glass compositions, because the biodegradable nature of the glass might cause long-term instability. Moreover, it is important that the thermal expansion coefficient of glass and metal should match, to avoid a detaching of the glass from the implant during processing [4].

4.7.4 Drug delivery

Controlled drug delivery refers to a planned delivery of a drug in advance, with the intention of maximizing its usage with minimal administration and making it more effective without the possibility of reducing or increasing the dose. Some studies proved that bioactive glasses can be employed as successful drug carriers. For example, bioactive glass combined with teicoplanin was tested to treat osteomyelitis in the tibial bone of rabbits in vivo. The study showed promising results, demonstrating that during the release of the drug, there was a formation of a bioactive HA layer. This strategy allowed the treatment of the disease with concurrent bone regeneration. Similarly, vancomycin was successfully incorporated on a bioactive glass carrier to treat osteomyelitis [3].

4.7.5 Soft tissue repair

In the last twenty years, researchers have demonstrated the possibility of using bioactive glasses for the repair or regeneration of soft tissues. In particular, recent studies have focused on the ability of BAGs of promoting angiogenesis as an alternative to the delivery of expensive growth factors stimulating neovascularization, such as vascular endothelial growth factor (VEGF) [28]. Silicate bioactive glass 45S5 particles used in low concentration (0.01-0.02 wt.%) as a coating of polystyrene surfaces have proved to enhance the proliferation of fibroblast 208F cells cultured in vitro for 24 hours, when compared to the uncoated surfaces. Moreover, improved neovascularization was confirmed by in vivo studies using a polyglycolic acid mesh covered by 45S5 glass implanted in rats for 28 and 42 days [31].

Angiogenesis promotion is not only peculiar to 45S5, but it has been proven that even borate 1393 B3 scaffolds possess this ability [32]. Furthermore, 1393 B3 scaffolds doped with different amounts of Cu were studied to investigate the role of the glass as a source of Cu, whose ions (Cu^{2+}) are known for having a stimulative action on the proliferation of endothelial cells. In comparison to not Cu-doped scaffolds, a significant increase in blood vessels was observed [32].

Besides angiogenesis, other studies focused on the promotion of neocartilage formation in vitro with the help of the ionic degradation products from bioactive glasses. In particular, researchers suppose that the ions released by porous scaffolds made of glass 1393, cultured together with bovine chondrocytes, can play the role of supplements in the medium, modulating chondrocyte biosynthesis, and so promoting neocartilage formation [33]. These results show promising applications for bioactive glasses in chondrogenesis, considering the difficulties and limitations of cartilage regeneration [28].

REFERENCES

[1] S. K. Nandi, A. Mahato, B. Kundu, and P. Mukherjee, “Doped Bioactive Glass Materials in Bone Regeneration,” in *Advanced Techniques in Bone Regeneration*, A. R. Zorzi and J. B. De Miranda, Eds., InTech, 2016. doi: 10.5772/63266.

[2] L. L. Hench, “Chronology of Bioactive Glass Development and Clinical Applications,” *NJGC*, vol. 03, no. 02, pp. 67–73, 2013, doi: 10.4236/njgc.2013.32011.

[3] V. Krishnan and T. Lakshmi, “Bioglass: A novel biocompatible innovation,” *J Adv Pharm Technol Res*, vol. 4, no. 2, p. 78, 2013, doi: 10.4103/2231-4040.111523.

[4] J. R. Jones, “Review of bioactive glass: From Hench to hybrids,” *Acta Biomaterialia*, vol. 9, no. 1, pp. 4457–4486, Jan. 2013, doi: 10.1016/j.actbio.2012.08.023.

[5] L. L. Hench, “Bioceramics: From Concept to Clinic,” *Journal of the American Ceramic Society*, vol. 74, no. 7, pp. 1487–1510, Jul. 1991, doi: 10.1111/j.1151-2916.1991.tb07132.x.

[6] G. Kaur, *Bioactive Glasses: Potential Biomaterials for Future Therapy*. in Series in BioEngineering. Cham: Springer International Publishing, 2017. doi: 10.1007/978-3-319-45716-1.

[7] E. Fiume, J. Barberi, E. Verné, and F. Baino, “Bioactive Glasses: From Parent 45S5 Composition to Scaffold-Assisted Tissue-Healing Therapies,” *JFB*, vol. 9, no. 1, p. 24, Mar. 2018, doi: 10.3390/jfb9010024.

[8] UNSW Sidney, “Glass,” Materials science and Engineering. Accessed: Jan. 29, 2025. [Online]. Available: https://www.unsw.edu.au/science/our-schools/materials/engage-with-us/high-school-students-and-teachers/online-tutorials/ceramics/glass

[9] Taha Khan, “Glass: An Overview,” AZO materials. Accessed: Jan. 29, 2025. [Online]. Available: https://www.azom.com/article.aspx?ArticleID=1021

[10] J. Fernández–Navarro and M. Villegas, “What is Glass?: An Introduction to the Physics and Chemistry of Silicate Glasses,” in *Modern Methods for Analysing Archaeological and Historical Glass*, 1st ed., K. Janssens, Ed., Wiley, 2013, pp. 1–22. doi: 10.1002/9781118314234.ch1.

[11] B. Karasu, A. O. Yanar, A. Koçak, and Ö. Kisacik, “Biyoaktif Camlar,” *El-Cezeri Fen ve Mühendislik Dergisi*, vol. 4, no. 3, pp. 436–471, Sep. 2017, doi: 10.31202/ecjse.323652.

[12] G. Kaur, G. Pickrell, N. Sriranganathan, V. Kumar, and D. Homa, “Review and the state of the art: Sol–gel and melt quenched bioactive glasses for tissue engineering,” *J Biomed Mater Res*, vol. 104, no. 6, pp. 1248–1275, Aug. 2016, doi: 10.1002/jbm.b.33443.

[13] H. Ylänen, Ed., *Bioactive glasses: materials, properties and applications*, Second edition. in Woodhead publishing series in biomaterials. Duxford Cambridge, Mass. Kidlington: Woodhead Publishing, an imprint of Elsevier, 2018.

[14] L. L. Hench, D. L. Wheeler, and D. C. Greenspan, “Molecular Control of Bioactivity in Sol-Gel Glasses,” *Journal of Sol-Gel Science and Technology*, vol. 13, no. 1/3, pp. 245–250, 1998, doi: 10.1023/A:1008643303888.

[15] A. T. and J. C., “Osteoinduction, osteoconduction and osseointegration,” *European Spine Journal*, vol. 10, no. 0, pp. S96–S101, Oct. 2001, doi: 10.1007/s005860100282.

[16] Greenspan, David C, “Bioactive glass: mechanisms of bone bonding,” 1999, Accessed: Feb. 08, 2025. [Online]. Available: https://www.tandlakartidningen.se/media/927/Greenspan_8_1999.pdf

[17] Hench, L. L., Andersson, O., “Bioactive Glass Coatings,” in Advanced Series in Ceramics. , 1993, pp. 239–60.

[18] Sandeep Kumar Yadav, Vikash Kumar Vyas, Sarthak Ray, Md Ershad, Akher Ali, Sunil Prasad, Manas Ranjan Majhi and and Ram Pyare, “In vitro bioactivity and mechanical properties of zirconium dioxide doped 1393 bioactive glass,” *International Journal of Scientific & Engineering Research, Volume 8, Issue 3, March-2017*.

[19] A. Wright, G. Dalba, F. Rocca, and N. Vedishcheva, “Borate Versus Silicate Glasses: Why Are They So Different?,” *Physics and Chemistry of Glasses - European Journal of Glass Science and Technology Part B*, vol. 51, pp. 233–265, Oct. 2010.

[20] A. Szczodra *et al.*, “Boron substitution in silicate bioactive glass scaffolds to enhance bone differentiation and regeneration,” *Acta Biomaterialia*, vol. 186, pp. 489–506, Sep. 2024, doi: 10.1016/j.actbio.2024.07.053.

[21] A. Ali *et al.*, “CuO assisted borate 1393B3 glass scaffold with enhanced mechanical performance and cytocompatibility: An In vitro study,” *Journal of the Mechanical Behavior of Biomedical Materials*, vol. 114, p. 104231, Feb. 2021, doi: 10.1016/j.jmbbm.2020.104231.

[22] L. Bi *et al.*, “Evaluation of bone regeneration, angiogenesis, and hydroxyapatite conversion in critical-sized rat calvarial defects implanted with bioactive glass scaffolds,” *J Biomedical Materials Res*, vol. 100A, no. 12, pp. 3267–3275, Dec. 2012, doi: 10.1002/jbm.a.34272.

[23] L. Azizi, P. Turkki, N. Huynh, J. M. Massera, and V. P. Hytönen, “Surface Modification of Bioactive Glass Promotes Cell Attachment and Spreading,” *ACS Omega*, vol. 6, no. 35, pp. 22635–22642, Sep. 2021, doi: 10.1021/acsomega.1c02669.

[24] F. Baino *et al.*, “Processing methods for making porous bioactive glass-based scaffolds—A state-of-the-art review,” *Int J Applied Ceramic Tech*, vol. 16, no. 5, pp. 1762–1796, Sep. 2019, doi: 10.1111/ijac.13195.

[25] J.-M. Nedelec *et al.*, “Materials doping through sol–gel chemistry: a little something can make a big difference,” *J Sol-Gel Sci Technol*, vol. 46, no. 3, pp. 259–271, Jun. 2008, doi: 10.1007/s10971-007-1665-0.

[26] J. Massera, L. Hupa, and M. Hupa, “Influence of the partial substitution of CaO with MgO on the thermal properties and in vitro reactivity of the bioactive glass S53P4,” *Journal of Non-Crystalline Solids*, vol. 358, no. 18–19, pp. 2701–2707, Sep. 2012, doi: 10.1016/j.jnoncrysol.2012.06.032.

[27] J. M. Tainio *et al.*, “Structure and in vitro dissolution of Mg and Sr containing borosilicate bioactive glasses for bone tissue engineering,” *Journal of Non-Crystalline Solids*, vol. 533, p. 119893, Apr. 2020, doi: 10.1016/j.jnoncrysol.2020.119893.

[28] M. N. Rahaman *et al.*, “Bioactive glass in tissue engineering1,” *Acta Biomaterialia*, vol. 7, no. 6, pp. 2355–2373, Jun. 2011, doi: 10.1016/j.actbio.2011.03.016.

[29] S. Lopez-Esteban, E. Saiz, S. Fujino, T. Oku, K. Suganuma, and A. P. Tomsia, “Bioactive glass coatings for orthopedic metallic implants,” *Journal of the European Ceramic Society*, vol. 23, no. 15, pp. 2921–2930, 2003, doi: 10.1016/S0955-2219(03)00303-0.

[30] N. Drnovšek, S. Novak, U. Dragin, M. Čeh, M. Gorenšek, and M. Gradišar, “Bioactive glass enhances bone ingrowth into the porous titanium coating on orthopaedic implants,” *International Orthopaedics (SICOT)*, vol. 36, no. 8, pp. 1739–1745, Aug. 2012, doi: 10.1007/s00264-012-1520-y.

[31] R. M. Day *et al.*, “Assessment of polyglycolic acid mesh and bioactive glass for soft-tissue engineering scaffolds,” *Biomaterials*, vol. 25, no. 27, pp. 5857–5866, Dec. 2004, doi: 10.1016/j.biomaterials.2004.01.043.

[32] J. R. Jones and A. G. Clare, Eds., *Bio-Glasses: An Introduction*, 1st ed. Wiley, 2012. doi: 10.1002/9781118346457.

[33] P. Jayabalan, A. R. Tan, M. N. Rahaman, S. B. Bal, C. T. Hung, and J. L. Cook, “Bioactive Glass 13-93 as a Subchondral Substrate for Tissue-engineered Osteochondral Constructs: A Pilot Study,” *Clinical Orthopaedics & Related Research*, vol. 469, no. 10, pp. 2754–2763, Oct. 2011, doi: 10.1007/s11999-011-1818-x.

5. BAGs SCAFFOLDS IN BONE TISSUE ENGINEERING

5.1 Tissue engineering

Tissue engineering (TE) is an interdisciplinary field which emerged in the last decades as a promising method to repair and regenerate tissues, or organs, damaged because of trauma, injury, disease, or aging [1], [2]. A very important advantage of this approach is the possibility to avoid organ and tissue transplantations, which are often responsible for the transmission of disease and rejections, together with the problem of lack of availability from donors and long waiting lists [3].

TE aims at developing tissue substitutes which can simulate native extracellular matrix (ECM) and promote the growth of functional tissue, both in vivo and in vitro. The general objective is to provide a temporary structure for letting tissue forming cells produce new tissue [3].

Figure 24 shows the most important features inside of a tissue engineering approach which are described below in a more detailed way.

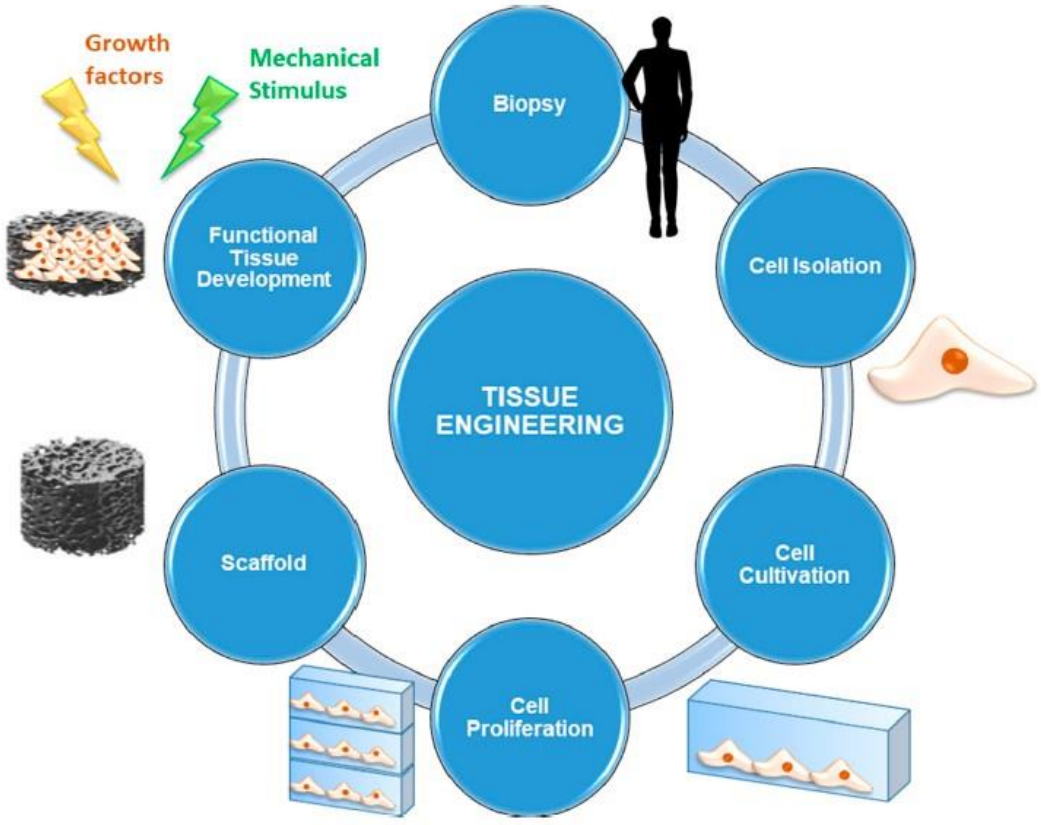

Figure 24. Most important elements for implementing tissue engineering [3].

Cells are the main important elements for the production of new tissue. Usually, they are directly taken from the desired site with a biopsy to avoid the risk of rejection from the patient. Another possibility is using stem cells, which are undifferentiated cells able to evolve into different cell lines under appropriate stimulations [3].

Scaffolds are 3D porous structures whose function is to provide temporary physical support to cells and stimulate their adhesion, migration, differentiation and proliferation. Their architecture is crucial for the development of an optimized microenvironment according to the tissue type and for the exchange of nutrients and waste between cells and the surroundings. Different types of materials can be used to synthesize scaffolds: natural scaffolds are made of biopolymers or ECM directly taken from the patient or donors, while synthetic scaffolds are produced using materials designed to mimic the characteristics of the original tissue [2], [3].

Signals are important elements for the stimulation of processes and cellular pathways responsible for cell proliferation and differentiation. They can be of different origin: biological, chemical, physical-mechanical. All the cells should receive signals and be influenced in the same way, in order to ensure the development of a functional tissue [3].

5.2 Basic requirements for BAGs scaffolds in bone TE

Since the 1990s, bioactive glasses have shown great potential in tissue engineering because of their bonding properties with the bone and the various possibilities of shaping them into 3D scaffolds. Currently, TE is still the main field for clinical applications of BAGs [3].

Scaffolds for bone tissue engineering must show some characteristics in order to induce the formation of a functional, mature tissue. The main important requirements are:

- **Biocompatibility**. Scaffolds must be biocompatible, which means that they must not release toxic products when in contact with biological fluids and the immune response after implantation in the host must be negligible to prevent the activation of inflammatory pathways [3].
- **Bioactivity**. The material of the scaffold must be able to promote osteogenic cells attachment and proliferation to stimulate new bone production, in other words it must be osteoconductive and possibly osteoinductive. Therefore, there should be no presence of a fibrous scar layer at the interface between host tissue and material, since it could hamper the formation of a bond with the bone [2], [3], [4].
- **Suitable degradation rate**. Scaffolds must dissolve with dissolution kinetics matching the ones of the healing tissue, to let it regenerate at the same time as the implant is disappearing. Moreover, the degradation products must be nontoxic and easy to be resorbed or excreted by the body [2], [3].
- **Porous and interconnected structure**. The presence of interconnected pores is essential to allow nutrients exchange, cell migration and vascularization. Indeed, the morphological features of a scaffold define the spatial distribution and orientation of the new tissue. An ideal scaffold should be highly permeable, with a porosity above 80-90 vol% and pore diameters between 10 and 500 µm, highly interconnected (>50 µm) reproducing the hierarchical structure of the bone. Large pores (100-500 µm) enhance vascularization and bone ingrowth, while pores between 2 and 10 µm increase the specific surface area, favoring protein adsorption and cell adhesion [3], [5].
- **Mouldability and easy fabrication.** Scaffolds must be easy to make into any shape and size, in order to completely fill bone defects according to the patient's characteristics. In addition, easy, scalable and low-cost fabrication should be viable for a production on large-scale [3].

- **Mechanical properties** should be kept during scaffold degradation and be comparable to the ones of the bone tissue in the implant site, avoiding mismatches which can cause bone resorption or breaking of the implant under loading [3].
- **Sterilization** of the surface and the bulk material must be possible following the biomedical devices regulations without modifications in the scaffold's original characteristics [3], [5].

Currently, an ideal scaffold fulfilling all the mentioned requirements does not exist. Research is trying to overcome the limits of BAG bone scaffolds, especially regarding their mechanical behavior. One great challenge is the possibility to combine a highly porous structure with adequate mechanical properties, compatible with the ones of the healing bone tissue [3].

Glasses possess an intrinsic brittleness which can cause mechanical failure of the device both during surgical implantation and the post operatory phase, because of cracks formation during the dissolution of the material [3]. Thermal treatments, such as sintering, are, therefore, necessary to reach adequate mechanical properties in scaffold manufacturing [3]. Sintering is a process that leads to the densification of a pre-shaped ceramic body, called green body, by heating it at a temperature between 50% and 75% of the melting temperature and keeping it for a certain period of time [5]. As a result, chemical bonds are created between powders, which become denser, and the green body volume is reduced (shrinkage). A sintered scaffold shows lower porosity in its 3D structure but enhanced mechanical strength [5].

However, silicate glasses were found to inhibit proper sintering because of the formation of crystals during the process [4]. Indeed, if concomitant crystallization occurs, typically from the surface, viscous flow is hindered, slowing down the sintering kinetics until all surface particles crystallize and the process stops [6]. This results in a poor-sintered scaffold, with lower mechanical and bioactive properties, since the rate of formation of HA decreases as well [4]. This phenomenon happens even though the sintering temperature is below the onset of crystallization, while at lower temperature no significant sintering occurs [4], [7]. For this reason, silicate bioactive glasses, such as 45S5 or S53P4, are not suitable for making scaffolds and are used only in powder form [7].

As a consequence, researchers have tried to develop other glass compositions able to avoid crystallization upon sintering. The bioactive glass 1393, for example, allows particle sintering and fiber drawing but was found to dissolve too slowly and be only osteoconductive [7]. More attention was, therefore, focused on new types of glasses, such as bioactive phosphate, borophosphate and borosilicate glasses. In particular, borosilicate glasses have emerged as a potential alternative since they convert faster and more completely into HA than silicate ones, and they have a low tendency to crystallize upon sintering, allowing the production of porous scaffolds. As investigated by Massera et al. [7], the borosilicate glass 1393 B20 is an example of a promising material for scaffold manufacturing, given its angiogenic and osteogenic properties because of the time-controlled boron release, and the ability to be sintered without crystallization.

Despite of bioactive glass composition, many techniques have been employed to increase the mechanical properties of the scaffolds for non-load bearing and load bearing applications. For example, it was found that high mechanical properties can be obtained with anisotropic scaffolds having pores with a specific orientation. This type of structure can be achieved with solid freeform fabrication (SFF) and unidirectional freezing of suspensions [5].

Figure 25 shows that several research groups were able to obtain scaffolds with mechanical properties similar to trabecular or cortical human bone tissue by using different scaffold manufacturing techniques.

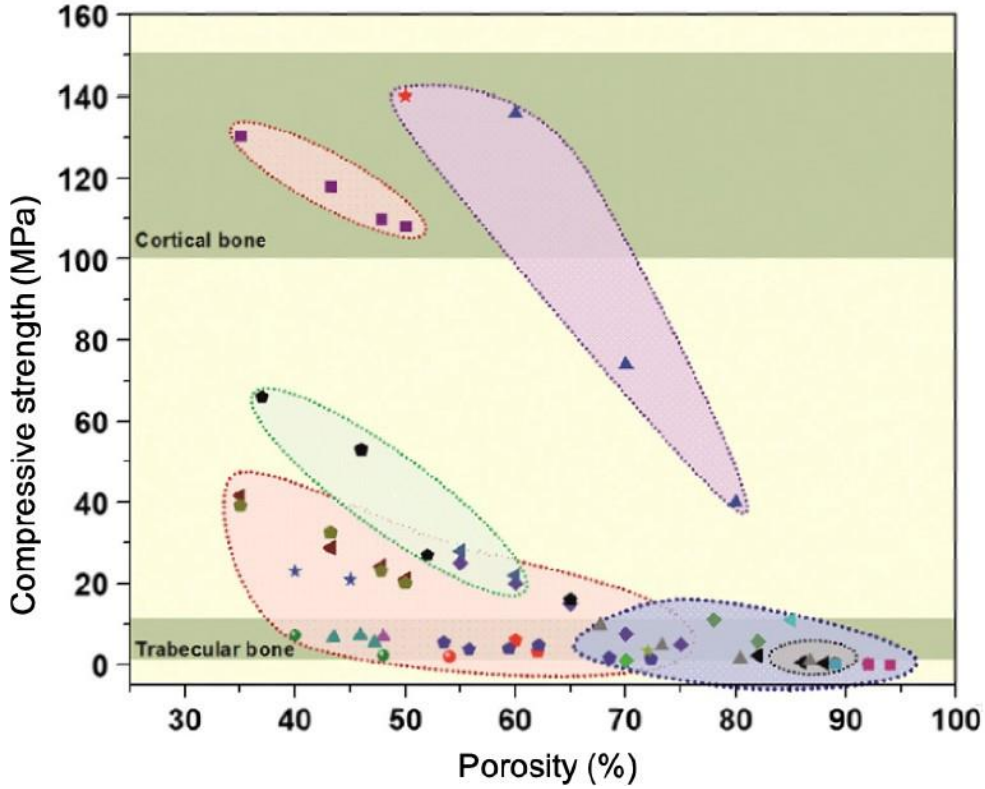

Figure 25. Compressive strength and porosity of bioactive glass scaffolds compared with human trabecular and cortical bone. From right bottom: gray represents sol-gel; green is freeze casting; pink is thermally bonded particles; purple is solid free-form fabrication and blue polymer foam replication [8].

Another important aspect to be considered when scaffolds are implanted for load bearing applications is their fracture toughness, which corresponds to the resistance of a material to crack propagation [8]. Glasses are characterized by an intrinsic low fracture toughness, which makes them very sensitive to small defects and flaws (~10 μm) [8]. Indeed, glasses can catastrophically fail in the presence of tensile or flexural stress much lower than their compressive strength [8].

The way human bones can considerably increase their fracture toughness is mainly through little adjustments and changes, such as crack deflection, organic bridging between mineral domains and microcracking [5], [8]. In particular, crack bridging through collagen fibrils has an important role in the toughening of bone [8]. That said, many studies took these mechanisms as an inspiration for finding methods to increase bioactive glass fracture toughness by creating composite scaffolds. For example, coating or infiltrating a scaffold with a biodegradable polymer, such as poly(ε-caprolactone) (PCL), can significantly increase the material toughness thanks to the creation of polymeric fibrils bridges which act in a similar way to the natural collagen fibrils in bone tissue [5], [8].

5.3 BAGs scaffolds manufacturing techniques

Since 2002, when the first bioactive glass scaffold was produced by Sepulveda et al. [9], many different manufacturing techniques have been developed by researchers to produce the optimal scaffold, which could meet all the requisites previously mentioned. In the next paragraphs, some of the main important techniques are illustrated.

5.3.1 Foaming methods

Foaming methods combine the presence of a melt-derived, or sol-gel, bioactive glass with a foaming agent to create air bubbles forming porosity. Air can be introduced through direct injection of gases, vigorous agitation, chemical reactions producing gas, or thermal decomposition of peroxides [5].

Despite the possibility to obtain scaffolds with a microstructure similar to the one of dry human trabecular bone, some drawbacks of this technique comprise low interconnectivity of the porous network, presence of closed pores, non-porous outer layer and low mechanical properties, in some cases just acceptable for bone repair. Foaming methods include gel-cast foaming, sol-gel foaming and H_2O_2 foaming [5], [8].

With gel-cast foaming, glass powders obtained from melt-quenching are mixed with a solution of organic monomers to form a slurry. The slurry is then poured into a mold where polymerization occurs. During the gelation process, foam is introduced either by injection of gases or by mechanical frothing, using a surfactant for the stabilization of the air bubbles. The material is then extracted from the mold and the solvent is eliminated, for example by drying in case of water. Finally, the organic components are removed through pyrolysis and the product is sintered. [5].

Sol-gel foaming was the method adopted to produce the first bioactive glass scaffold in 2002. It implicates the creation of a macroporous structure at the same time as the glass is synthesized by sol-gel method. Together with a surfactant, an accelerator is added to decrease the gelation time. This method allows the formation of two types of porosity: an interconnected macroporosity due to the surfactant action and a nanoporosity due to the intrinsic sol-gel texture. Despite the high brittleness of sol-gel glasses, recent process optimization allowed the production of porous scaffolds with a compressive strength of 5 MPa, acceptable value for cancellous bone repair [5].

Peroxide (H_2O_2) solution can be as well used as source for foaming, since, when heated at 60 °C, it releases vapor and oxygen which can produce bubbles. Glass powders are mixed with peroxide solution to form a slurry which is then cast into a mold, foamed at 60 °C, dried and sintered. The H_2O_2 percentage is an important parameter affecting the macroporosity level of the final product: by increasing the content of peroxide solution porosity, interconnectivity degree and pore size increase [5].

5.3.2 Thermal consolidation of particles

This method incorporates sacrificial particles, called porogen particles, with the green body before the molding phase. The particles can be of natural (e.g. starch, rice husk) or synthetic origin (e.g. PE particles) and must be fully removed by heat treatment before the sintering phase, in order to leave spaces and pores in the structure. If the removal process is not well controlled, an organic combustion residual (black char) could be deposited on the green body surface, preventing proper sintering and decreasing bioactivity. This method allows the production of a structure with gradients

of porosity at relatively low cost. However, it is not possible to reach levels of porosity higher than 70 vol% and pore interconnectivity results quite poor [5], [8].

An alternative to the use of a porogen agent is the production of a porous scaffold just by controlling the size of the glass particles and the sintering process. In particular, the sintering should be stopped when the formation of the sintering necks between the particles starts. Although this technique is very simple, the porosity level is quite low (< 50 vol%) and a strict control on particles shape and size is required [5].

5.3.3 Freeze casting of suspension

With freeze casting, a colloidal suspension of glass particles is poured into a mold and rapidly frozen. The frozen solvent is then removed by sublimation using a cold temperature vacuum (- 20°C), leaving a porous network in the material. At this point, the scaffold is dried and sintered [5], [8].

During freezing, the presence of a non-homogeneous cooling rate in the different directions leads to the growth of ice crystals with a preferred orientation, resulting in a porous scaffold with an oriented microstructure. This aspect is strictly related to an increased compressive strength in the direction of the orientation compared to other fabrication methods, making this type of scaffolds promising for load-bearing applications [5], [8].

However, it should be taken into account that water-based colloidal suspensions are not suitable, since the resulting pore size is too small for tissue ingrowth (10-40 μm). Therefore, it is necessary to include an additional organic solvent to obtain larger pores and pass from a lamellar microstructure to a columnar one, which can partially reproduce the structure of cortical bone [5], [8].

5.3.4 Additive manufacturing technologies

Additive manufacturing technologies (AMT), also known as solid freeform fabrication (SFF), refer to a group of techniques in which the product realization is carefully controlled “layer by layer” or “piece by piece”, using a bottom-up approach. These methods distinguish from the conventional ones because they allow the creation of many different shapes increasing the level of flexibility, industrial scalability and customization. Indeed, it is possible to produce patient-specific devices and, in most of the cases, no toxic solvents are used [5], [8].

The realization of the product starts with a predesigned CAD model, or computed tomography (CT), of the object intended to be constructed. The model is then divided into layers along one of the object’s axes and the machine implements the data by adding each layer at time to obtain the physical product [5], [8].

Additive manufacturing techniques have the great advantage of being employed for any kind of materials: metals, polymers, ceramics, glasses and living substances (cells). Regarding ceramic materials, AMT can be divided into indirect and direct, depending on the need for a post-treatment, such as sintering, or not, respectively [5].

AMT can be classified into four main categories:

- **Laminated object manufacturing.** The material is divided into sheets which are deposited, glued together and cut into the desired shape [5].

- **Extrusion-based techniques**. The material is extruded through a robot-controlled nozzle in the form of a filament and deposited. Robocasting, fused model deposition and dispense plotting belong to this category [5].
- **Methods based on stereolithography apparatus (SLA).** These techniques make use of a light beam, such as a laser to create a 3D object [5].
- **Fusing of bed powders.** Powders are added layer by layer and selectively fused according to the scaffold design, for example with a laser beam, as in selective laser sintering (SLS) method [5].

Among the different AMT, the direct ink writing methods (DIW) comprise a big family of manufacturing methods. These techniques make use of a computer-controlled stage able to translate and move a device, such as a nozzle or a print head, which can assemble the final product. The material deposition can be droplet-based if an ink-jet print head deposits the substance on a chosen path, or filamentary if the material is extruded through a nozzle as continuous filament. In the next paragraphs, some of the most important DIW techniques are illustrated [5].

5.3.4.1 3D printing

With 3D printing, each layer of the scaffold is built by adding a powder sheet, on which a water or organic-based binder is deposited. After each layer deposition, powders are dried and reinforced by heating. The way the binder moves follows a pattern from a CAD model. The printing type can be continuous ink-jet (CIJ) or drop-on-demand (DOD). With the first one, acoustic waves generate continuous flow of drops, which are then deviated by an electric field, while with the latter drops are released when needed with a piezoelectric or thermal system. After the building of all the layers, the loose powder is removed through a process called de-powdering, and a final heat treatment burns out the binder and sinter the glass particles [5].

Particle size, shape, roughness and size distribution are important characteristics through which it is possible to control the flowability and packing ability of the particles. To have a good packing ability usually round particles are used, with a size between 20 and 40 μm [5].

3D printing is a promising technique which can allow the production of scaffolds with a porosity ≥ 50 vol%. However, crystalline phases might form during the process or, if the mechanical properties obtained are suitable for load-bearing applications, the resulting porosity is low (< 50 vol%) [5].

5.3.4.2 Ink-jet printing (IJP)

This technique is very similar to the 3D printing but, instead of having an ink only containing the binder, the ink contains both the binder and the glass particles. The ink is deposited as droplets, with mechanisms similar to CIJ or DOD, and the object is built layer-by-layer [5].

IJP allows a better spatial accuracy on the x-y plane, compared to 3D printing, which depends on the physical and chemical properties of the ink, such as the wettability, surface tension and interaction between the droplets [5].

It can be used to synthesize scaffolds based on natural (e.g. agar, alginate, cellulose) or synthetic (e.g. poly[lactic acid], poly[capro lactone], hydrogels) polymers, but also calcium phosphates (e.g. HA, tri-calcium phosphate). Despite their promising characteristics, glass-based IJP printed scaffolds have not yet been reported in literature [5].

5.3.4.3 Robocasting

Robocasting is the most widely used and effective DIW technique. As shown in Figure 26, a continuous filament is extruded through a nozzle by using pressurized air and deposited by a robotic head following a CAD file [5].

In robocasting, there are two main methods of ink extrusion: the first one ejects the ink at a constant flow rate with a variable pressure, the second one uses pressurized air at a constant pressure value [5].

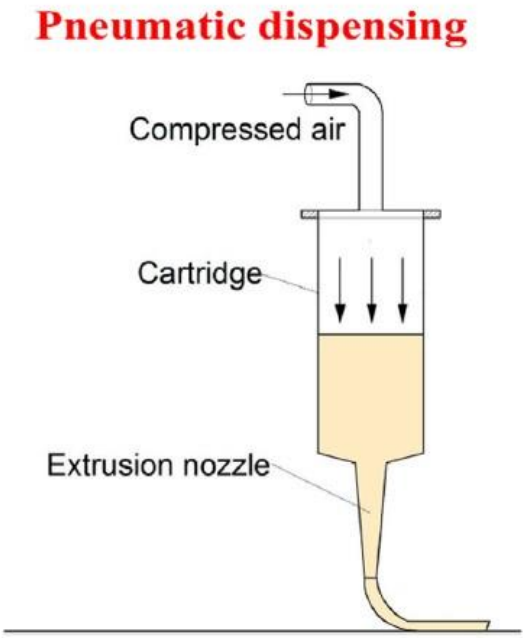

Figure 26. Robocasting procedure. Compressed air applies a certain pressure on the ink inside of a cartridge to ensure a continuous flow through a nozzle [10].

Ceramic particles and a polymeric binder are mixed together to form the ink, which has the consistency of a slurry. The ink must be pseudoplastic, namely following a shear-dependent viscous behavior. In particular, the relationship between shear stress and shear rate of a pseudoplastic fluid is described by the Hershel-Bulkley equation, reported below as Equation 6 [5], [11].

$$\tau = \tau_y + K(\dot{\gamma})^n$$

Equation 6. Hershel-Bulkley equation [11].

Where τ_y is the yield stress, K is the consistency factor, $\dot{\gamma}$ is the shear rate and n is the flow behavior index.

The parameter n changes according to the specific viscous behavior:

- In case of a Newtonian fluid: $n = 1$. The viscosity is independent of the applied shear rate and the rate of deformation is directly proportional to the shear stress [12].
- In case of dilatant or shear thickening $n > 1$. With increasing shear rate, the viscosity increases and the shear stress increases with decreasing slope [5], [13].

- In case of pseudoplastic or shear thinning $n < 1$. With increasing shear rate, the viscosity decreases and the shear stress increases with increasing slope [5], [13].

A pseudoplastic ink can flow through the nozzle without applying a high pressure, as its viscosity decreases with increasing shear stress [5].

Another important characteristic of the ink is the ability to maintain the rod-like structure after its deposition on the surface. Moreover, it should possess enough mechanical strength to avoid excessive deformation when another layer is deposited on the previous one. The printing substrate should be perfectly plane and allow attachment of the ink during printing and, at the same time, easy detachment of the dried product [5].

Among the different polymeric binders, Pluronic F127, ethyl cellulose/PE glycol and carboxymethyl cellulose are the most common ones [5]. Pluronic F127, in particular, is a triblock copolymer which is characterized by a reversible thermogelling process in aqueous solutions, passing from a solution to a gel-like state when the temperature overcomes the gel temperature T_g [14]. When the material is at a temperature below T_g water adsorbs on the PPO block polymer, making the chain slide across each other. The material at this condition is a solution. When the temperature overcomes the T_g, adsorption of water is not favored, so the polymeric chains form micelles with PPO as a core and PEO as a shell, leading to a gel-like state [14], [15].

When glass particles are mixed with Pluronic F127, Van der Waals forces or hydrogen bonding are created between the hydroxyl group of the polymeric chains and the particles' surface, stabilizing the structure. Moreover, the presence of glass lowers the T_g, since water preferably bonds to glass than to Pluronic [5].

Robocasting is a very promising method for glass-based scaffold manufacturing, through which it is possible to obtain scaffolds with a porosity between 50 and 70 vol%, possibly suitable for load bearing applications. In addition, it allows the creation of functionally graded porous objects with easy control of the structure. Glass particles size usually ranges between 1 µm and 30 µm, while the extrusion nozzles possess a diameter between 100 and 580 µm [5].

5.4 Multifunctional bone scaffolds

3D porous bone scaffolds are well known for their ability to promote bone tissue regeneration in the repair of critical bone defects caused by traumas, tumor excisions, or degenerative diseases [16]. However, combining bone regeneration ability with additional properties is often necessary to better mimic the complex ECM and address multiple challenges at the same time, creating in this way a multifunctional scaffold [17].

Multifunctional scaffolds can integrate tissue regeneration with numerous therapies, such as cell therapy, gene therapy, or immunomodulatory therapy [17]. In the context of multifunctional bone scaffolds, two main synergistic treatments are combined with bone tissue repair: prevention of bone infections and treatment of bone cancer [18].

5.4.1 Antimicrobial scaffolds

Antimicrobial scaffolds aim to prevent or destroy bacterial colonization and resistance following the implantation of a bone repair scaffold [19]. Specifically, bone scaffolds can acquire antimicrobial properties through various approaches:

- **Scaffolds with intrinsic antimicrobial effect**. An antimicrobial agent is incorporated into the scaffold composition, where it remains exposed on the surface. The antimicrobial activity is performed by the electrostatic interactions between the antimicrobial agent and the bacterial membrane, which destabilizes. Usually, the antimicrobial agent is a natural polymer, such as ϵ-poly-L-lysine, or chitosan [19].
- **Scaffolds loaded with antibiotics**. Prevention or treatment of bacterial infections can also be achieved through the introduction of antibiotics within the scaffold. Different types of scaffolds ranging from synthetic organic biopolymers to inorganic or composite materials can be loaded with antibiotics, such as ciprofloxacin, rifampin, or vancomycin. However, given the growing concern over antibiotic resistance, research is focusing more on free-antibiotic alternatives [19].
- **Scaffolds doped with metallic ions**. Metallic ions possessing antimicrobial properties, such as copper or silver, can be employed as free-antibiotic alternatives. They can be incorporated into the scaffold structure and directly delivered to the defect site. For example, a Sr/Zn co-doped porous HA scaffold has demonstrated to successfully reduce bacterial infection due to the antimicrobial properties of zinc [19].
- **Scaffolds incorporating nanoparticles.** Delivering of metallic ions or drugs can be efficiently and better performed through the use of nanoparticles as nanocarriers, since the release is more controlled due to their confinement without the possibility of targeting other cells or tissues. Metallic ions, such as silver, copper, or zinc can be successfully incorporated into NPs, as well as antibiotics [19].

5.4.2 Scaffolds for bone cancer treatment

Despite the acquisition of antimicrobial properties, the ability to treat bone cancer is another important challenge in the context of bone tissue engineering scaffolds. Indeed, when critical size bone defects need to be repaired following a bone cancer surgical removal, cancerous cells potentially remaining in the defect have a high potential of causing recurrence. Multifunctional scaffolds able to support bone proliferation and simultaneously kill cancer cells are, therefore, highly requested [18].

Three main strategies can be adopted for designing this type of multifunctional scaffolds. The first approach makes use of chemotherapeutic drugs embedded in the scaffold with the idea of a targeted drug delivery or localized and controlled drug release. The second method utilizes photothermal therapy, in which a catalyst embedded in the scaffold is excited by a near-infrared laser, generating heat release at the tumor's site with negative effects on cancer cells. The third strategy is of great and increasing interest, as it involves the use of magnetic scaffolds for hyperthermia therapy [18].

In the following paragraphs, this last approach is seen in more detail and different methods for producing magnetic scaffolds are illustrated.

5.4.2.1 Magnetic scaffolds for bone cancer treatment

With the growing development of hyperthermia, magnetic scaffolds have attracted great interest among researchers, since they can be used as a magnetic field-sensitive heat source for the treatment of bone cancer [20]. Figure 27 gives an illustrative example of this specific use for magnetic scaffolds.

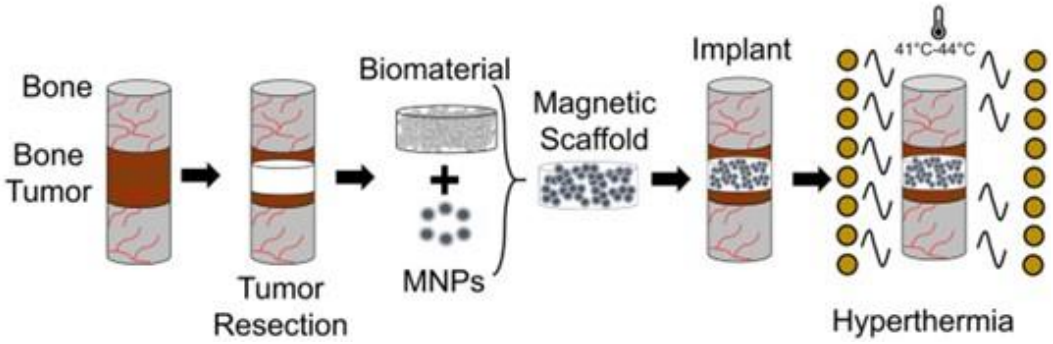

Figure 27. Use of magnetic scaffolds for hyperthermia in the treatment of bone cancer. Figure adapted by Lodi, Matteo Bruno, et al. [20].

A scaffold can become magnetic in different ways. Generally, the simplest approach consists in mixing magnetic NPs with a biocompatible scaffold. For example, Superparamagnetic Iron Oxide Nanoparticles (SPIONS) can be coated with polyacrylic acid (PAA) to increase their colloidal stability and then incorporated into a composite scaffold made of gelatin and HA by dip-coating. With dip-coating, the polymeric template of the scaffold is immersed in the colloidal suspension of MNPs, which are then adsorbed to the HA particle's surface. This method proved to obtain samples able to increase their temperature when exposed to a magnetic field accordingly to the MNPs content, with promising perspectives for hyperthermia applications [21].

A similar result can be obtained with the incorporation of Fe_3O_4 NPs in a polycaprolactone (PCL) scaffold matrix. This approach allows to combine the magnetic properties of the NPs with the advantageous characteristics of PCL, such as bioresorbability, inexpensive production routes, easy manipulation, tailorable degradation kinetics and mechanical properties [21].

Despite the co-precipitation in aqueous solution of ferrous and ferric salts, magnetic nanoparticles can be also synthetized by chemical doping of HA with magnetic ions. More specifically, during the HA formation both Fe species are introduced in a controlled manner and the crystallographic positions of Ca(1) and Ca(2) in the apatite lattice are replaced by Fe^{3+} and Fe^{2+} ions, respectively. This process leads to the formation of local superparamagnetic iron oxide domains within the HA lattice [21]. This FeHA nanopowder can be used to further coat bioactive glass-based scaffolds, allowing their magnetization, as demonstrated in previous studies [22].

In summary, magnetic scaffolds represent a promising advancement in tissue engineering. Their ability to be activated by an external magnetic field opens new possibilities, not only for hyperthermia treatment, but also because of the possibility to generate remotely magnetic stimuli which can guide growth factors-loaded nanocarriers to specific sites and trigger thermally induced drug delivery [21].

REFERENCES

[1] Joseph P Vacanti and Robert Langer, “Tissue engineering: the design and fabrication of living replacement devices for surgical reconstruction and transplantation,” 1999.

[2] M. N. Rahaman *et al.*, “Bioactive glass in tissue engineering1,” *Acta Biomaterialia*, vol. 7, no. 6, pp. 2355–2373, Jun. 2011, doi: 10.1016/j.actbio.2011.03.016.

[3] E. Fiume, J. Barberi, E. Verné, and F. Baino, “Bioactive Glasses: From Parent 45S5 Composition to Scaffold-Assisted Tissue-Healing Therapies,” *JFB*, vol. 9, no. 1, p. 24, Mar. 2018, doi: 10.3390/jfb9010024.

[4] Jonathan Massera, “Bioactive Glass in Tissue Engineering: Progress and Challenges,” *ATROA*, vol. 1, no. 1, Aug. 2016, doi: 10.15406/atroa.2016.01.00002.

[5] F. Baino *et al.*, “Processing methods for making porous bioactive glass-based scaffolds—A state-of-the-art review,” *Int J Applied Ceramic Tech*, vol. 16, no. 5, pp. 1762–1796, Sep. 2019, doi: 10.1111/ijac.13195.

[6] M. O. Prado and E. D. Zanotto, “Glass sintering with concurrent crystallization,” *Comptes Rendus. Chimie*, vol. 5, no. 11, pp. 773–786, Nov. 2002, doi: 10.1016/S1631-0748(02)01447-9.

[7] A. Szczodra *et al.*, “Boron substitution in silicate bioactive glass scaffolds to enhance bone differentiation and regeneration,” *Acta Biomaterialia*, vol. 186, pp. 489–506, Sep. 2024, doi: 10.1016/j.actbio.2024.07.053.

[8] Q. Fu, E. Saiz, M. N. Rahaman, and A. P. Tomsia, “Bioactive glass scaffolds for bone tissue engineering: state of the art and future perspectives,” *Materials Science and Engineering: C*, vol. 31, no. 7, pp. 1245–1256, Oct. 2011, doi: 10.1016/j.msec.2011.04.022.

[9] Pilar Sepulveda, Julian R. Jones, Larry L. Hench, “Bioactive sol-gel foams for tissue repair,” 2002.

[10] S. Lamnini, H. Elsayed, Y. Lakhdar, F. Baino, F. Smeacetto, and E. Bernardo, “Robocasting of advanced ceramics: ink optimization and protocol to predict the printing parameters - A review,” *Heliyon*, vol. 8, no. 9, p. e10651, Sep. 2022, doi: 10.1016/j.heliyon.2022.e10651.

[11] USACE Hydrologic Engineering Center • Powered by Scroll Viewport and Atlassian Confluence, “Hershel-Bulkley Parameters,” HEC-RAS Mud and Debris Flow. Accessed: Jan. 17, 2025. [Online]. Available: https://www.hec.usace.army.mil/confluence/rasdocs/rasmuddebris/non-newtonian-user-s-manual/user-inputs-and-model-parameters/hershel-bulkley-parameters#:~:text=The%20Herschel%2DBulkley%20model%20simulates,material%20more%20difficult%20to%20deform.

[12] A. Madhlopa, “Hydrodynamics of solar receivers,” in *Solar Receivers for Thermal Power Generation*, Elsevier, 2022, pp. 213–250. doi: 10.1016/B978-0-323-85271-5.00008-2.

[13] Science learning hub, “Shear thinning and shear thickening liquids.” Accessed: Feb. 24, 2025. [Online]. Available: https://www.sciencelearn.org.nz/images/1846-shear-thinning-and-shear-thickening-

liquids#:~:text=Some%20liquids%20behave%20differently%20when,in%20viscosity%20as%20stress%20increases.

[14] M. Jalaal, G. Cottrell, N. Balmforth, and B. Stoeber, “On the rheology of Pluronic F127 aqueous solutions,” *Journal of Rheology*, vol. 61, no. 1, pp. 139–146, Jan. 2017, doi: 10.1122/1.4971992.

[15] R. K. Prud’homme, G. Wu, and D. K. Schneider, “Structure and Rheology Studies of Poly(oxyethylene−oxypropylene−oxyethylene) Aqueous Solution,” *Langmuir*, vol. 12, no. 20, pp. 4651–4659, Jan. 1996, doi: 10.1021/la951506b.

[16] A. Ortolani *et al.*, “The prospective opportunities offered by magnetic scaffolds for bone tissue engineering: a review,” *Joints*, vol. 04, no. 04, pp. 228–235, Oct. 2016, doi: 10.11138/jts/2016.4.4.228.

[17] N. Muzzio, S. Moya, and G. Romero, “Multifunctional Scaffolds and Synergistic Strategies in Tissue Engineering and Regenerative Medicine,” *Pharmaceutics*, vol. 13, no. 6, p. 792, May 2021, doi: 10.3390/pharmaceutics13060792.

[18] A. Bigham, F. Foroughi, E. Rezvani Ghomi, M. Rafienia, R. E. Neisiany, and S. Ramakrishna, “The journey of multifunctional bone scaffolds fabricated from traditional toward modern techniques,” *Bio-des. Manuf.*, vol. 3, no. 4, pp. 281–306, Dec. 2020, doi: 10.1007/s42242-020-00094-4.

[19] M. Vallet-Regí, D. Lozano, B. González, and I. Izquierdo-Barba, “Biomaterials against Bone Infection,” *Adv Healthcare Materials*, vol. 9, no. 13, p. 2000310, Jul. 2020, doi: 10.1002/adhm.202000310.

[20] M. B. Lodi *et al.*, “Design and Characterization of Magnetic Scaffolds for Bone Tumor Hyperthermia,” *IEEE Access*, vol. 10, pp. 19768–19779, 2022, doi: 10.1109/ACCESS.2022.3151470.

[21] M. Banobre-Lopez *et al.*, “Hyperthermia Induced in Magnetic Scaffolds for Bone Tissue Engineering,” *IEEE Trans. Magn.*, vol. 50, no. 11, pp. 1–7, Nov. 2014, doi: 10.1109/TMAG.2014.2327245.

[22] M. L. Dittler *et al.*, “Magnetic 3D scaffolds for tissue engineering applications: bioactive glass (45S5) coated with iron-loaded hydroxyapatite nanoparticles,” *Biomed. Mater.*, vol. 16, no. 5, p. 055006, Sep. 2021, doi: 10.1088/1748-605X/ac14cc.

6. MATERIALS AND METHODS

6.1 Preparation of Superparamagnetic Iron Oxide Nanoparticles (SPIONS)

Superparamagnetic Iron Oxide Nanoparticles (SPIONS) were prepared in Politecnico di Torino (Turin, Italy) using the co-precipitation method in aqueous solution. $FeCl_2 \cdot 4H_2O$ and $FeCl_3 \cdot 6H_2O$ (Sigma Aldrich) were weighted and mixed with bi-distilled water, separately, using a magnetic stirrer, in order to obtain a molarity of 0.1 M for each solution. The two solutions were then mixed together in a quantity that resulted in a stoichiometric ratio of Fe^{2+}/Fe^{3+} of 1:2. The pH of the solution was measured and adjusted to around 10 by addition of NH_4OH (Sigma Aldrich).

At this point, the solution turned black and was placed in an ultrasound bath for 20 minutes, leading to the growth of Fe_3O_4 nanoparticles (magnetite). The solution of NPs was then separated using magnets and washed with bi-distilled water, to remove the traces of ammonium ions and residual salts. Figure 28 shows the separation of NPs from the liquid part by placing a magnet at the bottom of the beaker.

Later, a solution of citric acid $C_6H_8O_7$ (Sigma Alrich) 0.05 M was added to the washed magnetite solution to improve the NPs dispersion in water. NH_4OH was added again dropwise to adjust the pH at 5.2 and, after that, the solution was placed in an orbital shaker (KS 4000i control, IKA) at 150 rpm for 90 minutes at 80 °C.

Figure 28. Separation of NPs from the liquid phase with a magnet.

After the surface coating of NPs with citric acid, the solution was washed twice with bi-distilled water using an ultrafiltration device (Solvent Resistant Stirred Cells – Merck Millipore), as shown in Figure 29. As the last step, the NPs were re-suspended in bi-distilled water and pH was adjusted at 10.2 by using NH_4OH, to ensure an optimal NPs dispersion.

Figure 29. Ultrafiltration of liquid solution of Fe_3O_4 NPs and citric acid.

The concentration of each SPIONS solution was evaluated by pouring 500 µL of solution in an Eppendorf tube, placing it in an incubator at 37 °C until the SPIONS became dry, and weighing the mass of the dry SPIONS. The concentrations of the different batches ranged from 18.2 mg/ml to 20 mg/ml.

The SPIONS solution was stored in plastic jars, as shown in Figure 30, and sent to Tampere University, Hervanta Campus (Tampere, Finland).

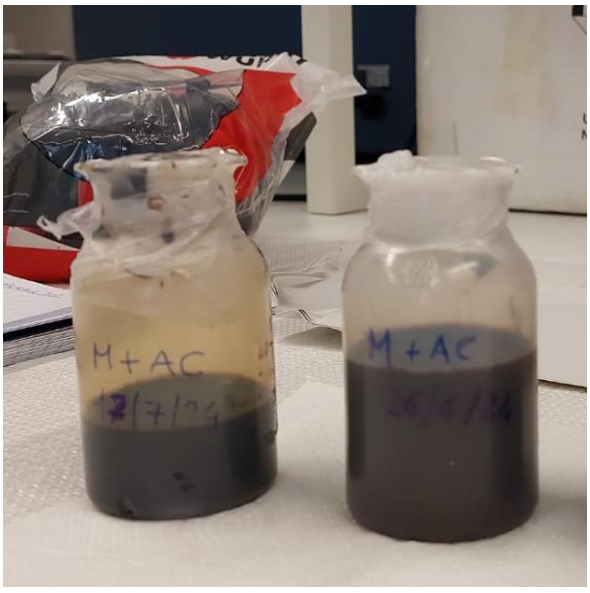

Figure 30. Liquid SPIONS solutions.

6.2 Transmission Electron Microscopy analysis

Transmission Electron Microscopy (TEM) images of SPIONS both as dry powder and in liquid solution were acquired. The samples were put in Eppendorf tubes and sent to the Microscopy Center of

Hervanta Campus, Tampere. Powder samples were prepared by crushing a small amount of dry SPIONS between microscope slides and dispersing the powder with isopropanol onto a holey-carbon-coated copper grid. Liquid samples were prepared by pipetting some drops of SPIONS solution onto a holey-carbon-coated copper grid.

The diameter of the particles was calculated by analyzing the acquired images with the software ImageJ2 1.54 (National Institutes of Health, USA). The images were calibrated in the software by setting the correct scale corresponding to that of the acquired images and the particles' diameter was acquired manually. Results are presented as the average of 5 measurements ± STD.

6.3 Preparation of bioactive glass 1393 B20

Bioactive glass 1393 B20 was prepared starting from the weighing and mixing of analytical grade $CaCO_3$, HBO_3, MgO, $(NH_4)H_2PO_4$, K_2CO_3, Na_2CO_3 and Belgian quartz sand (Sigma Aldrich and VWR). Table 3 shows the nominal composition of the glass, while Table 4 shows the mass of each reagent used in the preparation.

Table 3. Nominal composition of 1393 B20 bioactive glass.

Compounds	**mol %**
CaO	22.10
B_2O_3	10.92
MgO	7.70
P_2O_5	1.70
K_2O	7.90
Na_2O	6.00
SiO_2	43.68

Table 4. Mass of each reagent used for glass preparation.

Reagents	**Weight of raw materials ± 0.005 (g)**
$CaCO_3$	28.124
HBO_3	17.199
MgO	3.946
$(NH_4)H_2PO_4$	4.973
K_2CO_3	13.882
Na_2CO_3	8.086
SiO_2	33.370

All the reagents were put in a platinum crucible and melted in a furnace. The melting temperature profile is presented in Figure 31. The molten glass was mixed 30 minutes after the temperature reached 1450 °C, and the casting was done in a graphite mold at room temperature 30 minutes after the mixing. Subsequently, the glass was annealed at 500 °C for 8 hours.

After melting and annealing, the glass was crushed and milled using a planetary ball mill (Fritsch GmbH, Idar-Oberstein, Germany) and sieved (Gilson Company, Inc., Ohio, USA) to obtain glass particles with a diameter size <38 µm.

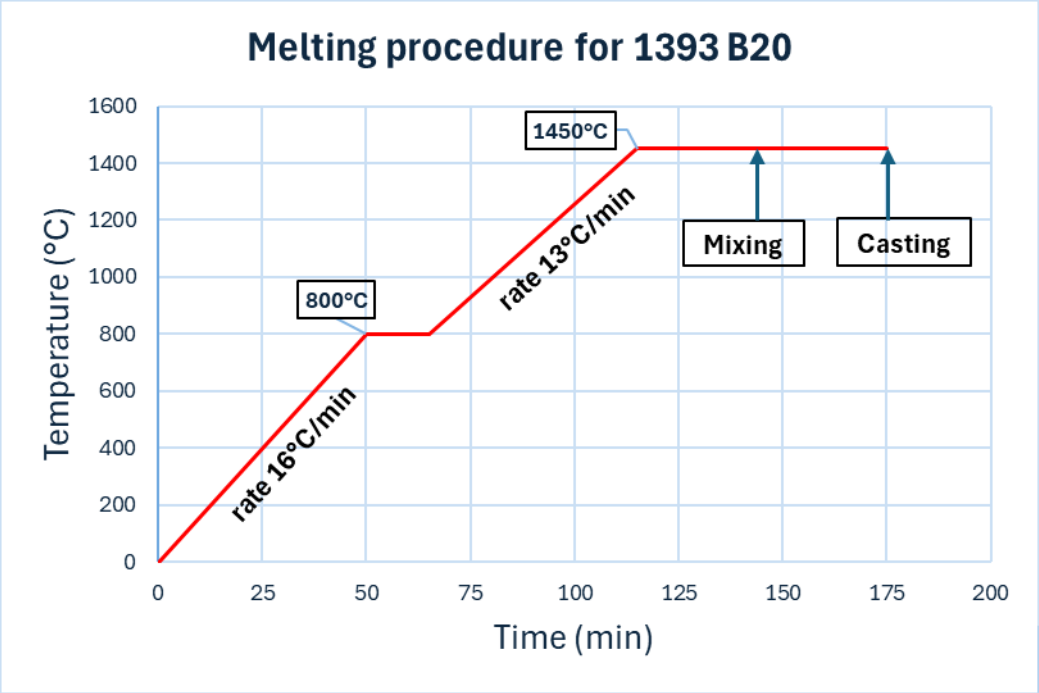

Figure 31. 1393 B20 melting temperature profile.

6.4 Scaffold production

Scaffolds were produced through robocasting technique using 3Dn-Tabletop printer (nScrypt Inc., Orlando, Florida, USA) and the software Machine Tool 3.0 system. The script used for 3D printing was set to obtain 5 layers cylindrical samples, with a diameter of 5 mm and height of 1 mm.

Four types of glass/SPIONS concentrations were tested, so four types of ink for robocasting were developed.

6.4.1 Ink for 100:0 wt% glass/SPIONS scaffolds

The ink was created starting from the preparation of a 30 wt% Pluronic solution as a binding agent. Pluronic F127 (Sigma Alrich) and distilled water were weighed in a ratio of 30:70 wt%, respectively, and mixed in an ice bath with a magnetic stirrer for 6 hours until the solution turned clear, as shown in Figure 32. Pluronic solution was stored in the fridge at 4 °C.

For the ink preparation, 1393 B20 glass powder and Pluronic solution were weighed in a ratio of 30:70 wt%, respectively, and mixed thoroughly using Vibrofix VF1 electrical shaker (IKA®-Labortechnic, Staufen, Germany). Several cycles of mixing/resting in ice bath were done to keep the Pluronic solution liquid. The mixing procedure was repeated in the same way for all the types of ink.

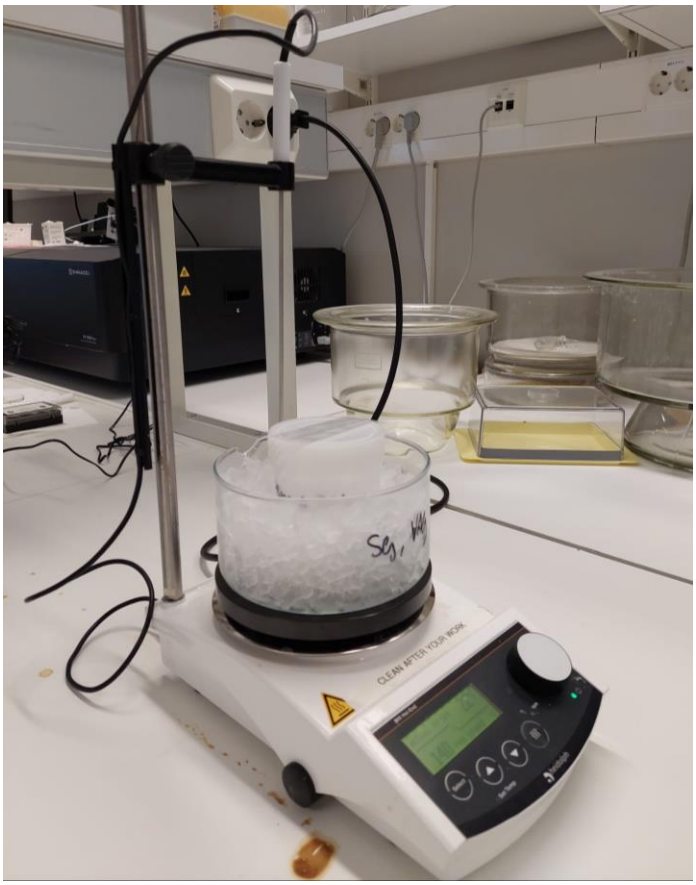

Figure 32. Magnetic stirring of 30wt% Pluronic solution in an ice bath.

6.4.2 Ink for 95:5 wt% wet glass/SPIONS scaffolds

For this type of ink, the 30 wt% Pluronic solution was obtained using Pluronic F127 and SPIONS suspended in water. The volume of SPIONS solution was equal to the one required for the water in the preparation of the water-based Pluronic solution. This amount was obtained from the partial evaporation of the original SPIONS solution, depending on the mass of SPIONS needed. By knowing the concentration of the SPIONS solution, the required mass of SPIONS was calculated considering a ratio of bioactive glass/SPIONS equal to 95:5 wt%, respectively. At the same time, the required mass of 1393 B20 was determined. The masses of 1393 B20+SPIONS and of Pluronic solution followed the ratio of 30:70 wt%, respectively.

6.4.3 Ink for 95:5 wt% and 90:10 wt% dry glass/SPIONS scaffolds

In this case, the liquid solution of SPIONS was first frozen and then put in a freeze drying machine until all the water evaporated and SPIONS were left as powder. The masses of SPIONS and bioactive glass were calculated considering a ratio of 95:5 wt% or 90:10 wt% and the 30 wt% Pluronic solution was prepared using water, as for the 100:0 wt% glass/SPIONS ink. In the ink preparation, SPIONS were first weighed and then crushed in a mortar, in order to reduce the particle agglomerates. After that, 1393 B20 glass powder was weighed and crushed with the SPIONS, until the mixture was homogeneous. Finally, Pluronic solution was added, respecting the ratio 30:70 wt% for 1393 B20+SPIONS and Pluronic solution.

After its preparation, the ink was transferred to Optimum® 3cc printing cartridge (Nordson EFD, Bedfordshire, England) and left for 1 hour at room temperature to stabilize. For 3D printing, a

SmoothFlow Tapered Tip with tip diameter of 0.41 mm (Nordson EFD Optimum® SmoothFlow™, Westlake, Ohio, USA) was attached to the cartridge and the extruded ink was deposited on acrylic sheets. The applied pressure for a continuous flow was in the range of 15-30 psi. Printed scaffolds were then left for 24 hours to dry at 37 °C, to reduce the risk of collapse and to let the residual water evaporate.

Subsequently, scaffolds were sintered at 625 °C in an electric muffle furnace (Nabertherm LT 9/11/SKM), following the procedure illustrated in Figure 33. Sintered scaffolds were placed in multiwell plates and stored in a desiccator for further analysis.

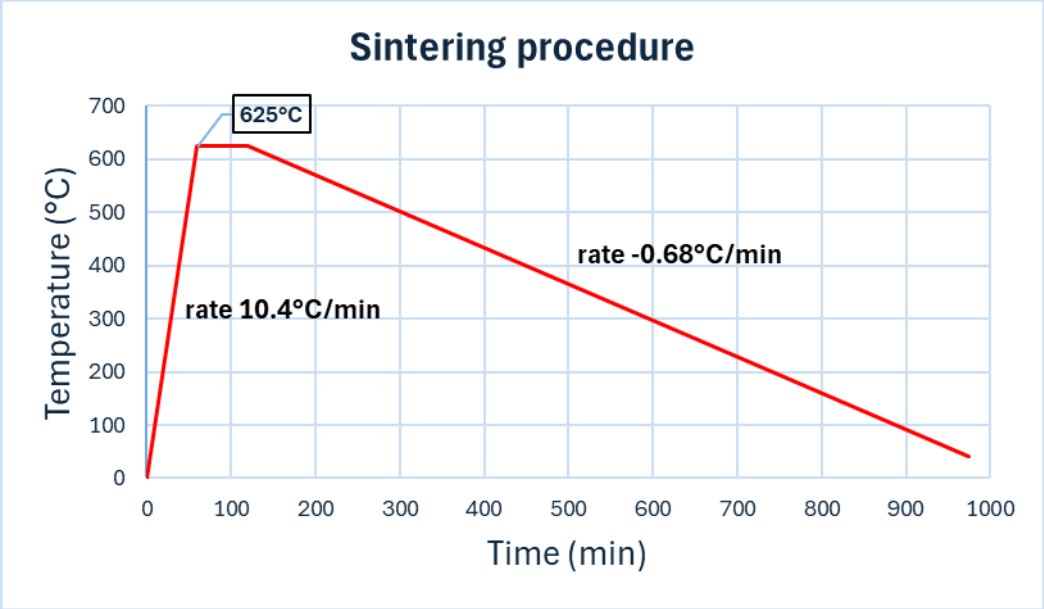

Figure 33. Sintering procedure of the scaffolds.

6.5 Rheology testing

The rheological properties of the Pluronic solutions (water based and with liquid SPIONS) and of the four inks were studied using a Discovery HR-2 rotational rheometer and TRIOS software (TA Instruments, U.S.A.). Approximately 200 µl of sample were put between parallel plates of stainless steel with a diameter of 12 mm and a gap of 800 µm to test the viscosity and the shear stress as a function of the shear rate, which varied in the range 0.01-1000 s^{-1}. The test was performed at room temperature (25 °C) and for each type of solution 3 samples were tested. The average shear stress and viscosity were calculated along with the standard deviation and represented as graphs.

6.6 Mechanical testing

The mechanical properties of the scaffolds (Young's modulus, fracture strength) were studied under compression using Instron Electropuls®, E1000 testing machine and Bluehill Universal® Software. For each scaffold composition 5 samples were tested, from which the graph representing the compressive stress as a function of the compressive strain was obtained. Average Young's modulus and average fracture strength were extracted and reported as mean ± SD.

6.7 In vitro dissolution test

The dissolution behavior of the scaffolds was studied by immersing them in SBF and analyzing the ion release at different time points.

6.7.1 SBF preparation

One liter of SBF was prepared starting from the addition of the reagents 1-8, presented in Table 5, to 700 ml of distilled water. Reagents were dissolved one at a time and, after that, water was added to reach 900 ml. The solution was incubated at 37 °C for 2 hours, after which TRIS was added slowly until the pH reached 7.45±0.01 while the solution was kept at 37 °C on a heating platform. 1 M-HCl and the remaining part of TRIS were added carefully to reach a pH of 7.40±0.01. Finally, distilled water was added to reach a final volume of 1000 ml and the solution was stored in the fridge.

Table 5. Quantity of each reagent for SBF preparation.

	Reagent	**For 1 L of SBF**
1	NaCl	8.035 g
2	$NaHCO_3$	0.335 g
3	KCl	0.225 g
4	$K_2HPO_4 \cdot 3\ H_2O$	0.231 g
5	$MgCl_2 \cdot 6\ H_2O$	0.311 g
6	1M- HCl	39 ml
7	$CaCl_2 \cdot 2\ H_2O$	0.308 g
8	Na_2SO_4	0.072 g
9	TRIS	6.118 g
10	1M- HCl	0-5 ml

6.7.2 Samples preparation and ICP analysis

The SBF testing was performed for up to 1 week. For all conditions, 4 time points (24 h, 48 h, 72 h, 1 week) were studied in triplicate. Each scaffold was first weighed and then placed in a 15 ml plastic tube, where it was added 1 ml of SBF at 37 °C to 10 mg of bioactive glass ratio. The tubes were placed in a dynamic incubator at 100 rpm at 37 °C. In addition to the different scaffold compositions, samples of SBF control were studied at all time points to ensure the stability of SBF over time. During the experiment, the SBF solution was not refreshed.

At each time point, pH of the solution at 37 °C was measured and 1 ml of solution was collected and placed in an empty tube where 9 ml of 1 M-HNO_3 was added. These new tubes were used for Inductively Coupled Plasma (ICP) (Agilent technologies 5110, Santa Clara, CA, USA) analysis to evaluate the ion release of B (λ=249.772 nm), Si (λ=251.611 nm), Ca (λ=317.933 nm), P (λ=213.618 nm), Mg (λ=285.213 nm), K (λ=766.491 nm), Fe (λ=234.350 nm) and Na (λ=588.995 nm). The results of the measurement are reported as mean ± SD.

6.8 SEM and EDS analysis

Field-Emission Scanning Electron Microscopy (SEM) (FESEM-EDS SUPRATM 40, Zeiss) equipped with Energy Dispersive X-ray Spectroscopy (EDS) was performed before and after (time point 1 week) the *in vitro* dissolution test for the morphological and compositional characterization of the samples.

For each scaffold composition, the external surface and cross-section were studied. The samples were prepared at Tampere University and analyzed in Politecnico di Torino. For analyzing the cross section, scaffolds were first put in Eppendorf tubes and immersed in EpoFix resin (EpoFix Kit, Struers Inc., Cleveland, OH 44145 USA). Once the resin was dry, a polishing machine (Struers Inc.) was used to expose the cross-section. For the analysis, samples were fixed on aluminum stubs with a conductive adhesive and metalized with Pt.

6.9 Calorimetric and magnetic tests

The ability of the samples to release heat was investigated in Politecnico di Torino by means of a magnetic induction furnace, Egma 6 (Felmi S.r.l) using 3 kW. Samples were placed in a tube and immersed in 2 ml of distilled water; the tube was covered with a thermal insulator to reduce the heat dispersion toward the environment. The temperature evaluation was performed by a digital thermocouple (Datalogger Tersid S.p.A), evaluating the temperature difference at fixed time intervals (1, 2.5, 5 and 10 min). Samples' heating capacity was studied before and after 7 days immersion in SBF. Two measurements per condition were conducted and samples were studied in duplicate. The results are reported as mean ± SD.

Magnetic properties were investigated in Politecnico di Torino with a DC magnetometer/AC susceptometer (Lakeshore 7225) equipped with a Cryogen-Freemagnet at room temperature in quasi static condition, using a magnetic field up to 50 kA/m (low field) useful for clinical applications.

6.10 Cell analysis

To understand the impact of the SPIONS on cell viability and proliferation, cell tests, such as Live and Dead assay, were performed on human adipose stem cells (hADSCs). The cells were collected from adipose tissue samples (Ethics Committee of the Wellbeing services county of Pirkanmaa, Tampere, Finland (R15161)) and isolated as indicated in previous studies [2]. The cells used in this study were at passages P3-P5. All the cell analysis were performed in Arvo building, Kauppi Campus (Tampere, Finland).

6.10.1 Cell culture

Following a procedure similar to previous studies [3], the hADSCs were defrosted and cultured in a T-75 polystyrene flask (Cellstar® 75 cm^2 Flask, Greiner bio-one, Frickenhausen, Germany), which contained a culture medium (CM) composed of MEM Alpha Medium (MEM Alpha Medium (1X), Minimum Essential Medium, Gibco, Thermo Fisher) without nucleosides and enriched with 5% Human Serum (HS; EU Eligible, Type AB Male, Serana, Pessin, Germany) and 1% antibiotics Penicillin/Streptomycin (P/S) (Gibco, Thermo Fisher, Life Technology Corporation, Grand Island, New York, USA).

The cells were cultured in an incubator (Thermo Scientific forma steri-cycle i160 CO_2) at 37 °C with controlled atmosphere parameters (air with 5% CO_2, controlled humidity) until they reached 80% confluence. The culture medium was changed every 2-3 days. Before every experiment, the cells were detached from the flask using 3 ml of trypsin (TryPLE™ Select (1X), Gibco, Thermo Fisher) and resuspended in culture medium.

6.10.2 Scaffold preincubation

Before the start of each cell test, scaffolds were first sterilized and then preincubated in culture medium. The sterilization was performed in a furnace at 200 °C for 3 hours, where each scaffold was placed and stored in a glass jar. For the preincubation, culture medium composed of α-MEM, 5% HS and 1 % P/S was added in each jar in the correct amount of 1 ml of CM every 10 mg of bioactive glass. The preincubation of the samples lasted 24 hours, after which 1 ml of CM was collected from each jar for ICP analysis. Samples containing only CM were prepared as a control. Preincubation solutions and controls were stored at -20 °C and then diluted 10 times in distilled water before ICP. The results of the measurements are graphically reported as mean ± SD.

6.10.3 Live and Dead assay

Live and Dead assay was performed to investigate the viability of the cells when put in direct contact and around the different scaffolds.

The hADSCs (passage P4), suspended in culture medium (α-MEM, 5% HS and 1 % P/S) with a density of 1100 cells/cm^2, were seeded into 48-well plates (ThermoFisher Scientific, Waltham, MA, USA), placing 1 ml of suspension for each well. Here, cells were cultured together with the preincubated scaffolds. Three samples per condition at three time points (day 1, day 3, day 7) were studied. For each time point, three wells of positive control were added to the analysis, consisting of cells in culture medium seeded at the bottom of the plate without scaffolds. Culture medium was refreshed at days 2 and 6.

At each time point and every time culture medium was refreshed, 1 ml of CM was collected from each well, stored at -20 °C and then diluted 10 times in distilled water for ICP analysis. At days 1, 3 and 7, after CM collection, scaffolds and positive controls were rinsed with Dulbecco's Phosphate Buffered Saline (DPBS) (Gibco, Life Technologies, Carlsbad, CA, USA) heated at 37 °C and then treated by placing 500 µl of staining solution in each well. The staining solution was prepared by adding 1.25 µl of each staining from the Live & Dead Kit (Live/Dead Cell Double Staining Kit, SIGMA-ALDRICH, 04511) to 10 ml of DPBS heated at 37 °C. Calcein-AM stained the live cells in green, while the dead cells were stained in red with Ethidium homodimer-1 (EthD-1). The samples were incubated with the staining solution for 45 minutes at 37 °C and then washed again with DPBS. At this point, three areas per sample were observed and captured with a fluorescence microscope (IX51, Olympus, Tokyo, Japan). All the images were processed with the software ImageJ2 1.54 (National Institutes of Health, USA).

6.10.4 Cell observation

Given the results from Live and Dead, an additional cell analysis was performed to verify how cell proliferation changed with a higher cell seeding density.

Scaffolds were preincubated following the same procedure as previously described and cultivated with cells considering a seeding cell density of 15000 cells in 1 ml of culture medium (α-MEM, 5% HS and 1 % P/S). Cell observation was performed at three time points (d1, d2, d7) with an optical microscope, from which pictures were acquired. Three samples per condition were studied, with the addition of the positive controls, which consisted of cells cultured without the scaffolds.

REFERENCES

[1] W. Stöber, A. Fink, and E. Bohn, “Controlled growth of monodisperse silica spheres in the micron size range,” *Journal of Colloid and Interface Science*, vol. 26, no. 1, pp. 62–69, Jan. 1968, doi: 10.1016/0021-9797(68)90272-5.

[2] L. Kyllönen *et al.*, “Effects of different serum conditions on osteogenic differentiation of human adipose stem cells in vitro,” *Stem Cell Res Ther*, vol. 4, no. 1, p. 17, Feb. 2013, doi: 10.1186/scrt165.

[3] V. A. Gobbo, A. Houaoui, K. Tajik, V. P. Hytönen, S. Miettinen, and J. Massera, “Concomitant silanization and controlled fibronectin adsorption on S53P4 bioactive glass enhances human adipose stem cells spreading and differentiation,” *Applied Surface Science Advances*, vol. 23, p. 100635, Sep. 2024, doi: 10.1016/j.apsadv.2024.100635.

7. RESULTS

7.1 SPIONS synthetization

Produced SPIONS via the co-precipitation method were analyzed using TEM to assess their shape and size. Figure 34 and Figure 35 present the TEM images of SPIONS as a dry powder and in liquid solution, respectively. It can be seen that the produced SPIONS have a spherical shape, with a diameter of approximately (12.86 ± 1.72) nm. Dry SPIONS (Figure 34) tend to aggregate, forming agglomerates, while in liquid (Figure *35*) the dispersion results more uniform.

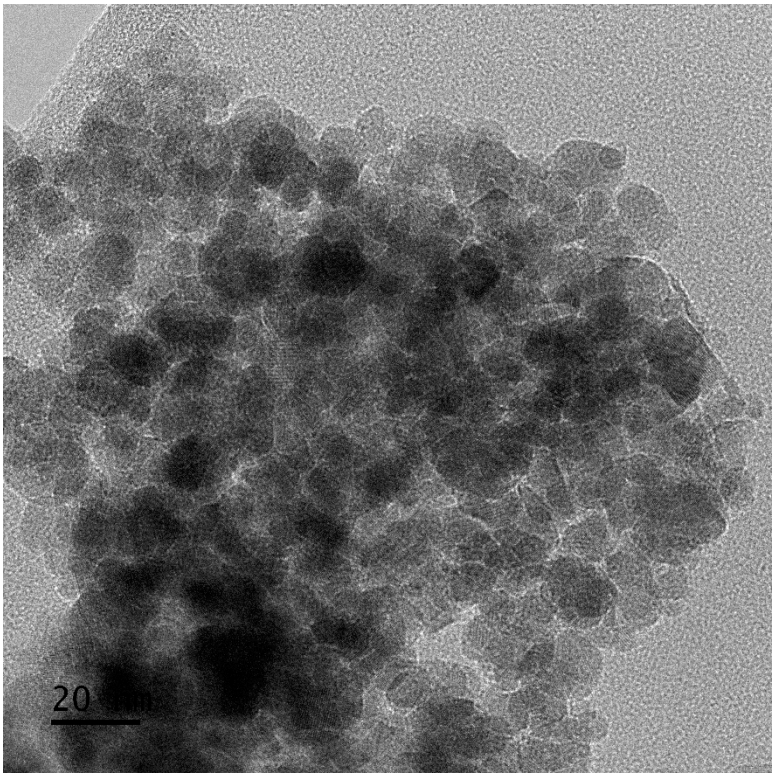

Figure 34. TEM image of SPIONS as a dry powder.

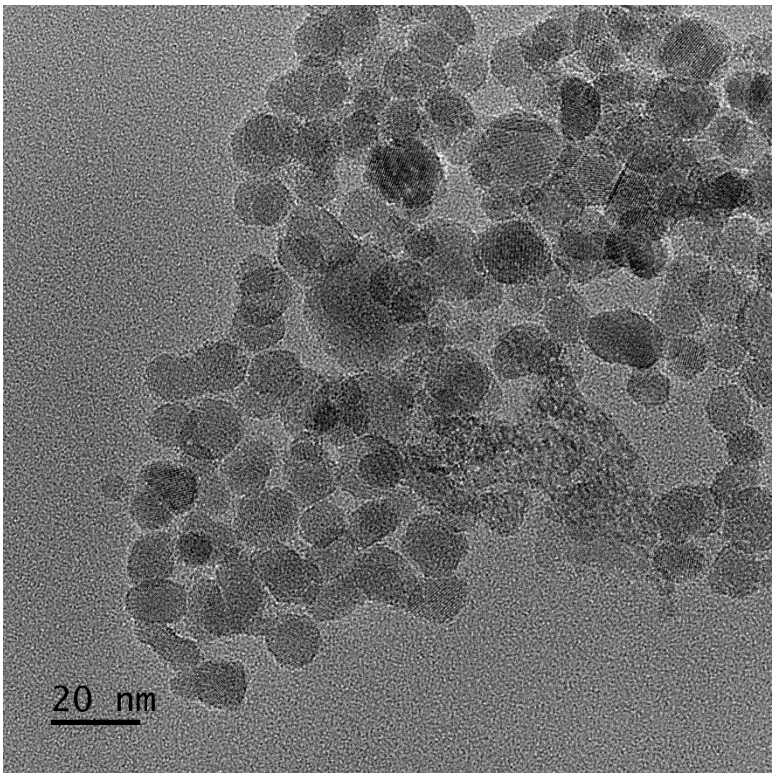

Figure 35. TEM image of SPIONS in liquid solution.

7.2 Rheology testing of inks and Pluronic solutions

As the aim was to produce SPIONS-containing scaffolds, via 3D prototyping, it is important to assess the impact of SPIONS incorporation on the ink rheology, both as dry and in a liquid. The rheology test aimed at understanding how the ink reacted when the shear rate increased, looking at the variations in shear stress and viscosity. The test was performed at the same temperature as the 3D printing is conducted (25 °C), in order to have the same conditions.

Figure *36* illustrates the viscosity of the inks as a function of the shear rate, while Figure *37* presents the shear stress of the inks as a function of shear rate. In both Figure 36 and Figure 37, the graphs are presented until a shear rate of 500 s^{-1} is reached. At higher shear rate values, the materials did not flow correctly anymore, leaving some empty spots under the rotating plates. Indeed, when the experiment is coming to an end and the plates are rotating faster, inks and Pluronic solutions might slip some material outside of the plates, leading to a non-uniform plate-material contact. After each test, a visual inspection confirmed that the material was accumulated at the borders of the plates and it was very thin, or not present anymore, in the central part.

The presence of error bars in all the graphs didn't allow a precise individuation and interpretation of the curves. Therefore, error bars are only reported in one curve in both Figure 36 and Figure 37 to verify the presence of a significative difference among the results.

Considering other studies on ceramic inks and robocasting [1], [2], [3], the shear rate range, to enable 3D printing, is considered to be between 10 s^{-1} and 300 s^{-1}, with the viscosity in the range between 10 Pa·s and 1000 Pa·s.

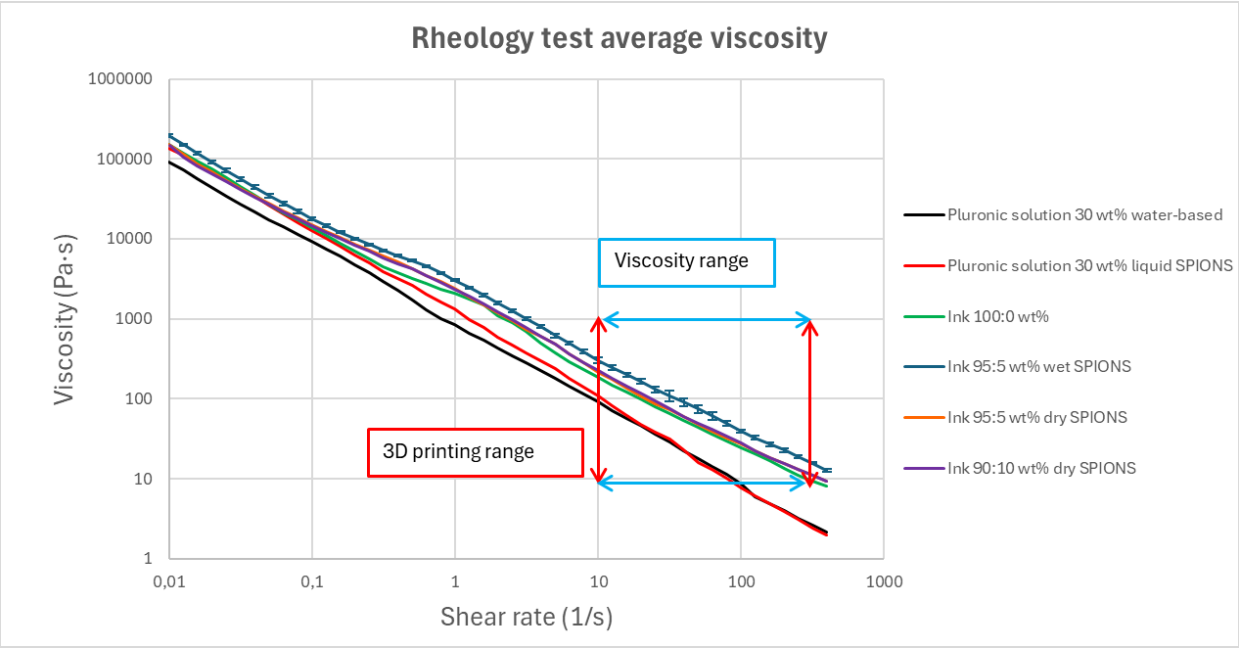

Figure 36. Average viscosity of the different fluids as a function of the shear rate.

All the viscosity graphs in Figure 36 show a clear decrease in viscosity when the shear rate increases. Regarding the inks, the curves almost overlap during the whole test, except for the ink with the composition 95:5 wt% glass/SPIONS prepared in wet conditions which has an average viscosity slightly above the others. The two Pluronic solutions show a lower average viscosity compared to the inks.

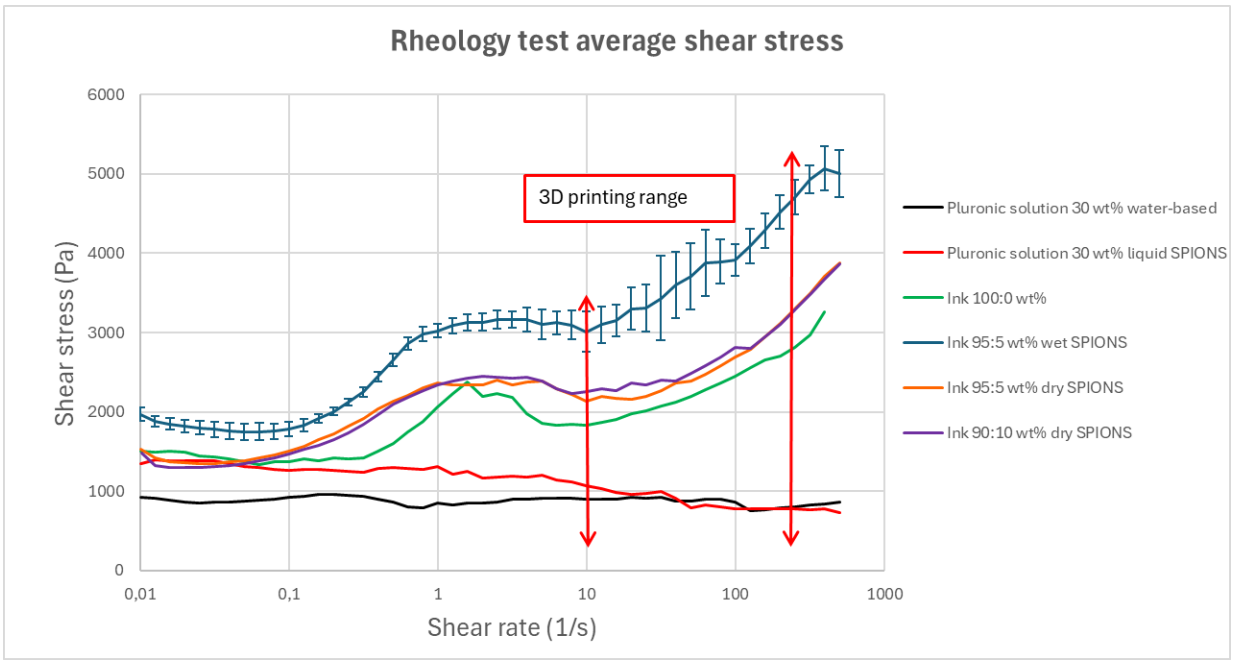

Figure 37. Average shear stress of the different fluids as a function of the shear rate.

The two Pluronic solutions in Figure *37* exhibit an almost horizontal line, without significant changes of the shear stress respect to the increasing of the shear rate. From Figure *37*, it is possible to see that in the different ink compositions the average shear stress is increasing with the shear rate. In both types of inks, with or without SPIONS, the pattern in the graphs is quite similar, with the inks

containing SPIONS showing a higher average shear stress than the one without. All the inks present a yield stress, ranging from 1493 Pa to 1970 Pa.

7.3 Scaffold production

Scaffolds of different glass/SPIONS compositions were produced through robocasting technique. Figure 38 shows the photograph of the produced scaffolds.

Figure 38. Photograph of the produced scaffolds. From left to right: 100:0 wt%, 95:5 wt% wet, 95:5 wt% dry, 90:10 wt% dry.

Scaffolds with a visible porous structure were successfully obtained for all the compositions, as shown in Figure *38*. However, some of the samples containing SPIONS required continuous pressure adjustments during printing, resulting in increased bulkiness of the structure. Consequently, obtaining a well-defined and reproducible porous structure was not always possible.

In particular, avoiding the formation of big SPIONS powder aggregates was a fundamental requirement for smooth printing in 95:5 wt% dry and 90:10 wt% dry compositions. To ensure this, weighed SPIONS were well crushed in a mortar alone and then together with glass powder during the ink preparation. Printing with the ink 95:5 wt% dry proceed without significant issues. However, the deposition of the ink 90:10 wt% dry encountered some difficulties, such as the lack of complete homogeneity in the fluid, with some parts which were watery and couldn't maintain perfectly the given shape, and other parts more viscous which required a higher pressure to flow through the nozzle.

On the other hand, the scaffolds produced with SPIONS in liquid solution were printed with less complications, showing that, in the case of the composition 95:5 wt%, the introduction of the SPIONS as a dry powder or as a liquid solution didn't change the overall printability process.

7.4 Magnetic properties and heating capacity

To verify that the scaffolds containing SPIONS were magnetic after the printing process, each type of sample was placed in close proximity to a magnet. Figure 39 shows that, except for the composition 100:0 wt%, all the other scaffold types attached to the magnet.

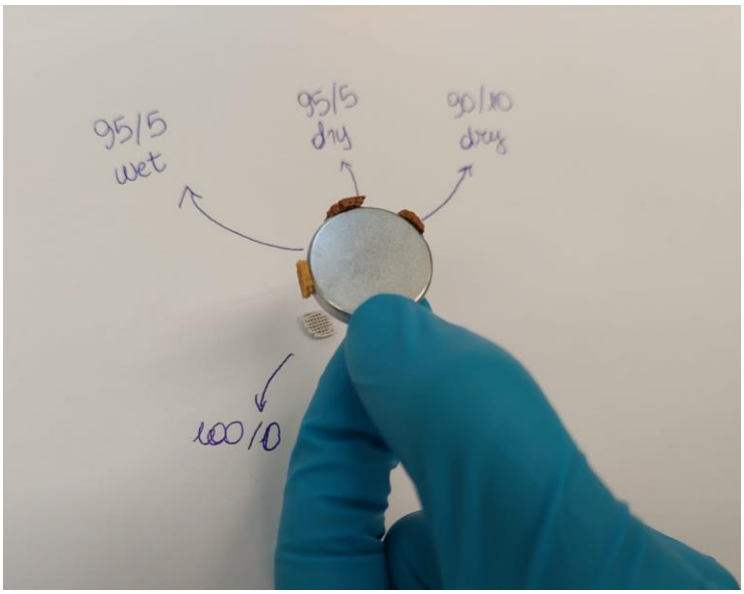

Figure 39. Photograph of the produced scaffolds showing their interaction with a magnet.

The magnetic properties of the scaffolds were further investigated to verify the presence of superparamagnetic behavior by measuring their magnetization under an alternating magnetic field. Figure 40 shows the variation of magnetization M as a function of the magnetic field strength H for the three different scaffold compositions containing SPIONS. The magnetic field strength H reached values up to 50 kA/m, corresponding to the range of interest for hyperthermia clinical applications [4].

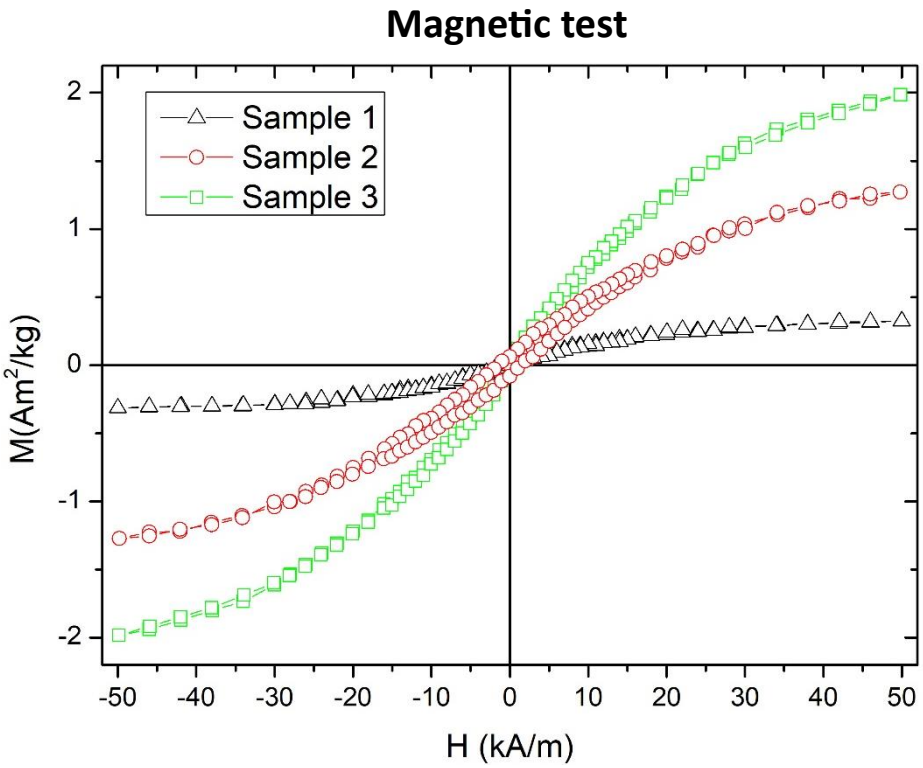

Figure 40. Magnetic test. Variation of the magnetization M as a function of the magnetic field strength H. Sample 1: 95:5 wt% wet, sample 2: 95:5 wt% dry, sample 3: 90:10 wt% dry.

In Figure 40, all the compositions exhibit a response to the alternating magnetic field. The composition 90:10 wt% dry corresponds to the one with the highest saturation magnetization, followed by 95:5 wt% dry and 95:5 wt% wet, which is the one with the lowest saturation magnetization. For all the compositions the behavior can be considered superparamagnetic, since the residual magnetization and the coercivity are close to zero.

In addition, a calorimetric test was performed to verify the heating capacity of the scaffolds when exposed to an external alternating magnetic field before and after 7 days immersion in SBF. The variation in temperature as a function of time of the different scaffold compositions containing SPIONS is presented before the immersion in SBF in Figure 41, and after 7 days immersion in SBF in Figure 42.

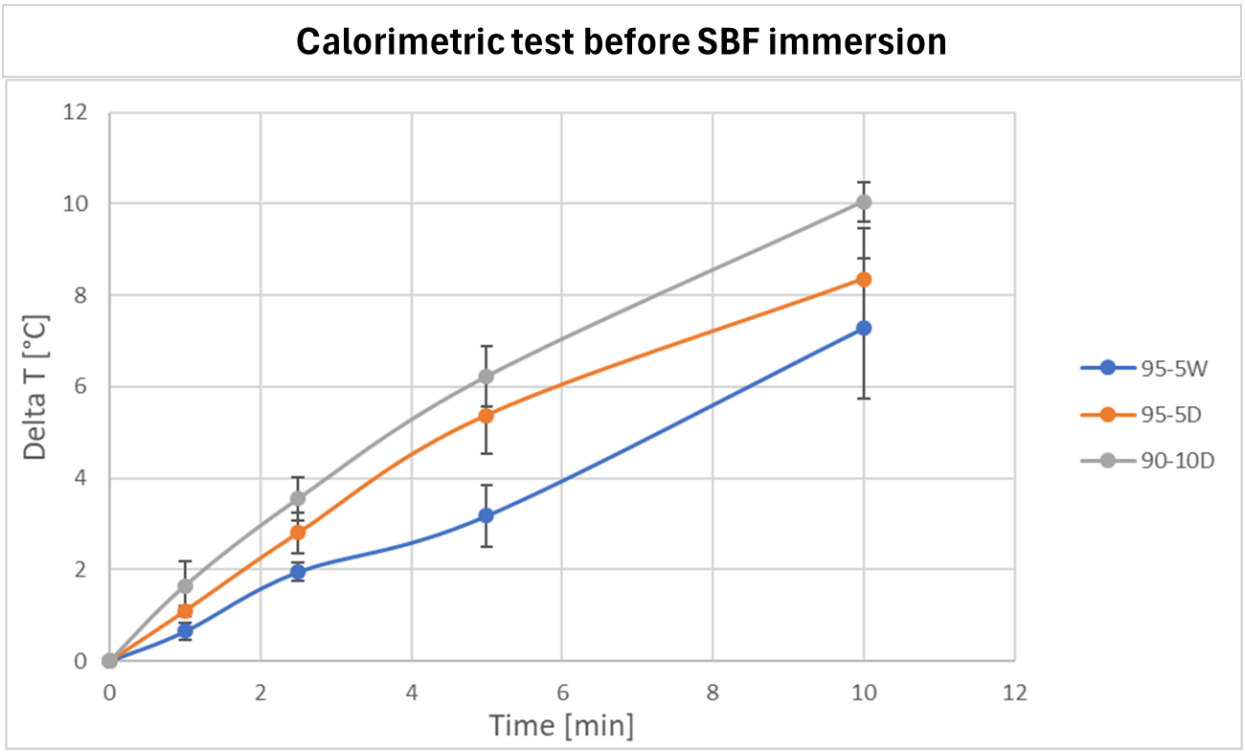

Figure 41. Calorimetric test. Variation of temperature as a function of time for the different BAG/SPIONS scaffold compositions before immersion in SBF.

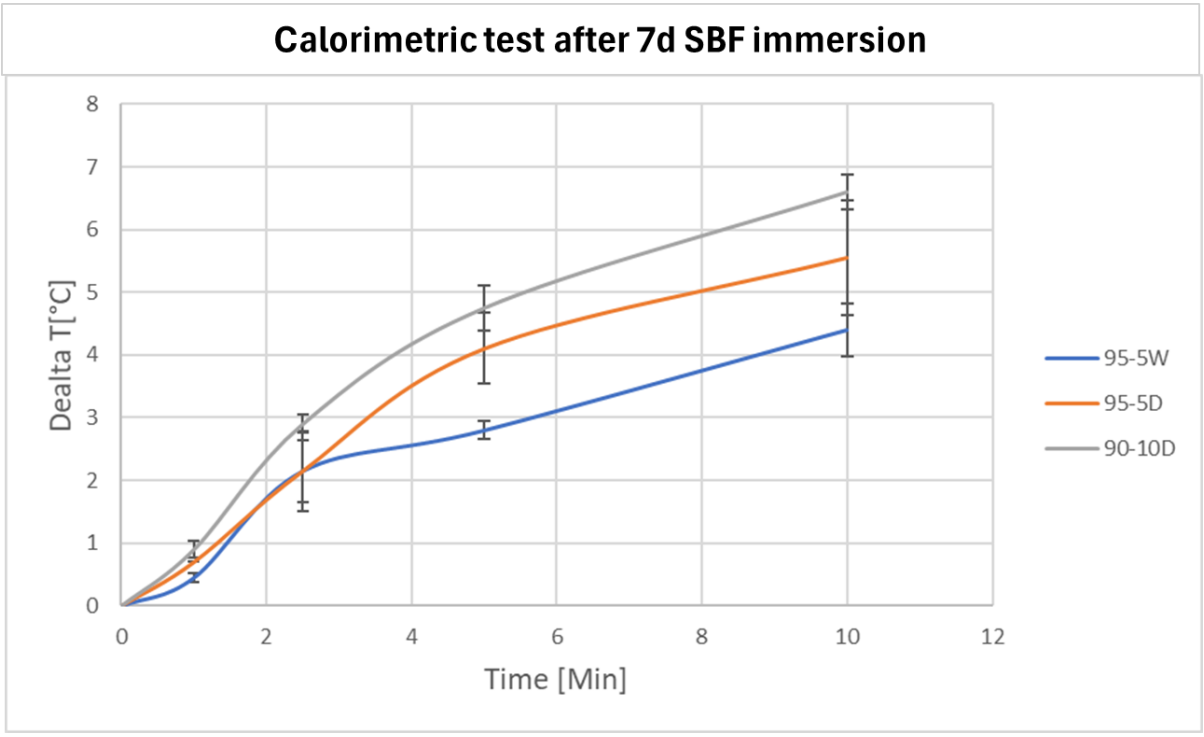

Figure 42. Calorimetric test. Variation of temperature as a function of time for the different BAG/SPIONS scaffold compositions after 7 days immersion in SBF.

In Figure 41, the composition 90:10 wt% dry exhibits the highest average temperature variation, increasing almost linearly and reaching a ΔT equal to 10 °C after 10 minutes under the magnetic field. The graph of composition 95:5 wt% dry follows a very similar trend, achieving comparable ΔT values, as indicated by the overlapping of the error bars at different time points. On the other hand, the temperature variation in the 95:5 wt% wet scaffolds is lower compared to the other two curves. As shown in Figure 42, similar results are obtained after 7 days of immersion in SBF, even though the temperatures reach lower values compared to the situation before the immersion.

7.5 Mechanical testing

The mechanical properties of the scaffolds were analyzed in compression through a mechanical test. From each scaffold tested, a graph of compressive stress as a function of compressive strain was extracted and used to calculate the values of Young's Modulus and fracture strength, as shown in Figure 43, taken as an example.

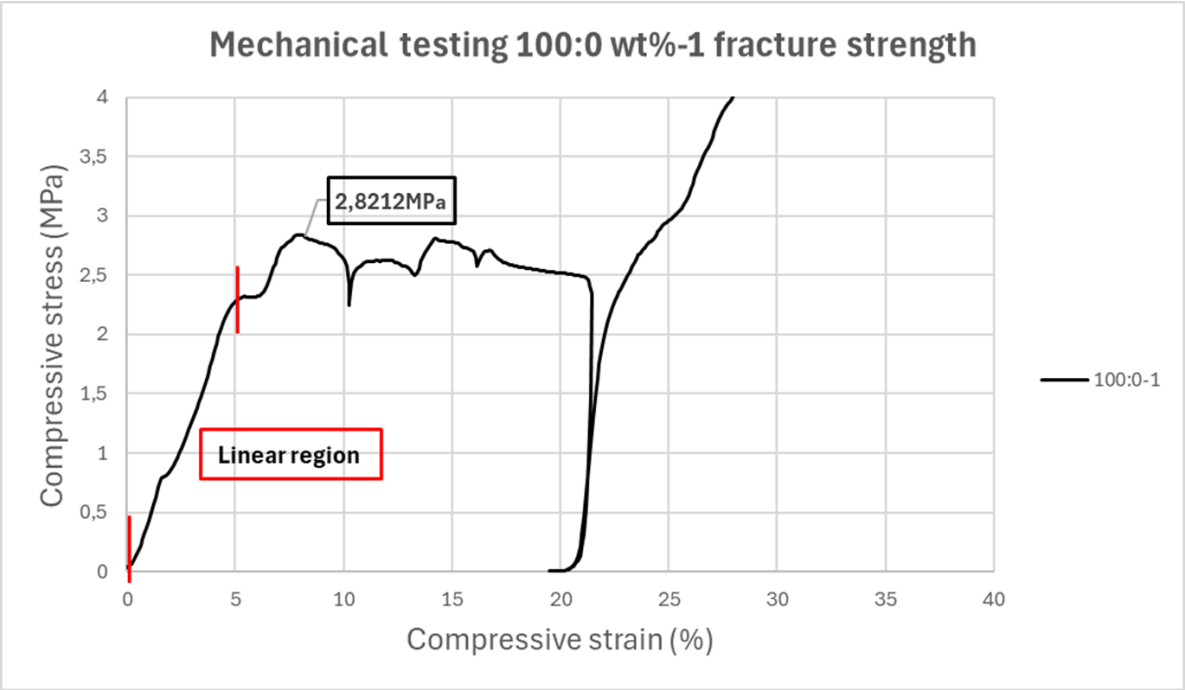

Figure 43. Example of compressive stress as a function of compressive strain graph obtained from the mechanical test.

The graph shows an initial linear part and subsequently a certain number of downward peaks. The linear part corresponds to the elastic region, where the Young's Modulus can be calculated as the slope of the curve using a linear fitting plot. The presence of multiple peaks directed downwards shows that the scaffold broke in many steps and not all at once, with a pattern confirmed by other studies about compressive tests on porous scaffolds [5], [6], [7]. After each breakage, the graph shows an increase in compressive stress, especially in the final part of the test. This aspect is due to the fact that when the pores collapse under loading, the structure of the scaffold densifies, becoming able to resist higher values of compressive stress and leading to a sharp increase in the graph [8]. Therefore, the actual value of compressive strength was considered as the peak of stress before the first break of the scaffold, when the structure is not yet broken and densified, as reported in Figure 43.

For each type of composition, the average Young's Modulus and the average fracture strength were calculated and reported in Figure 44 and Figure 45, respectively, with their standard deviation. In some cases, especially for the composition 100:0 wt%, the values of standard deviation resulted quite high. It needs to be considered that only 5 samples were tested for each composition, therefore some differences in the results of the test could lead to a large standard deviation.

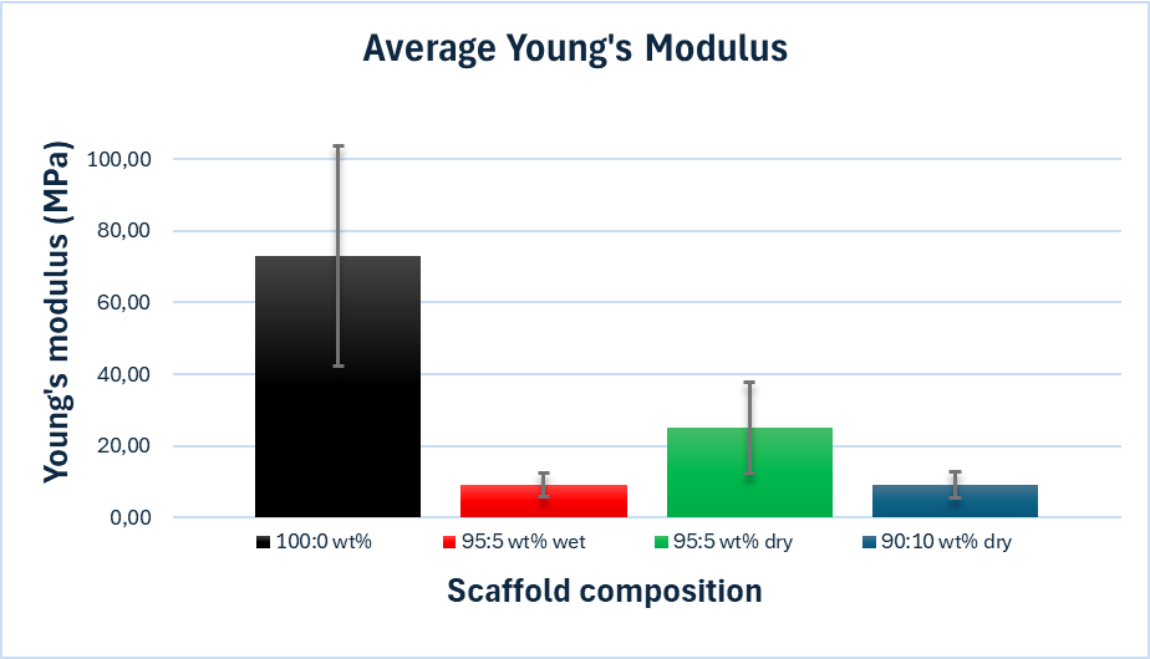

Figure 44 Average Young's Modulus and its standard deviation of the different scaffold compositions.

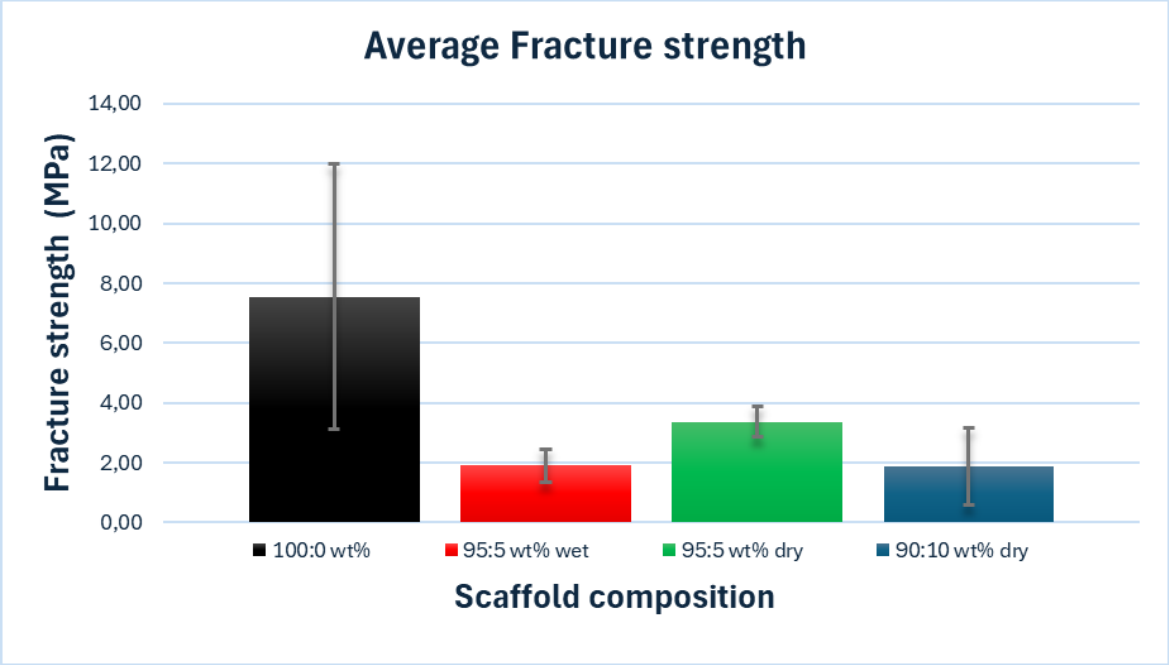

Figure 45. Average fracture strength and its standard deviation of the different scaffold compositions.

Among the different scaffold types, the composition 100:0 wt% shows the highest average mechanical properties, consistent with values reported for trabecular bone, as reported in Table 6. In contrast, the mechanical properties are generally low in the scaffolds containing SPIONS, among which the composition 95:5 wt% dry shows the highest average Young's Modulus and average fracture strength. Comparable results are obtained for the compositions 95:5 wt% wet and 90:10 wt% dry.

Table 6. Mechanical properties of trabecular and cortical bone in comparison with the tested samples [9].

Material	**Young's Modulus (MPa)**	**Compressive strength (MPa)**
100:0 wt%	72.77 ± 30.70	7.55 ± 4.42
95:5 wt% wet	9.00 ± 3.28	1.91 ± 0.55
95:5 wt% dry	25.13 ± 12.70	3.37 ± 0.50
90:10 wt% dry	9.01 ± 3.64	1.88 ± 1.29
Trabecular bone	50-500	0.1-16
Cortical bone	7000-30000	130-200

7.6 In vitro dissolution test

The dissolution properties were studied in order to investigate the bioactivity of the scaffolds, meaning the ability of the material to release ions into the solution which can precipitate and form a hydroxyapatite-like reactive layer. Samples were immersed in SBF under dynamic conditions to enable fluid movement and better liquid homogeneity, especially after ions are being released.

Figure 46 shows the average pH of the solution as a function of the incubation time calculated on 3 samples per type, with the standard deviations represented as error bars.

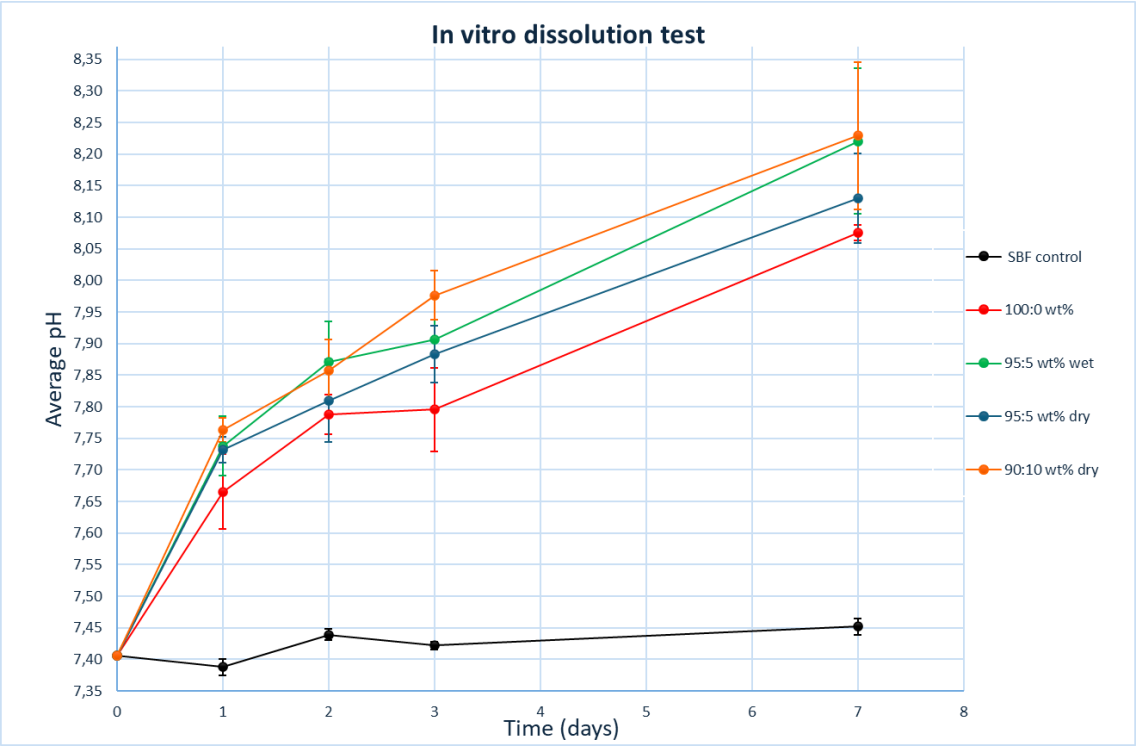

Figure 46. Average pH of the solution and its standard deviation at different time points.

SBF control shows a quite constant pH during the entire experiment, ensuring in this way the stability of the solution.

For the other samples, it is possible to see a similar trend of increase in the pH, with higher average values for the scaffolds containing SPIONS, especially for the composition 90:10 wt% dry. Therefore, the more SPIONS are present, the higher the pH is. This fact needs to be taken into consideration when scaffolds dissolve in the presence of cells, because of the development of a possible pH-dependent cytotoxicity [10]. However, by looking at the error bars at the different time points, the pH values of the various compositions partially overlap, so this difference is not so significant.

ICP-OES analysis was performed to assess the amount of ions present in the solution post-immersion. From the results of the analysis, sodium concentration was over the upper detection limit (440 ppm) in all the analyzed solutions, therefore the graph is not reported. On the other hand, iron release was under the lower detection limit (0.1 ppm), so its graph is not represented as well.

Figure 47 shows the silicon and boron ions concentrations, as a function of time, for the solutions containing the different scaffolds and the SBF control.

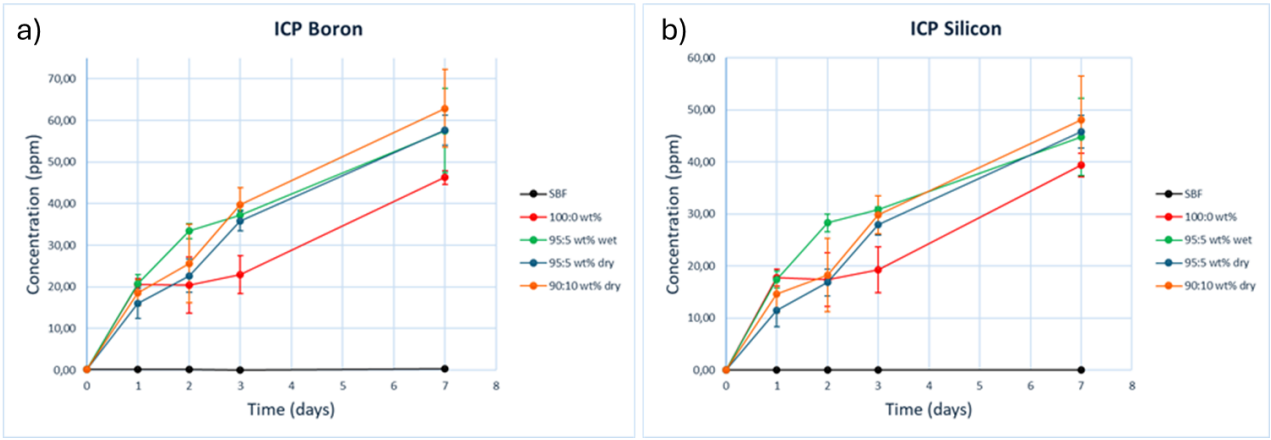

Figure 47. Release profiles of boron (a) and silicon (b) for 7 days in vitro dissolution test.

The release profiles of silicon and boron into the solutions give information about the general dissolution of the glass structure, as they are the network glass formers in a borosilicate glass, such as 1393 B20 [11].

SBF control is stable at 0 ppm for all the experiment duration, as silicon and boron are not contained in the SBF solution.

For all conditions, the silicon and boron contents increase in SBF with increasing immersion time. While a plateau is seen in the ions concentration between day 1 and 3 for the pure glass scaffolds, such plateau is absent from all the other conditions. In general it appears that the ion release from the 100:0 wt% scaffolds remained lower than the ion released from all SPIONS-containing scaffolds. Given the accuracy of the measurement, it seems that the dissolution of the scaffolds increases when SPIONS are introduced, but the amount of SPIONS and its state (dry vs wet) does not significantly impact the ion release.

The release profiles of calcium and phosphorus, represented in Figure 48, can give some information regarding the bioactivity, meaning the potential precipitation of a CaP reactive layer on the surface of the scaffolds.

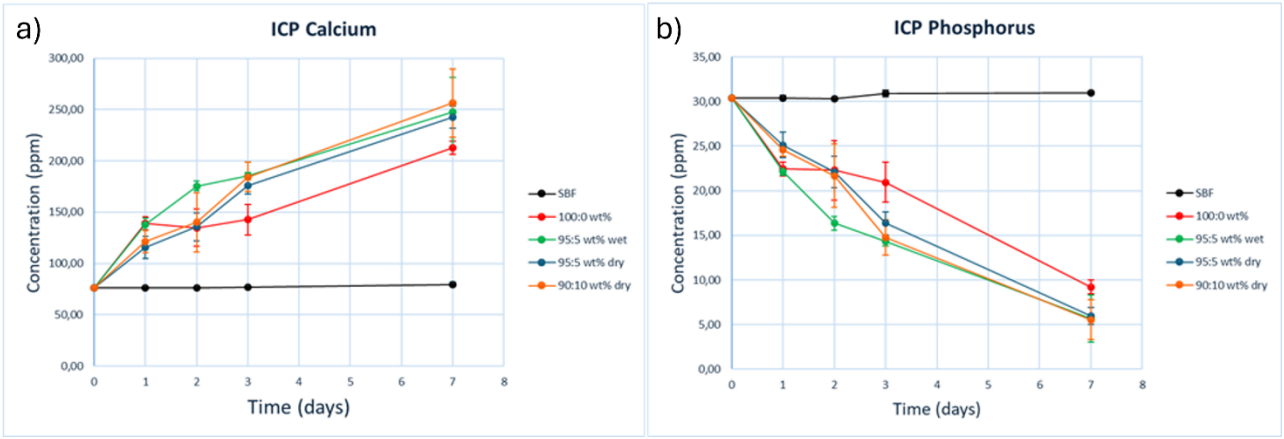

Figure 48. Release profiles of calcium (a) and phosphorus (b) for 7 days in vitro dissolution test.

SBF control shows quite stable profiles, with a non-zero concentration of calcium and phosphorus since the SBF solution contains these elements. However, it is important to note that both calcium and phosphorus remain constant throughout the testing period, confirming that the solution was stable.

For the solutions in contact with samples, calcium concentration is increasing, while phosphorus concentration is decreasing, indicating a phosphorous consumption. The patterns of calcium and phosphorus concentrations are coherent between each other and with the ones of silicon and boron in Figure 47: the composition 100:0 wt% shows a stabilization in the profiles between days 1 and 3, the two compositions 95:5 wt% dry and 90:10 wt% dry exhibit similar profiles, while 95:5 wt% wet distinguishes itself with a different trend only during the days 1 and 3.

7.7 Surface analysis

To investigate the morphology and composition of the scaffolds' surface, before and after 1 week immersion in SBF, SEM and EDS analyses were performed.

Figure 49 shows the SEM images acquired of all the scaffold compositions, before and after the in vitro dissolution test, while Figure 50 shows specifically the surface of the scaffold with composition 100:0 wt% before the immersion test at a lower magnification.

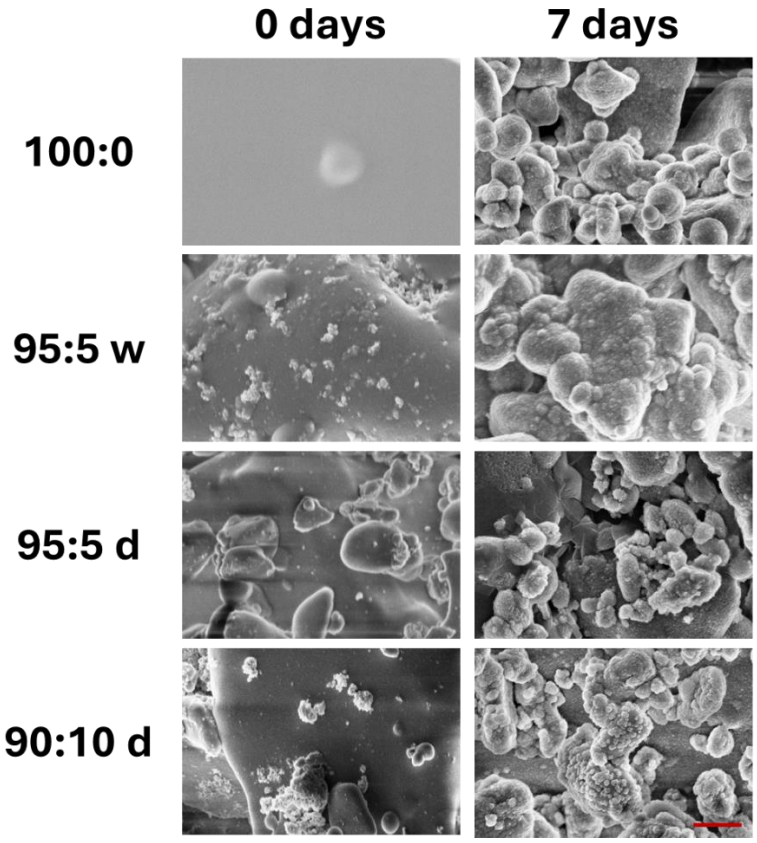

Figure 49. SEM images acquired before and after 7 days immersion in SBF. Magnification 20.00 KX. Scale bar 1 µm.

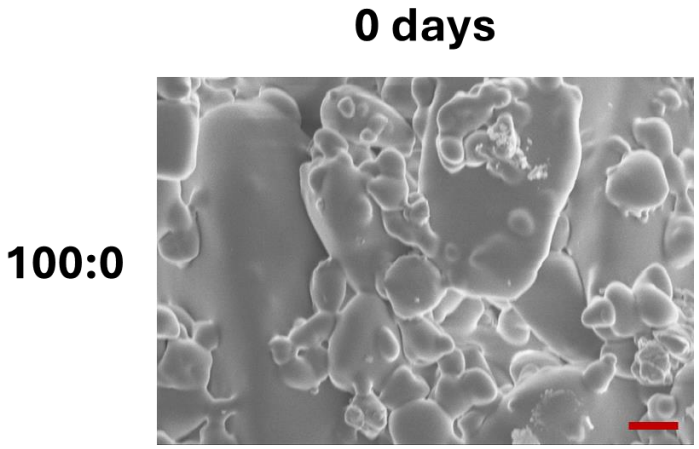

Figure 50. Image at a lower magnification (5.00 KX) of the surface for the composition 100:0 wt%. Scale bar 2 µm.

The surface of the sample with composition 100:0 wt% shows the formation of necks between the glass particles, representing a good but not perfect densification.

From Figure 49, the distribution of the SPIONS appears different depending on the scaffold composition and on the way SPIONS were introduced. In particular, in the compositions 95:5 wt% wet and 90:10 wt% dry SPIONS form agglomerates of the size of 100-200 nm, while with 95:5 wt% dry the distribution appears more homogeneous.

After 1 week of immersion in SBF, all the scaffold types show the formation of nodules which partially cover the surface, regardless of SPIONS presence.

The atomic percentage composition of different elements at the scaffold surface was analyzed using EDS before and after SBF immersion, as reported in Table 7. In addition, Table 7 presents the Ca/P ratios calculated for each condition.

Table 7. Element atomic% composition and Ca/P ratio for each type of scaffold, before and after 7 days in vitro dissolution test.

	100:0 wt%		**95:5 wt% wet**		**95:5 wt% dry**		**90:10 wt% dry**	
Elements	0d	7d	0d	7d	0d	7d	0d	7d
Na	15.8±1.7	8.9±3.2	9.6±0.2	7.1±2.0	17.0±4.9	5.8±3.4	15.3±2.3	8.2±0.6
Mg	9.6±0.5	7.0±2.6	6.9±0.5	5.6±0.3	9.0±1.4	4.8±1.4	8.4±1.1	7.4±1.0
Si	50.5±0.7	46.9±4.8	44.6±0.2	55.5±8.6	48.6±0.9	53.0±2.4	45.7±1.0	49.6±4.2
P	2.7±0.6	10.2±6.2	2.6±0.4	6.4±2.2	3.0±0.4	5.1±1.1	2.9±0.5	4.4±1.1
K	7.4±1.0	5.9±2.3	11.5±0.3	3.8±2.0	7.4±1.7	5.1±0.5	7.8±0.6	6.6±2.6
Ca	14.1±1.6	22.3±5.8	22.1±0.2	15.5±3.3	13.8±4.9	17.8±2.9	14.3±2.8	16.4±3.1
Fe	0.0±0.0	0.0±0.0	2.7±0.1	6.1±6.7	1.2±0.8	8.5±2.3	5.7±1.6	7.4±1.0
Ca/P ratio	5.4±1.4	2.7±0.9	8.7±1.2	2.8±1.4	4.8±2.2	3.6±0.4	5.2±1.7	4.2±1.7

In general, all the scaffold compositions show higher Na and lower Ca atomic percentages, compared to the nominal glass composition of the bioactive glass 1393 B20.

The Ca/P ratios calculated after SBF immersion are lower for all the scaffold compositions, compared to the pre-immersion values.

7.8 Cell analysis

The impact of SPIONS on cells was assessed through cell tests on viability (Live and Dead assay).

Figure 51 shows fluorescence microscope images obtained from the Live and Dead assay. The images compare hADSCs cultured alone (positive control) with those cultured in the presence of the scaffolds, using the composition 95:5 wt% wet as an illustrative example.

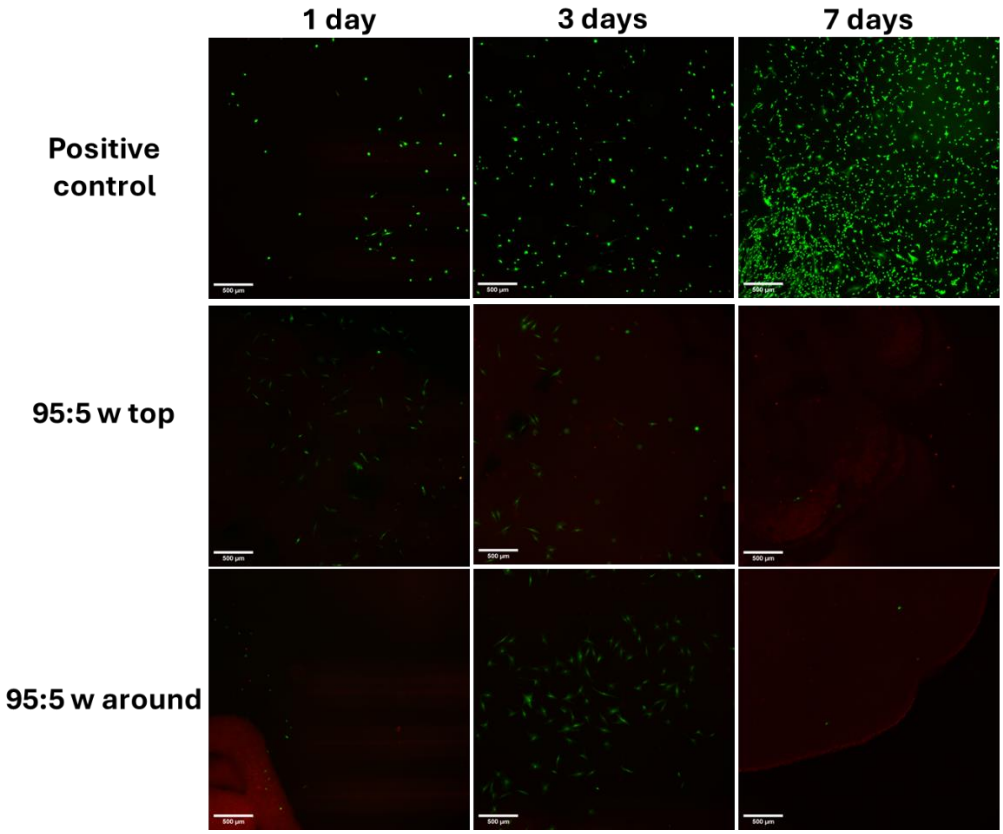

Figure 51. Live and Dead assay images at 3 time points (d1, d3, d7) for the positive control and the composition 95:5 wt% wet. Green-viable cells, red-necrotic cells. Scale bar 500 µm.

Cell viability is generally low both around and on the top of the scaffold, although viable cells are relatively more present around the sample at day 3. Moreover, the number of alive cells decreases significantly between day 3 and day 7, with almost no alive cells observed on day 7.

Nevertheless, it needs to be noted that the positive control generally exhibited a quite poor cell proliferation throughout the experiment, not reaching full confluence by day 7.

The cumulative ion release into CM during cell culture with the scaffolds was investigated by ICP analysis, as shown in Figure 52 and Figure 53.

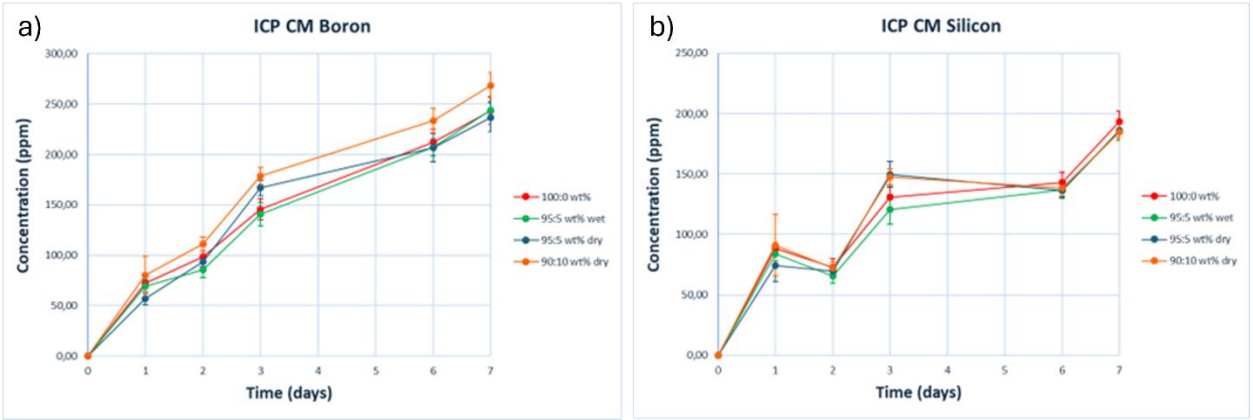

Figure 52. Cumulative ion release of boron (a) and silicon (b) into culture medium for 7 days cell culture.

The release profiles of boron and silicon in Figure 52 generally show an increase in their concentration into the solution, with higher values of ion concentration compared to the ones detected during the dissolution in SBF (Figure 47).

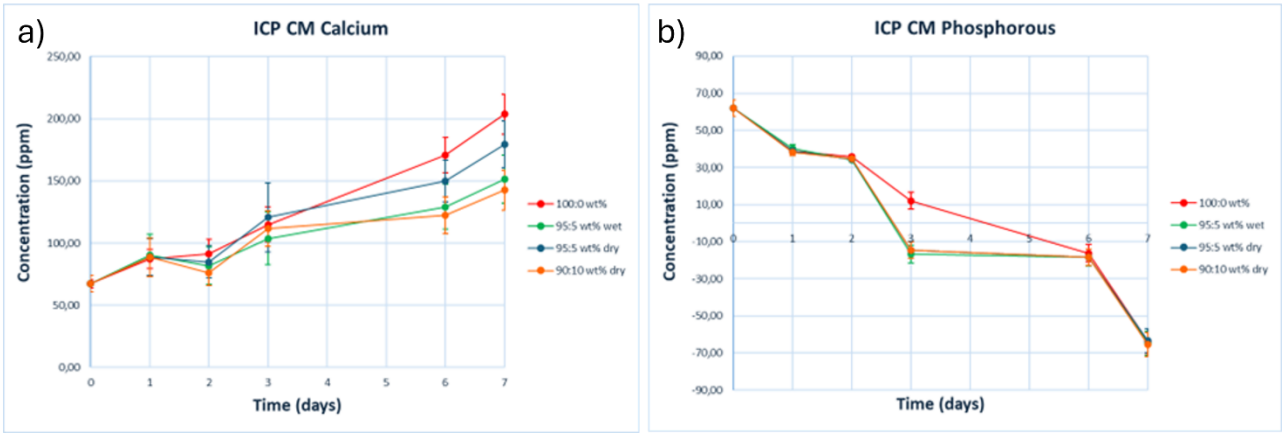

Figure 53. Cumulative ion release of calcium (a) and phosphorous (b) into culture medium for 7 days cell culture.

Similarly to calcium and phosphate release in SBF (Figure 48), calcium release in CM increases and phosphate release decreases, indicating phosphorous consumption (Figure 53).

In order to investigate the reasons for a too low cell proliferation during the Live and Dead assay, an additional cell observation was performed using a higher cell seeding density. Figure 54 shows an optical microscope image acquired on day 7 of cell culture for the composition 95:5 wt% wet. Compared to the images from the Live and Dead assay (Figure 51) where almost no cells are detected at this time point, Figure 54 reveals the presence of numerous cells. However, these cells are predominantly located far from the scaffold, where they also appear quite spread. In the area adjacent to the scaffold cells are present in less quantity and mostly with a round shape.

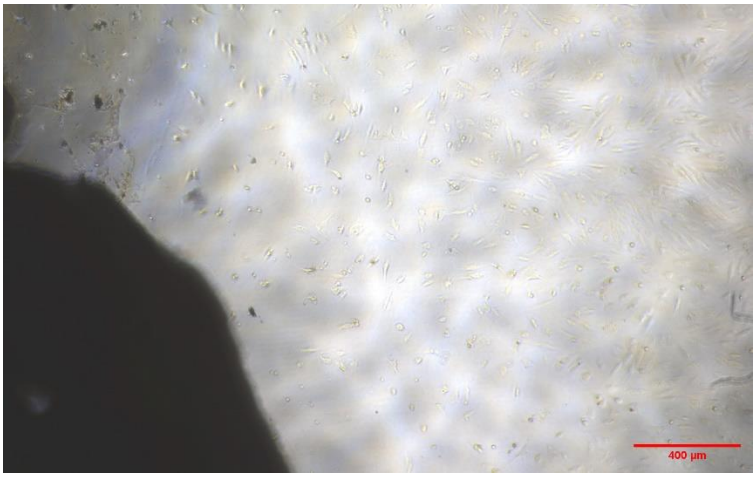

Figure 54. Optical microscope image for the composition 95:5 wt% wet. Scale bar 400 µm.

Given the Live and Dead results, the next step will be to optimize the cells density and ensure proper proliferation of the cells in the control wells. Subsequently, cell proliferation using CyQUANT will be performed.

8. DISCUSSION

8.1 Material characterization

The synthesis of SPIONS was successful and led to the production of nanosized particles covered by citric acid. In particular, the measured diameter of the NPs proved to be in the right dimension-range (diameter ≤ 20 nm) for being superparamagnetic [4].

As proved in other studies [12], the presence of citric acid as a coating influences the dispersion in aqueous medium, preventing the NPs from forming aggregates. When the pH is adjusted at 10.2 after citric acid adsorption, the third carboxylic group of this organic molecule deprotonates, leaving a negative surface charge on the NPs which promotes an electrostatic repulsion and the formation of a steric barrier, providing long-term stability [13], [14]. This is not favored without the presence of an aqueous medium, thus leading to the formation of aggregates in dry SPIONS. This aspect needs to be considered and figured out, for example by crushing the powder of SPIONS, for the ink production because the magnetic properties of the final result might be altered by the presence of agglomerates [15].

From the rheological test, both Pluronic solutions and inks exhibit a shear thinning behavior, which is an important characteristic in robocasting, as it allows a correct extrusion of the fluid through the nozzle [1].

Pluronic F127 is a triblock copolymer which undergoes a reversible thermogelling process in aqueous solutions, passing from a solution to a gel-like state when the temperature overcomes the gel temperature T_g [16]. For a solution concentration of 30 wt%, it was demonstrated that T_g is around 10 °C [16], therefore the material is a gel at room temperature and behaves like a viscoplastic fluid. In this state, the fluid is composed of a cubic lattice structure of spherical micelles (PPO as a core and PEO as a shell) packed closely which can break up and flow when undergoes a sufficient stress while passing through the nozzle [16], [17]. The presence of the glass contributes to the stiffening of the fluid, therefore the average viscosity curves of the inks in Figure 36 are slightly above the ones of the two Pluronic solutions.

As proved in other studies [18], the overlapping of the average viscosity curves of Figure 36 means that the rheological properties of the inks are mostly due to the intrinsic interactions between the hydrophobic and hydrophilic segments of Pluronic chains, so the presence of a lower or higher concentration of glass and SPIONS doesn't affect significantly a change in viscosity. The ink 95:5 wt% wet might have a slightly higher viscosity than the others because of the different preparation method of the Pluronic solution combined with the presence of glass powder: the introduction of the liquid solution of SPIONS could have marginally changed the stiffness of the final Pluronic solution, compared to the other cases in which the Pluronic solution is made with water and SPIONS are added later together with the bioactive glass.

From Figure 37, it is possible to see that the variation of the average shear stress of the inks confirms the typical behavior of a shear thinning fluid, even though the shape of the graphs is not perfectly the same as in theory [19]. This fact can be due to little defects during the experiment, such as an uneven distribution of the fluid between the parallel plates, or the presence of a not completely

homogeneous ink. The presence of a yield stress in the shear stress graphs is due to repulsive interactions of PEO chains in the overlapped micellar shells of the Pluronic gel [17].

The relationship between shear stress and shear rate can be described by the Hershel-Bulkley equation, reported in Equation 6 (page 61) [20].

The inks containing SPIONS experience higher shear stress compared to the ink 100:0 wt% because of the increased solid loading from the presence of the SPIONS. Consistent with the viscosity curves (Figure 36), the shear stress graph of the ink 95:5 wt% wet is positioned above the others, probably because of the different Pluronic solution preparation.

The shear stress behavior of the two Pluronic solutions can be explained by the development of a mechanically percolating and space filling network within the gel, in which the structural components, like the micelles and the SPIONS, form a continuous path throughout the material, making it behave in a solid-like way [21]. In the case of the inks, the presence of the glass particles disturb this network, preventing the establishment of this solid-like rheological behavior [18].

The 3D printed scaffolds generally show low mechanical properties (Figure 44 and Figure 45), probably due to the not complete densification of the bioactive glass 1393 B20 during sintering, as it can be observed from the SEM image in Figure 50.

Moreover, the presence of the SPIONS dispersed in the glass matrix could hamper a proper sintering of the glass particles, potentially leading to a further reduction in the mechanical properties. A possible explanation on the role of SPIONS considers the NPs as sources of defects in the glass matrix. Even though the introduction of magnetic nanoparticles has been considered in different studies as a way to improve the mechanical properties of the scaffolds [22], an excessive amount or a not uniform distribution can lead to their agglomeration, with a decrease of the mechanical properties of the matrix [23].

The non-homogeneity of the material was already observed during 3D printing, especially for the ink 90:10 wt%, where the SPIONS content is higher. The SEM images of Figure 49 confirm the presence of SPIONS agglomerates in the structure of 95:5 wt% wet and 90:10 wt% dry compositions, information that can be strictly correlated to the low mechanical properties of these two scaffold compositions. It is, therefore, possible that the detected SPIONS agglomerates acted as impurities rather than reinforcing the material [23].

In the composition 90:10 wt% the higher amount of SPIONS compared to 95:5 wt% dry may have promoted their aggregation, leading to defects formation in the matrix. However, obtaining a similar result with the composition 95:5 wt% wet was unexpected. The choice of using SPIONS in liquid solution for the ink production was mainly due to their better dispersion in water compared to powder form. The introduction of SPIONS as a liquid solution could have led to a different organization in the glass matrix and an unexpected SPIONS aggregation, as also suggested by the rheological results of Figure 36 and Figure 37, where the ink 95:5 wt% wet shows the highest viscosity and shear stress.

8.2 Magnetic properties and heating capacity

All the scaffold compositions containing SPIONS keep their magnetic properties, as proved by the attraction to the magnet in Figure 39 and by the presence of a non-zero magnetization in response to an alternating magnetic field in Figure 40.

Moreover, when exposed to an external alternating magnetic field, their magnetic properties lead to an increase in the surrounding temperature by up to 10 °C for the composition with the highest SPIONS content (Figure 41), reaching values suitable for hyperthermia treatments [4]. The lower temperatures reached after 7 days of immersion in SBF can be related to a slightly reduced SPIONS content because of the dissolution of the scaffold, as also proved by the ion release of boron and silicon (Figure 47). The released SPIONS can be excreted by the body through the liver or the spleen [27]. Since there is not much significative difference between the temperature increase in 95:5 wt% dry and 90:10 wt% dry, the former might be of greater interest because of its higher mechanical properties and better ink homogeneity. This demonstrates that these materials may have potential in thermotherapy.

8.3 Bioactivity

Scaffold bioactivity was assessed by the analysis of the ion release in SBF and by morphological and compositional analysis of the scaffolds' surface.

As observed in previous studies on bioactive glasses dissolution [24], the pH increase shown in Figure 46 is due to the ion exchange between glass and solution during the immersion time. In particular, cations from oxide network modifiers, such as Na^+ or K^+, are released into the solution while protons (H^+ and H_3O^+) occupy their place by going from the solution to the glass [25].

As observed during the mechanical characterization of the scaffolds, it is possible that the SPIONS disturbed the sintering of the glass particles, changing the glass surface area. Therefore, a higher increase in the pH could be due to a higher surface area to volume ratio in the scaffolds with SPIONS, which is related to a faster ion exchange [26].

The high sodium release explains the increase of pH, meaning that Na^+ ions are passing to the solution and exchanging with protons. The low level of iron refers to a negligible presence of magnetic NPs into the solution, meaning that SPIONS are not released, or released in minimum quantity. This aspect can be considered positively, since the release of ferrous ions is strictly related to the production of ROS species and can affect the cytotoxicity of the material [4], [27].

The different profiles in Figure 46 for the concentration 95:5 wt% wet, compared to 95:5 wt% dry and 90:10 wt% dry, could be related to a different way through which the SPIONS influence the dissolution, since they are introduced as a liquid solution instead of as a dry powder.

Regarding the ion release into the solution (Figure 47 and Figure 48), as observed in the pH level change of Figure 46, the presence of the SPIONS generally accelerates the process.

All the scaffolds undergo a degradation process and dissolve into the solution, as demonstrated by the concentration increase for both silicon and boron in Figure 47.

Regarding the bioactivity, all the scaffold types exhibit the deposition of a CaP HA-like reactive layer on the surface, as shown by the phosphorus consumption in Figure 48 and the nodules formation

on the surface after 7 days of immersion in SBF in Figure 49. Because of the concomitant dissolution of the glass, the CaP reactive layer is forming even if there is an increase in calcium release, as demonstrated in previous studies [28].

The nature of the reactive layer is not exactly equivalent to HA for all the scaffold compositions, since the calculated Ca/P ratios do not correspond to 1.67 but they are higher, as displayed in Table 7. However, it needs to be considered that the EDS analysis could have investigated a portion of the material which also comprised the area below the surface, since after only 1 week of immersion the deposited reactive layer did not appear quite thick (Figure 49), and the high Si atomic percentage (Table 7) could refer to the presence of a SiO_2-rich layer under the reactive layer. Nevertheless, the decreased Ca/P ratio value after 7 days immersion compared to the pre-immersion values is consistent with the uptake of phosphorous and the precipitation of a reactive layer. Additional analysis, such as FTIR, would be necessary to better identify the composition of the layer.

8.4 Cell viability

Cell culture in the presence of the scaffold brought to unfavorable results, with very low cell viability and proliferation around and on the top of the samples after 7 days of culturing (Figure 51). However, it needs to be considered that the cell seeding density was quite low compared to other studies on cell viability [29], as it is also proved by the poor cell proliferation in the positive control.

Optical microscope observations (Figure 54) confirmed that using a higher cell seeding density enhances cell proliferation, since a significantly greater number of cells was present in each well after 7 days of culture.

Nonetheless, increasing cell seeding density does not completely resolve the issue: while cells proliferate and successfully spread around the scaffold, they remain relatively round and in a lower amount in its immediate vicinity.

Consequently, additional investigations regarding cell viability should be considered. One important aspect could be the presence of a pH and ion concentration gradient within the scaffold structure. Indeed, the cell culture was performed in static conditions, so the medium inside of the pores was not properly refreshed. As already demonstrated in previous studies [30], performing cell culture under 15 rpm agitation could improve ion mobility and help prevent local concentrations in ions and pH. Therefore, cell tests should be repeated taking this aspect into account and using a cell seeding density comparable to the one employed for the performed additional cell observation.

REFERENCES

[1] E. Feilden, E. G.-T. Blanca, F. Giuliani, E. Saiz, and L. Vandeperre, “Robocasting of structural ceramic parts with hydrogel inks,” *Journal of the European Ceramic Society*, vol. 36, no. 10, pp. 2525–2533, Aug. 2016, doi: 10.1016/j.jeurceramsoc.2016.03.001.

[2] S. Lamnini, H. Elsayed, Y. Lakhdar, F. Baino, F. Smeacetto, and E. Bernardo, “Robocasting of advanced ceramics: ink optimization and protocol to predict the printing parameters - A review,” *Heliyon*, vol. 8, no. 9, p. e10651, Sep. 2022, doi: 10.1016/j.heliyon.2022.e10651.

[3] I. Rodrigues *et al.*, “Development of free binder zirconia-based pastes for the production of dental pieces by robocasting,” *Journal of Manufacturing Processes*, vol. 57, pp. 1–9, Sep. 2020, doi: 10.1016/j.jmapro.2020.06.015.

[4] A. Rajan and N. K. Sahu, “Review on magnetic nanoparticle-mediated hyperthermia for cancer therapy,” *J Nanopart Res*, vol. 22, no. 11, p. 319, Nov. 2020, doi: 10.1007/s11051-020-05045-9.

[5] L. Chao *et al.*, “Evaluation of Compressive and Permeability Behaviors of Trabecular-Like Porous Structure with Mixed Porosity Based on Mechanical Topology,” *JFB*, vol. 14, no. 1, p. 28, Jan. 2023, doi: 10.3390/jfb14010028.

[6] S. Zou *et al.*, “Mechanical and biological properties of enhanced porous scaffolds based on triply periodic minimal surfaces,” *Materials & Design*, vol. 219, p. 110803, Jul. 2022, doi: 10.1016/j.matdes.2022.110803.

[7] T.-R. Kim *et al.*, “Evaluation of Structural and Mechanical Properties of Porous Artificial Bone Scaffolds Fabricated via Advanced TBA-Based Freeze-Gel Casting Technique,” *Applied Sciences*, vol. 9, no. 9, p. 1965, May 2019, doi: 10.3390/app9091965.

[8] E. Ghassemieh, “Morphology and compression behaviour of biodegradable scaffolds produced by the sintering process,” *Proc Inst Mech Eng H*, vol. 222, no. 8, pp. 1247–1262, Nov. 2008, doi: 10.1243/09544119JEIM448.

[9] L.-C. Gerhardt and A. R. Boccaccini, “Bioactive Glass and Glass-Ceramic Scaffolds for Bone Tissue Engineering,” *Materials*, vol. 3, no. 7, pp. 3867–3910, Jul. 2010, doi: 10.3390/ma3073867.

[10] F. E. Ciraldo, E. Boccardi, V. Melli, F. Westhauser, and A. R. Boccaccini, “Tackling bioactive glass excessive in vitro bioreactivity: Preconditioning approaches for cell culture tests,” *Acta Biomaterialia*, vol. 75, pp. 3–10, Jul. 2018, doi: 10.1016/j.actbio.2018.05.019.

[11] M. I. Ojovan and W. E. Lee, “Immobilisation of Radioactive Wastes in Glass,” in *An Introduction to Nuclear Waste Immobilisation*, Elsevier, 2005, pp. 213–249. doi: 10.1016/B978-008044462-8/50019-3.

[12] P. Kumar and S. Agnihotri, “Synthesis of Dox Drug Conjugation and Citric Acid Stabilized Superparamagnetic Iron-Oxide Nanoparticles for Drug Delivery,” *Biochem Physiol*, vol. 01, no. 05, 2016, doi: 10.4172/2168-9652.1000194.

[13] S. Campelj, D. Makovec, and M. Drofenik, “Preparation and properties of water-based magnetic fluids,” *J. Phys.: Condens. Matter*, vol. 20, no. 20, p. 204101, May 2008, doi: 10.1088/0953-8984/20/20/204101.

[14] S. Kumar, C. Ravikumar, and R. Bandyopadhyaya, “State of Dispersion of Magnetic Nanoparticles in an Aqueous Medium: Experiments and Monte Carlo Simulation,” *Langmuir*, vol. 26, no. 23, pp. 18320–18330, Dec. 2010, doi: 10.1021/la1017196.

[15] C. Bárcena, A. K. Sra, and J. Gao, “Applications of Magnetic Nanoparticles in Biomedicine,” in *Nanoscale Magnetic Materials and Applications*, J. P. Liu, E. Fullerton, O. Gutfleisch, and D. J. Sellmyer, Eds., Boston, MA: Springer US, 2009, pp. 591–626. doi: 10.1007/978-0-387-85600-1_20.

[16] M. Jalaal, G. Cottrell, N. Balmforth, and B. Stoeber, “On the rheology of Pluronic F127 aqueous solutions,” *Journal of Rheology*, vol. 61, no. 1, pp. 139–146, Jan. 2017, doi: 10.1122/1.4971992.

[17] R. K. Prud’homme, G. Wu, and D. K. Schneider, “Structure and Rheology Studies of Poly(oxyethylene−oxypropylene−oxyethylene) Aqueous Solution,” *Langmuir*, vol. 12, no. 20, pp. 4651–4659, Jan. 1996, doi: 10.1021/la951506b.

[18] R. Bento, A. Gaddam, P. Oskoei, H. Oliveira, and J. M. F. Ferreira, “3D Printing of Macro Porous Sol-Gel Derived Bioactive Glass Scaffolds and Assessment of Biological Response,” *Materials*, vol. 14, no. 20, p. 5946, Oct. 2021, doi: 10.3390/ma14205946.

[19] D. B. Braun and M. R. Rosen, “Practical Rheology,” in *Rheology Modifiers Handbook*, Elsevier, 1999, pp. 1–69. doi: 10.1016/B978-0-8155-1441-1.50006-1.

[20] USACE Hydrologic Engineering Center • Powered by Scroll Viewport and Atlassian Confluence, “Hershel-Bulkley Parameters,” HEC-RAS Mud and Debris Flow. Accessed: Jan. 17, 2025. [Online]. Available: https://www.hec.usace.army.mil/confluence/rasdocs/rasmuddebris/non-newtonian-user-s-manual/user-inputs-and-model-parameters/hershel-bulkley-parameters#:~:text=The%20Herschel%2DBulkley%20model%20simulates,material%20more%20difficult%20to%20deform.

[21] B. Nan, P. Gołębiewski, R. Buczyński, F. J. Galindo-Rosales, and J. M. F. Ferreira, “Direct Ink Writing Glass: A Preliminary Step for Optical Application,” *Materials*, vol. 13, no. 7, p. 1636, Apr. 2020, doi: 10.3390/ma13071636.

[22] N. Marovič, I. Ban, U. Maver, and T. Maver, “Magnetic nanoparticles in 3D-printed scaffolds for biomedical applications,” *Nanotechnology Reviews*, vol. 12, no. 1, p. 20220570, Jul. 2023, doi: 10.1515/ntrev-2022-0570.

[23] C. Shuai *et al.*, “A magnetic micro-environment in scaffolds for stimulating bone regeneration,” *Materials & Design*, vol. 185, p. 108275, Jan. 2020, doi: 10.1016/j.matdes.2019.108275.

[24] J. R. Jones, P. Sepulveda, and L. L. Hench, “Dose-dependent behavior of bioactive glass dissolution,” *J. Biomed. Mater. Res.*, vol. 58, no. 6, pp. 720–726, Jan. 2001, doi: 10.1002/jbm.10053.

[25] L. L. Hench, “Bioceramics: From Concept to Clinic,” *Journal of the American Ceramic Society*, vol. 74, no. 7, pp. 1487–1510, Jul. 1991, doi: 10.1111/j.1151-2916.1991.tb07132.x.

[26] S. Fagerlund, P. Ek, L. Hupa, and M. Hupa, “Dissolution Kinetics of a Bioactive Glass by Continuous Measurement,” *J. Am. Ceram. Soc.*, vol. 95, no. 10, pp. 3130–3137, Oct. 2012, doi: 10.1111/j.1551-2916.2012.05374.x.

[27] J. Dulińska-Litewka, A. Łazarczyk, P. Hałubiec, O. Szafrański, K. Karnas, and A. Karewicz, “Superparamagnetic Iron Oxide Nanoparticles—Current and Prospective Medical Applications,” *Materials*, vol. 12, no. 4, p. 617, Feb. 2019, doi: 10.3390/ma12040617.

[28] E. Fiume, J. Massera, D. D’Ambrosio, E. Verné, and F. Baino, “Robocasting of multicomponent sol-gel–derived silicate bioactive glass scaffolds for bone tissue engineering,” *Ceramics International*, vol. 48, no. 23, pp. 35209–35216, Dec. 2022, doi: 10.1016/j.ceramint.2022.08.121.

[29] A. Szczodra *et al.*, “Pore graded borosilicate bioactive glass scaffolds: in vitro dissolution and cytocompatibility,” *J Mater Sci: Mater Med*, vol. 35, no. 1, p. 17, Mar. 2024, doi: 10.1007/s10856-024-06791-1.

[30] A. Szczodra *et al.*, “Boron substitution in silicate bioactive glass scaffolds to enhance bone differentiation and regeneration,” *Acta Biomaterialia*, vol. 186, pp. 489–506, Sep. 2024, doi: 10.1016/j.actbio.2024.07.053.

9. CONCLUSIONS

In the present work, 3D-printed magnetic scaffolds were successfully manufactured and analyzed in the context of bone tissue repair combined with hyperthermia for the treatment of bone cancer. This activity was carried out as a collaboration between Tampere University (Finland) and Politecnico di Torino (Italy).

In Politecnico di Torino, SPIONS were successfully synthetized and sent to Tampere University, where they were incorporated with bioactive glass 1393 B20 to form 4 different ink compositions. The obtained inks exhibited a shear thinning behavior under rheological testing, proving to be suitable for robocasting technique. The process of 3D printing led to the production of porous scaffolds, showing promising results in the context of hyperthermia treatment, as SPIONS maintained their magnetic properties. Under an external magnetic field, the magnetic properties of the scaffolds led to an increase in temperature of the surrounding. The increase in temperature is a function of the SPIONS loading content and the method through which SPIONS were introduced (in liquid solution or as a dry powder).

Scaffolds' bioactivity was preserved in the presence of SPIONS, since all the compositions exhibited the deposition of a reactive layer after 1 week of immersion in SBF. While it is likely that the reactive layer is HA, this must be confirmed with additional analysis.

On the other side, the presence of the SPIONS negatively affected the mechanical properties of the scaffolds, lowering the average values of Young's Modulus and fracture strength. In particular, the mechanical properties were strongly reduced in the case of the compositions 95:5 wt% wet and 90:10 wt% dry, where SPIONS agglomerates, within the glass matrix, were identified as the primary cause. While the presence of agglomerates in the composition 90:10 wt% dry can be attributed to the higher SPIONS content, the result observed in the composition 95:5 wt% wet was unexpected, as SPIONS were intentionally incorporated as a liquid solution to improve particle dispersion. Further studies are therefore needed to fully understand the behavior of SPIONS in liquid solution when combined with glass powder and Pluronic solution to form an ink for robocasting.

Cell tests need to be repeated. The low proliferation of the cells in the control well, along with the low density of cells plated are likely to be the reason for the negative results obtained. Furthermore, shaking the well plate to prevent pH gradient across the scaffold might be required in future testing.

As a result, 95:5 wt% dry proved to be the most suitable composition containing SPIONS for the following reasons:

- It exhibited a smooth printing process, thanks to the homogeneity of its ink.
- The distribution of SPIONS within the glass matrix was more even, without the formation of big agglomerates.
- Among the compositions with SPIONS, it was the one with the highest mechanical properties.
- The increase in temperature during the calorimetric test showed comparable results to the composition 90:10 wt% dry, meaning that a higher SPIONS content does not increase significantly the heating capacity.

This study represents an innovative step towards the possibility of offering new, multifunctional treatments able to combine different needs at the same time. The application of this concept could

lead to significative improvements in the fight against cancer, in particular in the context of cancer recurrence post-surgery.

Given the previously described limitations, future developments might focus on ways to improve the mechanical properties of the scaffolds, in order to reach at least the ones of trabecular bone, as it has been already achieved with scaffolds made of only 1393 B20 bioactive glass. Despite the additional investigations required about cell viability, further studies could focus on ways to enhance the biocompatibility of the scaffolds, for instance by using different types of coating for SPIONS.